

Electronic Theses and Dissertations, 2004-2019

2019

Artificial Magnetism and Topological Phenomena in Optics

Midya Parto
University of Central Florida

 Part of the [Electromagnetics and Photonics Commons](#), and the [Optics Commons](#)
Find similar works at: <https://stars.library.ucf.edu/etd>
University of Central Florida Libraries <http://library.ucf.edu>

This Doctoral Dissertation (Open Access) is brought to you for free and open access by STARS. It has been accepted for inclusion in Electronic Theses and Dissertations, 2004-2019 by an authorized administrator of STARS. For more information, please contact STARS@ucf.edu.

STARS Citation

Parto, Midya, "Artificial Magnetism and Topological Phenomena in Optics" (2019). *Electronic Theses and Dissertations, 2004-2019*. 6830.
<https://stars.library.ucf.edu/etd/6830>

ARTIFICIAL MAGNETISM AND TOPOLOGICAL PHENOMENA IN OPTICS

by

MIDYA PARTO

B.S. University of Tehran, 2011

M.S. University of Tehran, 2014

M.S. University of Central Florida, 2016

A dissertation submitted in partial fulfillment of the requirements
for the degree of Doctor of Philosophy
in CREOL/The College of Optics & Photonics
at the University of Central Florida
Orlando, Florida

Summer Term
2019

Major Professor: Demetrios N. Christodoulides

© 2019 Midya Parto

ABSTRACT

Recent years have witnessed intense research activities to effectively control the flow of photons using various classes of optical structures such as photonic crystals and metamaterials. In this regard, optics has benefited from concepts in condensed matter and solid-state physics, where similar problems concerning electronic wavefunctions arise. An important example of such correspondence is associated with the photon dynamics under the effect of an artificial magnetic field. This is especially important since photons, as neutral bosons, do not inherently interact with magnetic fields. One way to mitigate this issue is to exploit magneto-optical materials. However, as is well known, using such materials comes with several issues in terms of optical losses and fabrication challenges. Therefore, clearly of interest would be to devise certain schemes, which employ conventional dielectric materials, and yet provide an artificial “magnetic field” e.g. through geometric phases imprinted in the photonic wave amplitudes. Here, we utilize such schemes to observe various optical wave phenomena arising from the associated artificial magnetism. First, we show that light propagation dynamics in a twisted multicore optical fiber is governed by the Schrödinger equation in the presence of a magnetic potential. Using this, we experimentally observe Aharonov-Bohm suppression of optical tunneling in these structures. Moreover, we use notions from topological insulators to demonstrate the first dielectric-based topological lasers both in 1- and 2-dimensional lattices of microring resonators. Our measurements show that such laser arrays exhibit significant improvement in terms of robustness against defects and disorder, as well as higher slope efficiencies as compared to conventional laser arrays. Finally, we show both theoretically and experimentally, that the cooperative interplay among vectorial electromagnetic modes in coupled metallic nanolasers can be utilized as a means to emulate the

classical XY Hamiltonian. In particular, we discern two phases in these systems, akin to those associated with ferromagnetic (FM) and antiferromagnetic (AF) materials.

To my family,
Mohammad, Farideh and Kaveh.

ACKNOWLEDGMENTS

I would like to acknowledge all of those without whom this work would have never been accomplished. First and foremost, I would like to thank my advisor Dr. Demetrios Christodoulides for his enduring support throughout my PhD studies. With the help of his thoughtful guidance, knowledge, and encouragement, I was able to challenge myself to grow and excel in my scientific endeavors. It was truly a great pleasure for me to work with him. I would like to express my gratitude to my co-advisor Dr. Mercedeh Khajavikhan. Without her support and the fruitful collaborations with Dr. Khajavikhan's supervision, the experimental observations presented in this dissertation would have never been possible.

I am particularly grateful to Dr. Rodrigo Amezcua-Correa for generously giving us full access to his facilities. In addition, I would like to thank all my committee members, Dr. Patrick LiKamWa and Dr. Eduardo Mucciolo for their constructive remarks and sharing their knowledge with me, from which my work has benefited.

I would like to thank all my past and current colleagues and groupmates. I would like to specially thank Amin, Pawel, Absar, Billy, Ali Miri, Helena, Fan and Jason. Also many thanks to CREOL faculty and staff for all their help and support during these years of my PhD.

On a more personal note, I would like to thank all my friends during these years and in the past, who made my life a more enjoyable experience. I want to thank my best friend Roxana for being a member of family for me, Nick for being such a great friend throughout these years, DD and Madi for always being kind to me, and Saeed with whom it is always relaxing to talk. Also many thanks to Layla and Omid, Steffen and Maria, Ali and Mina, Hossein and Fatemeh, Fedor,

Mehrdad and Erica, Abbas, Alireza, Mohsen, and my high-school friends Amir, Mojtaba, Arman, Pouyan and Arash.

Finally, and above all, I want to express my utmost gratitude and endless love for my dear family who always were there for me in the happiness and hardships of my life, and supported me unconditionally. I literally cannot put into words how much I love them, but I will try to do my best. I am deeply grateful to my mother, Farideh, who taught me how to love and be patient no matter what comes on my way. I thank my father, Mohammad, from whom I learned to be persistent and strong, no matter how tough life gets. And finally my brother, Kaveh, who was my first teacher and mentor, and always took care of me. I am lucky to have you all!

TABLE OF CONTENTS

LIST OF FIGURES.....	xi
LIST OF TABLES	xxii
CHAPTER 1: INTRODUCTION	1
CHAPTER 2: GEOMETRIC PHASES AND SYNTHETIC MAGNETIC FIELDS IN TWISTED MULTICORE OPTICAL FIBERS.....	4
2.1. Introduction	4
2.2. Linear/nonlinear twisted multicore optical fibers.....	4
2.2.1 Light propagation in twisted multicore ring-shaped fiber structures.....	6
2.3. Observation of twist-induced geometric phases and inhibition of optical tunneling via Aharonov-Bohm effect.....	16
2.3.1 A twisted multicore fiber platform for realizing synthetic magnetic fields for photons 19	
2.3.2 Controlling and suppressing optical tunneling via twist-induced geometric phases	21
2.3.3 Impact of nonlinearity on AB tunneling inhibition.....	22
2.3.4 Suppression of tunneling in higher-order spatial modes	25
2.3.5 Experimental methods	26
2.3.6 Supermodes of twisted multicore optical fibers.....	28
2.3.7 Perturbation analysis of the tunneling inhibition.....	30

2.3.8	Coupling of the fundamental mode and higher-order modes.....	33
2.3.9	Kerr-induced detuning in high powers	36
2.3.10	Coupling suppression of higher-order modes	36
2.4.	Zero-DGD multicore optical fibers	38
2.5.	Summary	47
CHAPTER 3: TOPOLOGICAL INSULATOR LASERS.....		50
3.1.	Introduction	50
3.2.	Lasing in the topological defect of a 1D SSH array	52
3.2.1	Theoretically predicted spectra emitted by the PT-symmetric SSH laser array	63
3.2.2	Complex band structure of the CT-symmetric Hamiltonian	64
3.2.3	Frequency upshift in the spectra	65
3.2.4	Analytical solution for the edge state in the SSH array	66
3.3.	2D Topological laser.....	67
3.3.1	Characterization setup	77
3.3.2	Fabrication procedures	78
3.3.3	Spectra from extended edge states	80
3.3.4	Calibration of output couplers.....	80
3.3.5	Mode directionality depending on pumping conditions	81
3.3.6	FDTD simulation of microring resonator involving an S-bend.....	81

3.4. Summary	83
CHAPTER 4: SPIN-LIKE BEHAVIOR AND GEOMETRICAL FRUSTRATION IN NANOLASER ARRAYS.....	85
4.1. Introduction	85
4.2. Theory of coupled metallic nanolasers.....	86
4.3. Observing ferromagnetic and antiferromagnetic behavior in coupled nanolasers.....	91
4.4. Geometric frustration in nanolaser lattices.....	94
4.5. Lasing in the ferromagnetic state of a square lattice	95
4.6. Derivation of the energy landscape function	98
4.7. Fabrication procedure and SEM images	101
4.8. Characterization setup	103
4.9. Light-light curves and spectral evolutions	108
4.10. Tuning the exchange couplings J_{ij}	110
4.11. Polarization measurements for frustrated states	112
4.12. Summary	113
CHAPTER 5: CONCLUDING REMARKS	115
REFERENCES	118

LIST OF FIGURES

Figure 1 (a) Schematic of a 2N-core twisted optical fiber, (b) its equivalent one-dimensional lattice.....	8
Figure 2 Schematic of an 8-core twisted optical fiber.....	9
Figure 3 Intensity evolution in the eight-core fiber of Fig. 2.....	9
Figure 4 Destructive interference between photons tunneling through two possible paths in the twisted eight-core fiber.....	9
Figure 5 Intensity evolution in the nonlinear twisted eight-core fiber.....	10
Figure 6 Nonlinear Aharonov-Bohm suppression of optical tunneling in a twisted four-core fiber.....	12
Figure 7 Comparison between analytical and numerical solutions for the light intensity evolution in the first core of the twisted four-core fiber structure.....	14
Figure 8 Beam propagation analysis of the twisted four-core fiber structure: intensity evolutions for (a) low and (b) high input powers.....	15
Figure 9 The robustness of the effect against nonuniformity, when core 2 is detuned from the rest of the structure by $\delta = 0.8$	16
Figure 10 Twisted fiber structures as a platform for realizing synthetic magnetic fields for photons. A twisted four-core optical fiber in which the photon tunneling evolution dynamics are analogous to those expected from electrons in the presence of a magnetic field. The constantly rotating local transverse coordinates are depicted at three different planes. The top inset shows a microscope image of the input facet of the four-core fiber used in our experiments. The low-index fluorine-	

doped core is clearly visible at the center of the fiber. The bottom inset depicts a schematic of a two-dimensional atomic lattice in the presence of a static perpendicular magnetic field (arrows), where a tight-binding formalism can be utilized to describe the electronic band structure after a Peierls substitution..... 21

Figure 11 Dependence of optical tunneling dynamics on the AB phase. Normalized light intensity at the output of core #3 for different values of the AB phase ϕ (as induced by different twist rates). In all cases, core #1 is excited at the input with CW laser light at $\lambda = 1550 \text{ nm}$. Theoretical results corresponding to the same set of parameters are also provided for comparison. At $\phi = \pi/4$, the third core always remains dark, clearly indicating AB tunneling suppression..... 24

Figure 12 AB inhibition of tunneling in the presence of optical nonlinearities. Output light intensity profiles from a twisted, 24 cm long, four-core fiber when only core #1 is quasi-linearly excited for (A), $\phi = 0$ (no twist), (B), $\phi = \pi/4$, and (C), $\phi \approx 0.27\pi$. In (A-C), the pulses used had a peak power $\sim 500W$ at $\lambda = 1064 \text{ nm}$. Plots (D-F) show similar results when the input peak power is $\sim 6kW$ and hence nonlinear Kerr effects are at play. It is evident that the coupling between cores #1 and #3 is completely suppressed in both cases (B,E), regardless of the power levels used, indicating an immunity of the AB tunneling suppression against nonlinear index changes. For higher input powers (D-F), the self-focusing nonlinearity further suppresses light coupling, even among adjacent cores. The inset on the left depicts numbers in panel (A) depict the relative arrangement of the four cores in this particular experiment. 25

Figure 13 AB tunneling suppression for higher-order modes. Light intensity distributions at the output of a twisted four-core fiber when the higher-order $LP02$ mode is excited with CW light at $\lambda = 665 \text{ nm}$. These results are presented for (A), $\phi = 0$ (no twist), (B), $\phi \approx 0.11\pi$, and (C), $\phi =$

$\pi/4$. Even though in the excited core #1, most of the optical power resides in the fundamental LP_{01} mode, only the LP_{02} mode appears in the remaining cores due to its higher coupling coefficient. Plot (C) clearly reveals that AB suppression of light tunneling occurs in a universal fashion, even for higher-order modes. The inset on the left depicts numbers in panel (A) depict the arrangement of the cores corresponding to these observations. 26

Figure 14 Twisted N-core fiber. The tunneling Aharonov-Bohm phase is depicted in the figure by φ 28

Figure 15 Inhomogeneous couplings among cores. Different coupling coefficients among various nearby cores in a four-core system for an LP_{11} mode. 37

Figure 16 A hexagonal MCF structure involving six dissimilar cores. 39

Figure 17 Schematic of a four-core MCF. 43

Figure 18 The four supermode intensity profiles of an ultra-low DGD four-core MCF design. 43

Figure 19 Variation of DGD over the C-band for a three-core fiber design..... 47

Figure 20 (a) InGaAsP multilayer quantum well structure used in the microrings, (b) a schematic of the SSH microring laser array, and (c) a microscope image of the fabricated structure with 16 elements. Insets show scanning electron microscope images of the grating at the end of the out-coupling waveguides, and the coupling region between two microrings. 53

Figure 21 Eigenvalue diagrams of (a) Hermitian and uniformly pumped ($g = 0$ and $g \neq 0$) and (b) PT-symmetric SSH lattice. The field profiles of the edge states are also depicted in the right and left insets. 56

Figure 22 Theoretically predicted steady-state lasing profiles for a) uniformly pumped and b) PT-symmetric SSH lattice. The insets show the power spectra corresponding to the edge mode and bulk modes as obtained from different locations in the array..... 58

Figure 23 The complex Berry phase $\Phi +$ as a function of the normalized gain η . The different phases are indicated through different colors. The simulated intensity distributions corresponding to these three distinct phases I, II, and III are depicted in (b), (c), and (d), respectively..... 60

Figure 24 The left panels depict the measured intensity distributions in the 16-element SSH array at every site. The middle panels show raw data from the extraction ports, while the right panels the corresponding power spectra. Each of the successive rows (a), (b), and (c) are progressively associated with phase I, II, and III observations. The inset in (a) provides the exponential intensity distribution of the lasing edge-state in a log-linear scale..... 62

Figure 25 Calculated spectra for the system considered in Fig. 17 in (a) phase I, (b) phase II, and (c) phase III. 64

Figure 26 Eigenvalue diagrams associated with the CT-symmetric Hamiltonian of Eq. (2-10) for three different normalized gain values indicated at the top. The three diagrams correspond to (a) phase I, (b) phase II, and (c) phase III. 65

Figure 27 A schematic of a semi-infinite PT-symmetric SSH microring laser array. 66

Figure 28 Topological insulator laser: lattice geometry and associated band structure. (A) Microscope image of an active InGaAsP topologically non-trivial 10x10 micro-resonator array. (B) SEM image of the out-coupling grating structures used to probe the array at the location indicated in (A). (C) SEM micrograph of a unit cell comprised of a primary ring site surrounded by four identical intermediary racetrack links. (D) Frequency band diagram corresponding to an

infinite ribbon structure based on the topological lattice used in this study. The bulk bands are colored in black, while the two counter-propagating edge-state bands in green and red. (E) A schematic of the topological array when pumped along the perimeter so as to promote edge mode transport. The directionality of energy flow is monitored through the power extracted from the out-coupling gratings..... 70

Figure 29 Slope efficiencies and associated spectra of topological and trivial lattices. (A) Output intensity vs. pump density for a 10x10 topological array with $\alpha = 0.25$ and its corresponding trivial counterpart ($\alpha = 0$). In this experiment the enhancement of the slope efficiency ratio is approximately 3x. (B) Emission spectra from a trivial and a topological array when pumped at 23.5 kW/cm². Evolution of the spectrum as a function of the pumping levels for (C) topological and (D) trivial arrays. Single-mode, narrow-linewidth lasing in (C) is clearly evident. 73

Figure 30 Lasing characteristics of topological lattices vs. that of their corresponding trivial counterparts under different pumping conditions. Lasing in a (A) non-topological and (B) topological array when only their periphery is selectively pumped. (C) and (D) represent the spectral content as obtained from specific edge-sites of the arrays as depicted in (A) and (B), correspondingly. Notice that the topological lattice remain single-moded while the trivial one emits in several modes. Lasing transport in a (E) trivial array and in a (F) topological lattice when the bottom side is pumped. The excitation of the edge-mode in (F) is clearly visible. (G) and (H) present similar results when the pumping region at the bottom side is further extended. In (H) the edge-mode is again excited. No laser radiation is observed from the extracting ports in the trivial lattice (G). The pumping conditions are shown in the insets at the top..... 74

Figure 31 Robust behavior of the lasing edge mode with respect to defects in a topological array. Lasing response of a (A) topological and (B) trivial array in the presence of two defects intentionally inserted on the periphery. Note that the edge mode transport in (A) clearly bypasses the defects, whereas no such behavior is observed in its trivial counterpart. 75

Figure 32 Topological active array involving chiral S-micro-resonator elements. (A) SEM image of a 10x10 topological array. The primary resonators feature an internal S-bend for enforcing in this case a right-spin, while the intermediate link design is the same as in Fig. 1 (C). (B) A closeup SEM micrograph of the basic elements involved. (C) Field distribution in an individual S-element as obtained from FDTD-simulations. (D) Measured intensity profile associated with the lasing edge-mode in a topological array with $\alpha = 0.25$. In this system, the periphery is selectively pumped, and the energy flows unidirectionally in a clock-wise manner, as also indicated by the radiation emerging from the extracting ports..... 77

Figure 33 (A) Sketch of the measurement setup: sample on the lower left, pump laser on top and analysis setup on the right. (B) Pumping scheme and masks employed for the interrogation of the micro-resonator arrays. 78

Figure 34 Manufacturing steps of the micro-ring resonators..... 78

Figure 35 Spectra along the perimeter for (A) trivial and (B) topological sample. The axes are the same for all graphs and are denoted in the center. 80

Figure 36 (A) Pumping scheme of micro-resonator arrays. (B) Camera image of a sample pumped as shown in (A). (C) Recorded intensity profiles from the two out-coupling ports. 81

Figure 37 (A) pumping configuration, (B) and (C) field intensity profiles at different OD filter positions with spectra of the two ports to the right. 82

Figure 38 Exponential decay in the amplitude of an anti-clockwise pulse in an S-microresonator cavity identical to those implemented in the design of Fig. 32. 82

Figure 39 Spin-like behavior in coupled metallic nanolaser arrays. a, Different regimes in spin systems with ferromagnetic (FM) and anti-ferromagnetic (AF) exchange interactions. b, SEM image of an array of six coupled active nanodisks (before silver deposition) used in this study. 89

Figure 40 Lasing supermodes in coupled nanolasers and their corresponding pseudospins when arranged in simple geometric configurations. a, Ferromagnetic and b, anti-ferromagnetic interactions between pseudospins associated with the longitudinal component of the magnetic field in coupled nanodisk lasers. Depending on the size of the individual elements (575 nm in a, or 930 nm in b), different TE_{22} and TE_{14} electromagnetic modes predominantly lase, leading to an FM and an AF regime of coupling between nanodisk dimers. c, Geometrically frustrated ground states of the classical XY Hamiltonian corresponding to vortices with opposite winding numbers +1 (top) and -1 (bottom). d, Resonant electromagnetic supermodes in a triangular array of AF-coupled metallic nanodisks associated with the frustrated states of c. 91

Figure 41 FM and AF interactions in four-element coupled nanodisk lasers. Observation of FM (a-c) and AF (d-f) states in different scenarios of coupled metallic nanolasers with various sizes. a, Longitudinal magnetic field profiles corresponding to the lasing TE_{22} mode in four coupled nanodisks of radius 575 nm. b, Theoretically predicted and c, experimentally measured optical field intensities and polarization characteristics of the light emitted by such an array. d-f, Similar results for the AF case where nanodisks having radii of 940 nm are employed in the same square geometry. The yellow arrows indicate the direction of the linear polarizer. No geometric frustration is observed in either the FM or the AF regimes. 93

Figure 42 Frustrated states in spin-like lasing fields emerging from nanolaser arrays. a, Simulated lasing profile, b, experimentally measured optical intensities, and c, associated pseudospin configuration for a geometrically frustrated lasing supermode emitted from an $N = 3$ nanolaser array with an AF-type interaction. In this case each nanodisk has a radius of 930 nm , leading to a TE_{14} cavity mode. d, Optical intensity pattern obtained after diffraction from a triangular aperture, indicating a topological charge of $l = +1$, as expected from the pseudospin arrangement of c. e-h & i-l present similar results for $N = 5$ and $N = 6$ nanolaser arrays involving elements with radii 930 nm and 850 nm (TE_{13} mode), respectively. Note that for these structures the triangular diffraction pattern indicates an $l = -2$ topological charge (h & l). The triangular diffraction measurements were all performed by incorporating a $\lambda/4$ waveplate before the aperture followed by a linear polarizer so as to filter for the right-hand circularly polarized component. 96

Figure 43 Square lattice of 20×20 nanolasers exhibiting FM spin-like behavior. a, SEM image of a 20×20 square lattice of coupled active nanodisks used in this study. b, Below the lasing threshold, the orientation of the pseudospins associated with the electromagnetic TE_{22} mode within each laser element are randomly fluctuating. c, Once the pump exceeds the threshold, the array starts to lase in an FM state, with the pseudospins aligned in the same direction. d & e, Experimentally measured optical intensity patterns and polarization characteristics of the light emitted by this square lattice below (spontaneous emission) and above the lasing threshold, respectively. In the lasing regime, the far-field from this nanolaser square lattice clearly indicates in-phase coherent emission in the TE_{22} mode (ferromagnetic state). The yellow arrows indicate the orientation of the linear polarizer. 97

Figure 44 Fabrication process of a metallic nanolaser lattice. This same process is used in other geometries as well. The bottom right corner provides a legend to the materials of the structure. a, Cleaned wafer with InGaAsP quantum wells grown on an InP substrate. b, A thin layer of negative tone HSQ ebeam resist is spun onto the sample. c, The wafer is patterned by ebeam lithography and the resist is developed. d, A dry etching process is used to define the lattice. e, 1 μm Ag is deposited by means of ebeam evaporation. f, The sample is mounted and bonded to a glass microscope slide silver side down with SU-8. g, Sample is immersed into HCl to remove the InP substrate. 102

Figure 45 SEM images of the lattices. In all lattices the nanodisks elements are separated by 50 nm. a, 20 x 20 array of nanodisks (radius 545 nm). b, zoomed in view of the front left corner of the 20 x 20 array. c, 4-element array of nanodisks (radius 575 nm). d, e, & f, 3-, 4-, & 5-element arrays (radius 930 nm, 940 nm, and 930 nm, respectively). g, 6-element array (radius 850 nm). 103

Figure 46 Characterization microphotoluminescence setup schematic. The samples are pumped with a 1064 nm fiber laser and focus onto the sample with a 50x objective (N.A. 0.42). Light is either directed to an InGaAs camera to observe emission patterns, or to a monochromator with an attached InGaAs linear array detector. The emission power is collected at the location of the first focus after the pump notch filter. The triangular aperture used to reveal the OAM of the radiated beams is removable so as to not obstruct imaging the sample surface and to collect proper modal profiles. 106

Figure 47 Characterization of charge measurement using a 7-element metallic lattice operating at room temperature. a, Simulated z-component of the magnetic field. b, c, & d, The simulated

intensity profile and the polarization resolved intensity distributions when filtered for horizontal (c) and vertical (d) polarizations. e, f, & g, The experimentally observed emission pattern and intensity distributions. h, The simulated far-field diffraction pattern of the lattice after passing through a triangular aperture. i, The experimentally observed profile is in agreement and has $l = -2$. j, The light-light curve shows a clear onset in lasing. k, The spectral evolution of this laser shows linewidth narrowing and single-mode behavior. 107

Figure 48 Light-light and spectral evolutions curves for the lattices with antiferromagnetic-like coupling. All the lattices indicate a clear onset of lasing and linewidth narrowing. a & b, c & d, and e & f, show the light-light and the spectral evolutions of lattices operating in the TE_{14} mode at temperature of 225 K for the 3-, 4-, & 5-element lattices, respectively. The radii of the nanodisks are 930 nm, 940 nm, and 930 nm, respectively. g & h the 6-element lattice supports lasing at room temperature in the TE_{13} mode (850 nm radius elements). 109

Figure 49 Output characteristics of the 4-element and 20×20 -element array displaying ferromagnetic like coupling. Both lattices operate in the TE_{22} mode, albeit at differing temperatures. a & b, the 4-element arrangement is cooled to 78 K and has disks with radii of 575 nm. c & d, the 20×20 -element lattice (radius of 545 nm) generates more than 10 mW peak output power..... 110

Figure 50 Asymmetric triangle geometry. a, A schematic of three pseudospins arranged on a triangle with asymmetric exchange couplings. In this case, the angles of the bottom pseudospins are expected to change as shown in the figure. b, FEM simulation of the lasing supermode in an asymmetric triangular array of nanodisks. Each nanodisk supports a TE_{13} mode. c-h Experimental measurements (top) together with theoretically calculated results for diffraction intensities and

polarization states of the optical fields emitted by such a nanodisk array. The arrows depict the direction of the linear polarizer..... 112

Figure 51 Polarization measurements for frustrated states. Theoretically predicted and experimentally measured polarization profiles for lasing supermodes in arrays of a, $N = 3$, b, $N = 5$, and c, $N = 6$ nanodisk laser arrays. The arrows indicate the direction of linear polarizations. 113

LIST OF TABLES

Table 1 Effect of surface passivation on current devoted to surface recombination at threshold.	34
Table 2 Low DGD MCF structures of different geometries.....	45

CHAPTER 1: INTRODUCTION

Electrons under the effect of a magnetic field can display an array of interesting and counterintuitive effects. These include for example the emergence of Landau levels [1], quantum Hall [2] and topological insulator effects [3], as well as the quantization of magnetic flux through a superconductor [4], to mention a few. Recently, the prospect of observing processes similar to those expected from magnetic fields has been the subject of intense research efforts, including for example photon and cold atom dynamics under the action of synthetic magnetic fields [5–12], photonic topological insulators [13–15] and nonreciprocal optical elements [16]. In such arrangements, typically an artificial magnetic field is introduced by exploiting the intimate connection between Berry’s phase in parameter space and the Aharonov-Bohm (AB) phase [17–20].

In electronic systems, an intriguing phenomenon arising from the presence of a magnetic field is a possible inhibition of electron tunneling in degenerate quantum channels [21]. This latter effect is a direct by-product of an AB phase [22,23] that in turn leads to a complete elimination of tunneling, a process resulting from the destructive interference of the eigenfunctions involved. However, despite early theoretical efforts, an experimental observation in this regard is still lacking, as of yet, within the context of solid-state physics - primarily due to practical challenges associated with the need for ultrahigh magnetic fluxes. Of interest would be to realize an equivalent optical structure, that effectively benefits from synthetic magnetic fields to overcome this issue. In Chapter 2, we propose one such realization using a twisted multicore optical fiber, and observe the AB suppression of optical tunneling for the first time. From a different perspective, our results also provide the first observation of a geometric phase in the realm of optics that is associated with the

tunneling processes of photons. The effect of optical Kerr nonlinearity on this AB phase is also studied both theoretically and experimentally.

As already mentioned, one important phenomenon arising from the interaction of electrons with magnetic fields is the notion of topological insulators (TI). In condensed matter physics, TIs represent new forms of matter wherein electron conduction is prohibited in the bulk, while it is allowed along the surface by means of edge states [3,24–26]. These gapless edge states emerge whenever a TI is terminated either on vacuum or is interfaced with an ordinary insulator- a principle better known as bulk-edge correspondence. This property stems from the fact that any transition from two distinct topological phases cannot be performed in a continuous fashion, but instead requires a bandgap-crossing at the interface of two materials that exhibit different topological invariants. In this respect, topological edge states are robust against local perturbations, since their characteristics are dictated by their corresponding bulk environment. This is in sharp contrast to conventional defect states that originate from imperfections, and are by nature sensitive to perturbations. It is this robustness that has incited a flurry of activities aimed to understand and harness the ramifications of topology in many and diverse fields ranging from optics to ultracold atomic gases, mechanics, and acoustics [27–30]. As indicated in recent studies, the introduction of topology in photonics can lead to a host of intriguing and unexpected results. These include for example unidirectional light transport, backscattered-free light propagation as well as immunity to structural imperfections [16]. Lately, there has been a great deal of interest in studying the interplay between non-Hermiticity and topology [31–33]. In this regard, photonics provides a versatile platform to perform such studies, since non-Hermiticity can be readily established through the introduction of optical gain and loss- something that has been previously exploited in observing

PT-symmetric interactions and spontaneous symmetry breaking effects [34,35]. As demonstrated in recent works, the isomorphism between the Schrödinger equation and the optical wave equation can be fruitfully utilized to design photonic lattice structures capable of displaying topological phenomena akin to those encountered in condensed matter physics [13–15,36]. In Chapter 3, we demonstrate the first magnet-free topological lasers both in 1D and 2D lattices of ring resonators. In 1D, we show that how by lasing in the edge mode of a Su-Schrieffer-Heeger (SSH) [37] array, the resulting emitted frequency is robust with respect to coupling disorders. Moreover, we observe unidirectional, robust edge-mode transport and enhanced slope efficiencies in our proposed 2D laser array.

Finally, in Chapter 4, we consider arrays of coupled nanodisk laser arrays in metallic claddings. A theoretical model describing possible supermodes of such structure is developed, and is shown to successfully predict the emergent lasing modes. In this respect, we show that the dissipation function in such a platform can be formulated in a way similar to the XY Hamiltonian describing interacting magnetic spins. Based on various geometrical parameters and electromagnetic modes involved, different regimes of ferromagnetic (FM)- and anti-ferromagnetic (AF)-like couplings are identified. Moreover, we show that in certain geometries and under AF-like couplings, the resonant electromagnetic modes in these nanolaser arrays will exhibit geometric frustration.

CHAPTER 2: GEOMETRIC PHASES AND SYNTHETIC MAGNETIC FIELDS IN TWISTED MULTICORE OPTICAL FIBERS

2.1. Introduction

Geometric phases appear ubiquitously in many and diverse areas of physical sciences, ranging from classical and molecular dynamics to quantum mechanics and solid-state physics. In the realm of optics, similar phenomena are known to emerge in the form of a Pancharatnam-Berry phase whenever the polarization state traces a closed contour on the Poincaré sphere. While this class of geometric phases has been extensively investigated in both free-space and guided wave systems, the observation of similar effects in photon-tunneling arrangements has so far remained largely unexplored. In this chapter, we first provide the theoretical analysis of light propagation dynamics in a twisted ring-shaped multicore optical fiber, both in the linear and nonlinear regimes. After that, we provide our pertinent experimental results. We experimentally demonstrate that the tunneling or coupling process in a twisted multi-core fiber system can display a chiral geometric phase accumulation-analogous to the Aharonov-Bohm effect. In our experiments, the tunneling geometric phase is manifested through the interference of the corresponding supermodes. Our work provides the first observation of Aharonov-Bohm suppression of tunneling in an optical setting.

2.2. Linear/nonlinear twisted multicore optical fibers

An intriguing phenomenon arising from the presence of a magnetic field, is a possible inhibition of electron tunneling in degenerate quantum channels-a process never been observed before in any physical system [21]. This latter effect is a direct byproduct of an Aharonov-Bohm

phase [22,23] that in turn leads to a complete elimination of tunneling, a process resulting from the destructive interference of the eigenfunctions involved. A possible optical realization of this effect has also been suggested in a twisted annular or multicore fiber configuration in [6]. In addition, similar systems have also been studied in parity-time-symmetric configurations, where it was found that the exact PT phase can be broken in a quantized fashion [38,39]. Apart from being fundamental in nature, this effect can be potentially utilized for applications, such as torsion sensors [40] and mode management [41], as well as dispersion and polarization control [42]. At this point we emphasize that this topological phenomenon has so far been considered only in the linear regime. In this respect, one may ask whether this Aharonov-Bohm tunneling suppression will still persist even under nonlinear conditions. In other words, is this process robust enough to withstand nonlinear effects?

This section is devoted to the study of twisted multicore optical fibers [43,44]. We will see that the evolution of light in a twisted multicore optical fiber can mimic that of electrons under the effect of a constant, perpendicular magnetic field, which manifests itself in a complex coupling coefficient between the neighboring elements. In other words, these structures can be considered as a viable platform for the realization of synthetic gauge fields for photons. In order to examine the role of this in photonics, we first discuss how the topological suppression of light tunneling can occur in a twisted ring waveguide array. Following this, we show that this topological suppression of light tunneling can be maintained completely intact in spite of the presence of optical nonlinearity. This holds true in any ring multicore system irrespective of dimensionality. Analytical results pertaining to four-core twisted nonlinear fiber structures indicate that the Aharonov-Bohm phase remains invariant and has no dependence whatsoever

on the power levels. At higher intensities, a discrete spatial soliton is formed that further suppresses the energy exchange or tunneling process. The effect of the twist rate on the onset of these mechanisms is also investigated. Moreover, the aforementioned effect can manifest itself even when the waveguide sides are detuned. Beam propagation simulations further corroborate our results - as obtained from nonlinear coupled mode theory.

2.2.1 Light propagation in twisted multicore ring-shaped fiber structures

In order to elucidate the mechanism behind the inhibition of optical tunneling, perhaps it is best to explore this effect under linear conditions. In this respect, consider a circular $2N$ -core waveguide arrangement as shown in Fig. 1 (a). Each waveguide channel is supposed to be single-moded, while it is evanescently coupled to its nearest neighbors. In addition, the structure is twisted along the propagation axis with a spatial period of Λ . Under these conditions, one can show that in the rotating frame, the evolution of the modal field amplitudes E_n obeys the following set of differential equations [11]:

$$i \frac{dE_n}{dz} + \beta_n E_n + \kappa (E_{n+1} e^{-i\phi} + E_{n-1} e^{i\phi}) = 0, \quad n = 0, 1, \dots, 2N - 1 \quad (2.1)$$

where the index n indicates the site number (modulo $2N$), β_n represents the propagation constant of each core, and κ is the coupling coefficient among nearest neighbors. In Eq. 2.1 $\phi = (k_0 n_0 \epsilon D^2)/2$ is the tunneling phase introduced by the twist, $k_0 = 2\pi/\lambda_0$, D is the core distance between successive sites, and $\epsilon = 2\pi/\Lambda$ is the angular twist pitch. Equation 2.1 clearly shows that in such a setting, the coupling coefficients are in fact complex, having equal and opposite phases depending on

whether the tunneling direction is clockwise or counter-clockwise. In what follows we show that for specific twist rates leading to the phase condition $N\varphi = \pi/2 + m\pi$, the energy exchange between sites #0 and #N is totally diminished – in other words, these two channels become effectively decoupled. To analytically prove this assertion, let us consider an infinite version (unfolded) of this same lattice, as shown in Fig. 1 (b). In this system the field dynamics are governed by the same equation, only this time $n \in (-\infty, +\infty)$. If the central site is the only one initially excited, the field distribution in this infinite array is given by:

$$i^n J_n(2\kappa z) e^{in\phi}, \quad n = \dots, -1, 0, 1, \dots \quad (2.2)$$

In the $2N$ circular array, the field amplitude at site n can then be obtained by summing up all the “echoes” resulting from the periodicity of the circular array, and hence one finds that [45]:

$$E_n(z) = \sum_{m=-\infty}^{\infty} i^{n+2mN} J_{n+2mN}(2\kappa z) e^{i(n+2mN)\phi} \quad n = 0, 1, \dots, 2N - 1 \quad (2.3)$$

From here, it is straightforward to see that the optical field in waveguide N is always zero:

$$E_N(z) = \sum_{m=0}^{\infty} [i^{(2m+1)N} J_{(2m+1)N}(2\kappa z) e^{i(2m+1)N\phi} + i^{-(2m+1)N} J_{-(2m+1)N}(2\kappa z) e^{-i(2m+1)N\phi}] = 0. \quad (2.4)$$

This completes the proof.

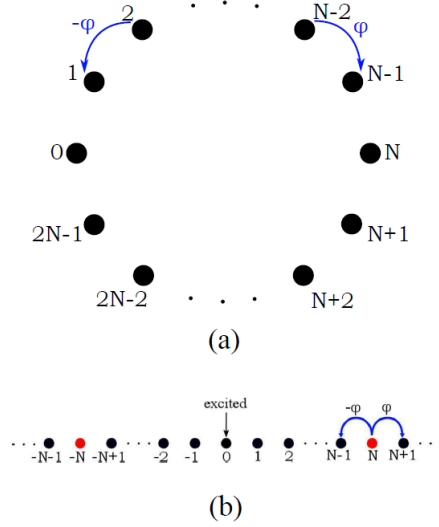


Figure 1 (a) Schematic of a $2N$ -core twisted optical fiber, (b) its equivalent one-dimensional lattice.

To demonstrate these dynamics, let us consider linear light evolution in an 8-core twisted fiber as depicted in Fig. 2. In order to achieve topological Aharonov-Bohm suppression, we set $4\phi = \pi/2$. Hence, in this case the twist pitch is given by $\Lambda = 8k_0n_0D^2$. The results of solving the coupled mode Eqs. 2.1 for this structure are shown in Fig. 3. It is clear that the core #5 remains dark, confirming the results predicted by the above general linear analysis. Because of this topological effect, any cross-talk between sites #1 and #3 is totally prohibited. This effect can be intuitively explained by noticing the fact that the two coupling paths (from core #1 to #5 via upper and lower paths, Fig. 4) differ from each other by a phase factor of $\pm\pi$. Subsequently, light transport along these two paths results in destructive interference, thus leaving the core #5 completely dark.

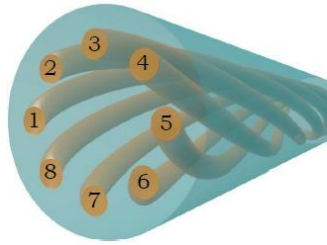


Figure 2 Schematic of an 8-core twisted optical fiber.

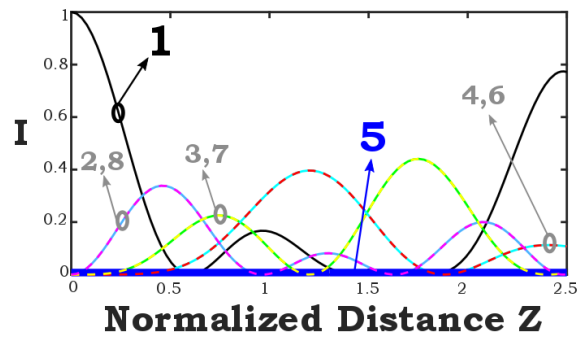


Figure 3 Intensity evolution in the eight-core fiber of Fig. 2.

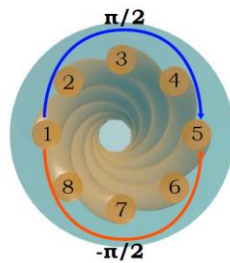


Figure 4 Destructive interference between photons tunneling through two possible paths in the twisted eight-core fiber.

From the previous discussion it is clear that the topological phenomenon under consideration is by nature linear. In this respect, one may ask whether it can withstand the nonlinear conditions. The purpose of this section is to answer this question, which we find it to be positive by both solving the coupled mode Eqs. 2.1, as well as using beam propagation techniques to analyze the structure.

In the presence of third order Kerr nonlinearity, Eqs. 2.1 will be modified to the following:

$$i \frac{dE_n}{dz} + \beta_n E_n + \kappa (E_{n+1} e^{i\phi} + E_{n-1} e^{-i\phi}) + \gamma |E_n|^2 E_n = 0 \quad (2.5)$$

where γ is the nonlinear Kerr coefficient. To investigate the wave evolution in this case, we study the dynamics for the same 8-core system that we discussed in the linear section. The results are presented in Fig. 5. It is clear from the figure that the suppression of coupling between cores #1 and #5 is preserved.

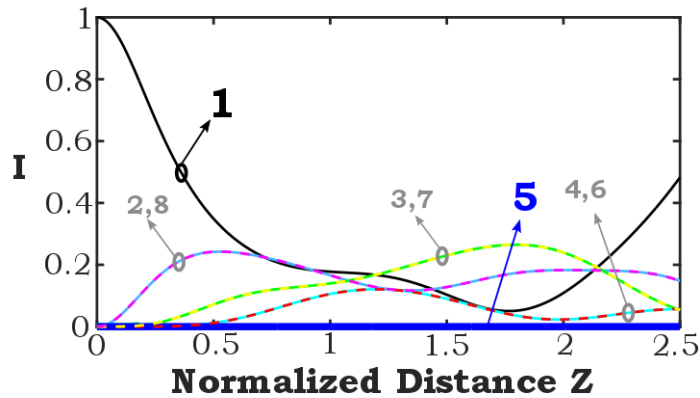


Figure 5 Intensity evolution in the nonlinear twisted eight-core fiber.

To examine the nonlinear dynamics, in what follows, we analyze Aharonov-Bohm suppression of optical tunneling the aforementioned behavior in a four-core twisted fiber. For this system, Eqs. 2.5 can be reduced to the following equations using the normalizations $Z = \kappa z$ and $E_n = \rho a_n \exp(i\beta_1 z)$:

$$\begin{aligned}
\frac{ida_1}{dZ} + a_2 e^{i\phi} + a_4 e^{-i\phi} + |a_1|^2 a_1 &= 0 \\
\frac{ida_2}{dZ} + a_1 e^{-i\phi} + a_3 e^{i\phi} + \delta a_2 + |a_2|^2 a_2 &= 0 \\
\frac{ida_3}{dZ} + a_2 e^{-i\phi} + a_4 e^{i\phi} + |a_3|^2 a_3 &= 0 \\
\frac{ida_4}{dZ} + a_1 e^{i\phi} + a_3 e^{-i\phi} + \delta a_4 + |a_4|^2 a_4 &= 0,
\end{aligned} \tag{2.6}$$

where we have chosen $\frac{\gamma\rho^2}{\kappa} = 1$ and $\delta = \Delta/\kappa$ (detuning between the cores). Here we are interested in the case where $\phi = \pi/4$. To examine light dynamics in this case, the system of Eqs. 2.6 is solved numerically. The results for the intensities in each core are shown in Fig. 10, where it is clear that the coupling from core #1 to #3 is effectively suppressed. This suggests that the third amplitude a_3 in Eqs. 2.6 can effectively be decoupled from the rest. Therefore, one can cast the problem in the following set of two coupled equations:

$$\begin{aligned}
i \frac{da_1}{dZ} + 2e^{i\pi/4} a_2 + |a_1|^2 a_1 &= 0 \\
i \frac{da_2}{dZ} + e^{-i\pi/4} a_1 + \delta a_2 + |a_2|^2 a_2 &= 0,
\end{aligned} \tag{2.7}$$

where we have used the fact that $a_4 = \exp(i\pi/2) a_2$. These equations can be further simplified using the new variables $u = a_1 \exp(-i\pi/4)$ and $v = \sqrt{2} a_2$:

$$\begin{aligned}
i \frac{du}{dZ} + \sqrt{2} v + |u|^2 u &= 0 \\
i \frac{dv}{dZ} + \sqrt{2} u + \delta v + \frac{1}{2} |v|^2 v &= 0.
\end{aligned} \tag{2.8}$$

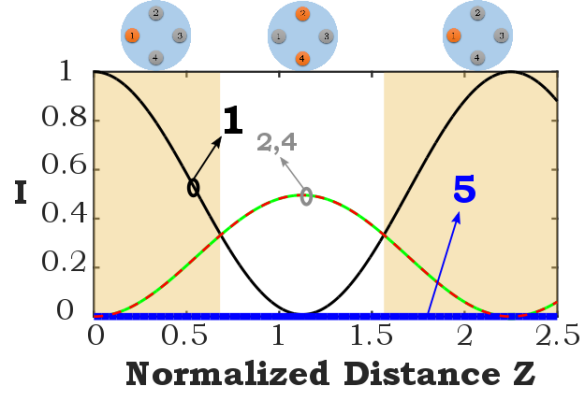


Figure 6 Nonlinear Aharonov-Bohm suppression of optical tunneling in a twisted four-core fiber.

Equations 2.8 define a system of four real equations in terms of the following parameters:

$$\begin{aligned}
 U_0 &= |u|^2 + |v|^2 & (a) \\
 U_1 &= |u|^2 - |v|^2 & (b) \\
 U_2 &= uv^* + u^*v & (c) \\
 U_3 &= i(u^*v - uv^*), & (d)
 \end{aligned} \tag{2.9}$$

namely:

$$\begin{aligned}
 \dot{U}_0 &= 0 & (a) \\
 \dot{U}_1 &= 2\sqrt{2} U_3 & (b) \\
 \dot{U}_2 &= \left(-\frac{1}{4}U_0 - \frac{3}{4}U_1 + \delta\right) U_3 & (c) \\
 \dot{U}_3 &= -2\sqrt{2} U_1 + \left(\frac{1}{4}U_0 + \frac{3}{4}U_1 - \delta\right) U_2. & (d)
 \end{aligned} \tag{2.10}$$

Integrating Eqs. 2.10 (a) and 2.10 (c), one obtains the following two conservation laws:

$$\begin{aligned}
 U_0 &= C_1 & (a) \\
 U_2 &= \frac{1}{2\sqrt{2}} \left(-\frac{C_1}{4}U_1 - \frac{3}{8}U_1^2 + \delta U_1\right) + C_2 & (b)
 \end{aligned} \tag{2.11}$$

where C_1 and C_2 are constants determined by the initial conditions. Here we assume at $z =$

0 $a_1(0) = E_0$ while $a_i(0) = 0$ for $i = 2, 3, 4$. The constants in Eqs. (1-11) are then given by:

$$\begin{aligned}
 C_1 &= |E_0|^2 & (a) \\
 C_2 &= \frac{1}{2\sqrt{2}} \left(\frac{5}{8}|E_0|^4 - \delta|E_0|^2\right), & (b)
 \end{aligned} \tag{2.12}$$

as a function of the normalized input power and detuning between the cores. Substituting these results into Eqs. 2.10, one would obtain the following differential equation for the parameter U_1 :

$$\dot{U}_1^2 = -\frac{9}{64}U_1^4 - \frac{2}{3}B_1U_1^3 + B_2U_1^2 + 2B_3U_1 + 2B_4, \quad (2.13)$$

where $B_1, B_2, B_3,$ and B_4 are defined as

$$\begin{aligned} B_1 &= \frac{9}{32}C_1 - \frac{9}{8}\delta \\ B_2 &= -\frac{C_1^2}{16} + \frac{C_1}{2}\delta + \frac{3\sqrt{2}}{2}C_2 - \delta^2 - 8 \\ B_3 &= \frac{\sqrt{2}}{2}C_1C_2 - 2\sqrt{2}\delta C_2 \\ B_4 &= \frac{9}{128}C_1^4 + \frac{B_1}{3}C_1^3 - \frac{B_2}{2}C_1^2 - B_3C_1. \end{aligned} \quad (2.14)$$

The differential Eq. 2.13 can be solved analytically in terms of Jacobi elliptic functions [46–48]:

$$U_1(Z) = \frac{r_1B + r_2A - (r_1B - r_2A)cn(U, k)}{A + B + (A - B)cn(U, k)}, \quad (2.15)$$

where r_1 and r_2 are real, while r_3 and r_3^* are complex conjugate roots of the fourth order polynomial of Eq. 2.13, from which A and B are determined:

$$\begin{aligned} A^2 &= \left(r_1 - \frac{r_3+r_3^*}{2}\right)^2 - \frac{(r_3-r_3^*)^2}{4} \\ B^2 &= \left(r_2 - \frac{r_3+r_3^*}{2}\right)^2 - \frac{(r_3-r_3^*)^2}{4}. \end{aligned} \quad (2.16)$$

Moreover, U is related to the elliptic integral of the first kind $F(\varphi, k)$ and the normalized propagation distance Z by $U = F(\pi, k) - \frac{3Z}{8g}$, with $k^2 = \frac{(r_1-r_2)^2-(A-B)^2}{4AB}$ being the square of the elliptic modulus and $g = (AB)^{-1/2}$. In order to show the consistency of this analytical

solution, we compared it with the results obtained from numerically solving Eqs. 2.14. Fig. 7 summarizes these results, indicating the consistency of this analytical solution.

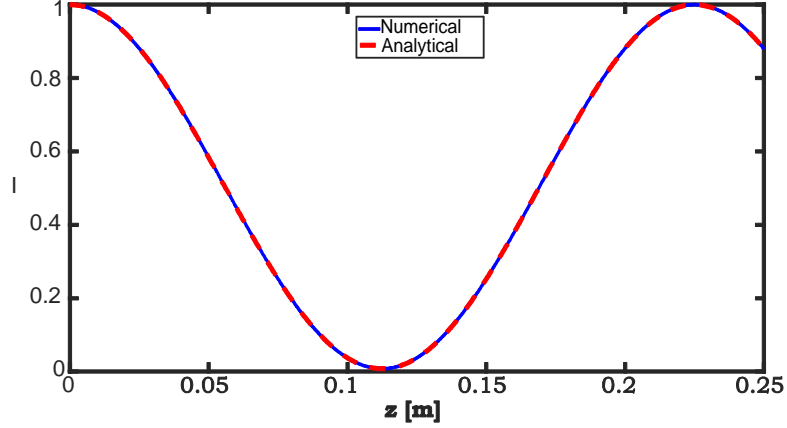


Figure 7 Comparison between analytical and numerical solutions for the light intensity evolution in the first core of the twisted four-core fiber structure.

A possible silica-based four-core arrangement where one can observe the aforementioned Aharonov-Bohm tunneling suppression is comprised of cores with radii equal to $R = 4.5 \mu\text{m}$ while the spacing between elements is $D = 24 \mu\text{m}$. The operating wavelength is assumed to be $\lambda_0 = 1550 \text{ nm}$ and the numerical aperture of each element is 0.1. The structure is twisted around its central axis with a pitch of $\Lambda = 1.4 \text{ cm}$, corresponding to $\phi = \pi/4$. In order to evaluate the coupled mode results presented, we use beam propagation method to monitor the intensity evolution in each core along the propagation axis for different powers launched into the core #1. The results are summarized in Fig. 8. These dynamics clearly indicate that the differential phase between the two light channels is left unchanged even under highly nonlinear conditions. Consequently, the quenching of the coupling can be preserved. At considerable higher power levels ($\sim 10 \text{ kW}$), the nonlinearity starts to dominate the coupling effects. As a result, a discrete

soliton is created on site 1, which further reduces energy transfer to the nearest cores (#2, #4). Even in this highly localizing regime, the topological phases are left intact. Finally, we examined the robustness of the effect with respect to the detuning of the cores #2 and #4. Figure 9 shows the results when there is a detuning of $\delta = 0.8$ between these channels. Although deviation from the ideal case of Fig. 8 is observed, it is evident that the effect in general persists such a perturbation in the structure, which can be attributed to the topological nature of the Aharonov-Bohm phase.

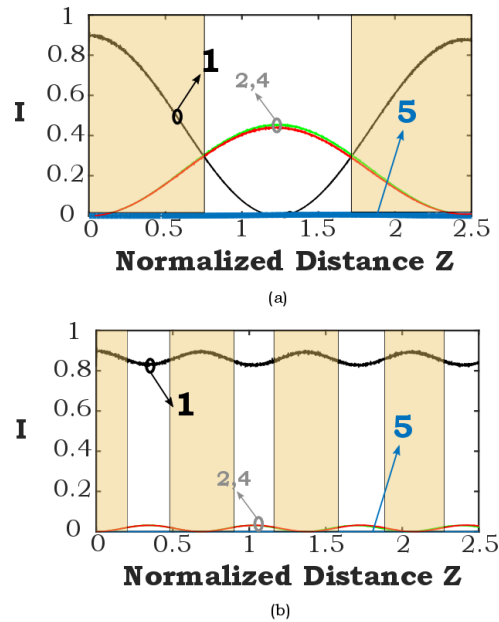


Figure 8 Beam propagation analysis of the twisted four-core fiber structure: intensity evolutions for (a) low and (b) high input powers.

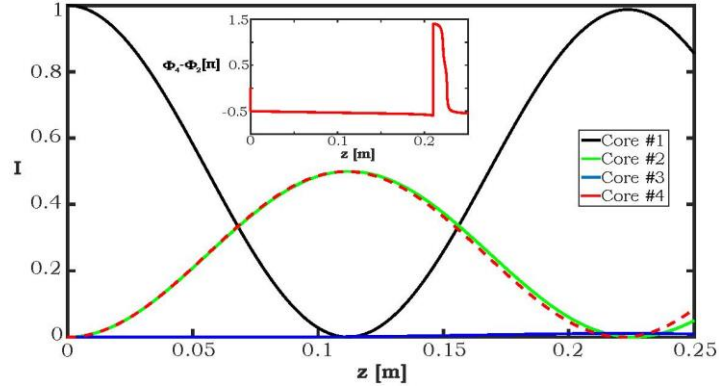


Figure 9 The robustness of the effect against nonuniformity, when core 2 is detuned from the rest of the structure by $\delta = 0.8$.

2.3. Observation of twist-induced geometric phases and inhibition of optical tunneling via Aharonov-Bohm effect

Quantum tunneling plays a central role in a number of intriguing phenomena in physics [49–53]. An archetypical manifestation of this quantum effect is the possibility of electron tunneling between multiple quantum wells when separated by potential barriers. Interestingly, on many occasions, even this simple class of systems can exhibit some unexpected quantum behaviors. For instance, complete quenching of coherent quantum tunneling can be achieved by appropriately imposing a time-harmonic drive to a double-well potential or other more complex lattice systems [54–56]. Another intriguing process is that arising from the topological restoration of energy degeneracies associated with bound states. These effects can reveal themselves in multiple quantum wells that are arranged on a closed loop, when threaded by a constant magnetic flux of certain quantized magnitudes [21]. This occurs due to the interference between degenerate electronic wavefunctions, when a nonzero Aharonov-Bohm (AB) phase is accumulated [22,23]. However, despite early theoretical efforts, an experimental observation of this latter effect is still

lacking, as of yet, within the context of solid-state physics - primarily due to practical challenges associated with the need for ultrahigh magnetic fluxes.

In recent years, the realization of synthetic gauge fields in physical settings involving neutral entities has provided a flexible platform to observe dynamics similar to those arising from the interaction of electrons with magnetic fields [57–59]. In general, such artificial magnetism can be achieved through either dynamic temporal/spatial modulation of the couplings [10,13,14], or via the use of geometric phases [60,61]. So far, this artificial magnetism has led to the demonstration of photonic topological insulators in both passive [14,15,30,62] and active arrangements [63,64], Landau levels for photons [65,66], as well as quantum many-body effects [67,68]. An important advantage offered by such schemes is the possibility for experimental demonstrations of a certain class of quantum phenomena without invoking magnetic fields, something that would have been otherwise impossible within the context of condensed matter physics. In optics, perhaps the earliest demonstration of a geometric phase is that associated with polarized light [69]. This arises when the polarization state of light follows a closed contour on the Poincaré sphere. As a result, the corresponding electric field amplitude acquires a geometric phase, known as the Pancharatnam-Berry phase [69,70]. Similar effects can also occur for linearly polarized light [20] or speckle patterns in a multimode optical fiber [71,72], when the direction of propagation varies in space.

In this section, we experimentally demonstrate an optical geometric phase, which is associated with photon tunneling in a twisted multicore fiber structure. We show that this form of geometric phase results from a constant rotation in the local frame of the fiber, and appears in a chiral manner in the corresponding coupling coefficients between adjacent cores. Thus far, twisted photonic crystal fibers have been employed to demonstrate coreless light guiding, optical activity, as well

as orbital angular momentum conservation [73–75]. Alternatively, in our study, we employ the twist-induced geometric phase to realize a synthetic magnetic field for the photon coupling between nearest-neighbor light channels. As proposed in recent studies [11,43], this is analogous to the Aharonov-Bohm effect associated with electron dynamics in the presence of a magnetic flux. We further exploit this analogy to demonstrate the Aharonov-Bohm suppression of light tunneling in a four-core twisted optical fiber. While this latter effect was originally predicted in the context of quantum electronics [21], its experimental observation has so far remained elusive due to the requirement of strong magnetic fields. In this regard, it is only recently that an experimental observation of this type has been reported in a system involving ultracold Ca ions in a linear Paul trap [76]. In our experiments, we investigate the effect of different twist rates, emulating synthetic gauge fields of varying magnitudes. In this respect, the conditions for a complete tunneling inhibition are investigated, both theoretically and experimentally. Our experimental results are in good agreement with those expected from theory for different twist rates. Moreover, we study the behavior of this same arrangement under high power conditions - where nonlinear effects start to antagonize the coupling mechanisms in the multicore system. In this highly nonlinear regime, we find that the suppression of tunneling still persists – a direct byproduct of the topological nature of the AB geometric phase. Finally, even in the case where each core is multimoded, we demonstrate that the AB inhibition of tunneling occurs in a universal fashion. In other words, this same process can totally eliminate the coupling for all higher-order modes.

2.3.1 A twisted multicore fiber platform for realizing synthetic magnetic fields for photons

In order to demonstrate AB suppression of light tunneling because of geometric phase effects, we fabricated a four-core optical fiber structure as shown in the inset of Fig. 10. Each of the four circular cores is coupled to its nearest neighbors, while a fluorine-doped refractive index depression in the middle of the structure eliminates any cross-channeling effects between opposite cores (see section 2.3.5). An artificial gauge field is then imposed on this system after twisting the multicore fiber. In this case, the evolution of the optical modal field amplitudes is described by a paraxial wave equation, expressed in the twisted local frame, in a way analogous to that associated with electron wavefunctions in the presence of a magnetic field [11,61,77] (Fig. 10). In quantum mechanics, in the presence of a uniform magnetic field, a gauge transformation through Peierls substitution is known to reduce the electron dynamics to those expected under conventional zero-field conditions. This result can be directly extended in more complicated settings such as for example atomic lattices. By treating this configuration within the tight-binding formalism, one can then show that the magnetic field now manifests itself in the form of complex coupling coefficients, having phase factors given by the Peierls integral [78]. Similarly, in a twisted multicore fiber configuration, the coupling coefficients appearing in the coupled mode equations are accordingly modified as $\kappa_{mn}e^{i\varphi_{mn}}$, where κ_{mn} represents the coupling or tunneling strength between subsequent cores in the absence of twisting, while the pertinent phase factor is given by:

$$\varphi_{mn} = k_0 \int_{\vec{r}_m}^{\vec{r}_n} \frac{1}{2} \vec{r} \times \vec{B}_{eff} \cdot \vec{dl}, \quad (2.17)$$

where $\vec{B}_{eff} = -2n_0\epsilon\hat{z}$ is the effective magnetic field induced by twisting, and $\epsilon = 2\pi/\Lambda$ is the angular twist rate. Λ denotes the spatial pitch associated with this helical structure, k_0 represents the free-space wavenumber, n_0 is the refractive index of the cladding region, and $\vec{r}_{m,n}$ stands for

the positions of the neighboring cores m, n . Under these conditions, the evolution of the modal field amplitudes E_n within the cores are given by $id|\psi\rangle/dz + H|\psi\rangle = 0$, where $|\psi\rangle = [E_1, E_2, E_3, E_4]^T$ represents a complex state vector whose evolution is subjected to a Hamiltonian H that is given by:

$$H = \begin{pmatrix} \beta_1 & \kappa e^{-i\phi} & 0 & \kappa e^{i\phi} \\ \kappa e^{i\phi} & \beta_2 & \kappa e^{-i\phi} & 0 \\ 0 & \kappa e^{i\phi} & \beta_3 & \kappa e^{-i\phi} \\ \kappa e^{-i\phi} & 0 & \kappa e^{i\phi} & \beta_4 \end{pmatrix}. \quad (2.18)$$

In Eq. 2.18, β_n stands for the propagation constants of the individual cores, κ is the magnitude of the nearest neighbor coupling coefficient, while $\phi = (k_0 n_0 \epsilon D^2)/2$ represents the Aharonov-Bohm tunneling phase introduced by the twist, when the core distance between successive sites is D , and $\epsilon = 2\pi/\Lambda$. In the four-core structure prepared, all cores are identical, and so are the respective propagation constants β_n . In this case, the β terms can be readily eliminated from the evolution equations through a trivial gauge transformation. As we will see however, this is no longer valid under nonlinear conditions.

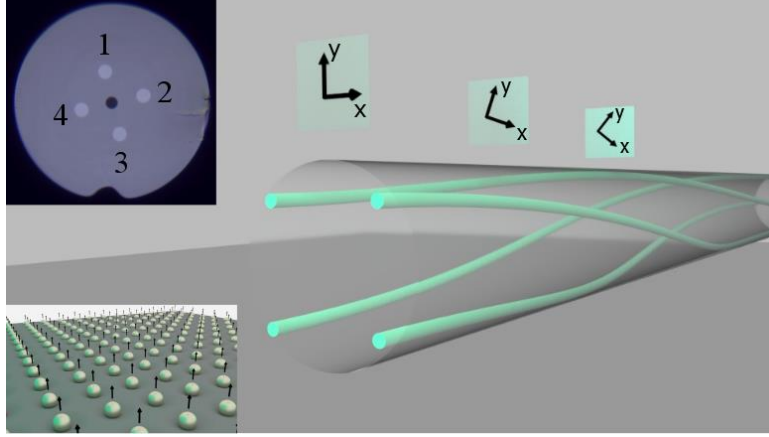


Figure 10 Twisted fiber structures as a platform for realizing synthetic magnetic fields for photons. A twisted four-core optical fiber in which the photon tunneling evolution dynamics are analogous to those expected from electrons in the presence of a magnetic field. The constantly rotating local transverse coordinates are depicted at three different planes. The top inset shows a microscope image of the input facet of the four-core fiber used in our experiments. The low-index fluorine-doped core is clearly visible at the center of the fiber. The bottom inset depicts a schematic of a two-dimensional atomic lattice in the presence of a static perpendicular magnetic field (arrows), where a tight-binding formalism can be utilized to describe the electronic band structure after a Peierls substitution.

2.3.2 Controlling and suppressing optical tunneling via twist-induced geometric phases

Equation 2.18 clearly suggests that photon tunneling in a twisted multicore fiber arrangement is accompanied by a geometric phase accumulation, akin to that expected in electron dynamics from a path-dependent AB phase. In order to experimentally observe the ϕ phase in the four-core fiber structure, we initially excite core #1 with coherent light from an external cavity laser, operating at $\lambda = 1550 \text{ nm}$ with an output power of $\sim 1 \text{ mW}$. The coupling length between successive cores is estimated to be $L_c \approx 9 \text{ cm}$. We then monitor the optical power coupled to the opposite core #3, as we vary the magnitude of the effective magnetic field (resulting from different twist rates). At the same time, the power levels in cores #2 and #4 are also recorded. It is important

to note that the multicore fiber used here is designed in such a way that at $\lambda = 1550 \text{ nm}$ only the fundamental LP_{01} mode is supported by each of the individual cores (section 2.3.5). Figure 11 shows experimental results where the output intensity from core #3 is plotted against the AB phase ϕ . In this same figure, the expected theoretical behavior (section 2.3.5) as obtained after directly solving the dynamical evolution equations is also presented. These observations indicate that the AB-like suppression of light tunneling from core #1 to #3 occurs when the gauge field corresponds to $\phi = \pi/4$. This is formally analogous to AB suppression of tunneling for electrons in the presence of a specific magnetic flux. These results provide the first observation of this intriguing effect in an optical setting.

2.3.3 Impact of nonlinearity on AB tunneling inhibition

We further explore how the aforementioned AB-like suppression of tunneling is affected by the Kerr nonlinearity of these silica multicore fibers. In this respect, we launch $\sim 400 \text{ ps}$ high intensity pulses at $\lambda = 1064 \text{ nm}$ from a Q-switched microchip laser into core #1. At this wavelength, the fiber cores in our structure support LP_{11} modes in addition to the fundamental LP_{01} . Because of mode confinement, the LP_{11} modes are very strongly coupled at 1064 nm , while the LP_{01} are virtually uncoupled. The initial ratio between the powers launched in LP_{01} and LP_{11} at core #1 is adjusted by cleaving the input facet of the fiber at an angle. In this experiment, the sole purpose of exciting the fundamental LP_{01} mode is to introduce a variable “energy” detuning $\Delta\beta_{NL} = k_0 n_2 |E_{max}|^2$ in the cores – thus allowing us to study how the nonlinearity n_2 impacts the inhibition of tunneling dynamics of the LP_{11} modes. This is achieved through cross-phase modulation effects in each core. To observe these effects, we performed intensity measurements both at low $\sim 500 \text{ W}$ and high $\sim 6 \text{ kW}$ power levels (section 2.3.5). Figure 12 depicts the output

intensity profiles at the end of the four-core fiber, for different twist-induced phases ϕ . As indicated by these results, at $\phi = \pi/4$, the AB-like inhibition of tunneling between opposite cores still takes place regardless of the optical power exciting this system. In agreement with previous theoretical studies, these observations suggest that this process remains unaffected even under highly nonlinear conditions [43]. This robustness can be understood through a formal perturbation analysis (section 2.3.7), indicating that to first-order any $\Delta\beta$ variations (linear or nonlinear) within the four cores do not affect the twist-induced degeneracy between the two groups of supermodes at $\phi = \pi/4$. This faithful tunneling inhibition is attributed to the topological nature of this optical Aharonov-Bohm phase. Finally, as the optical power injected in the first core increases, a discrete soliton forms around this waveguide channel - further suppressing any tunneling of light to the nearby cores, as also evident in Fig. 12.

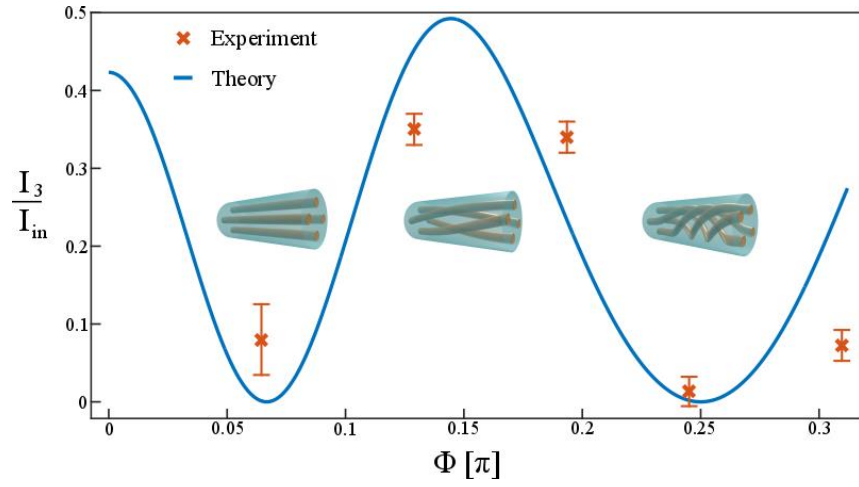


Figure 11 Dependence of optical tunneling dynamics on the AB phase. Normalized light intensity at the output of core #3 for different values of the AB phase ϕ (as induced by different twist rates). In all cases, core #1 is excited at the input with CW laser light at $\lambda = 1550 \text{ nm}$. Theoretical results corresponding to the same set of parameters are also provided for comparison. At $\phi = \pi/4$, the third core always remains dark, clearly indicating AB tunneling suppression.

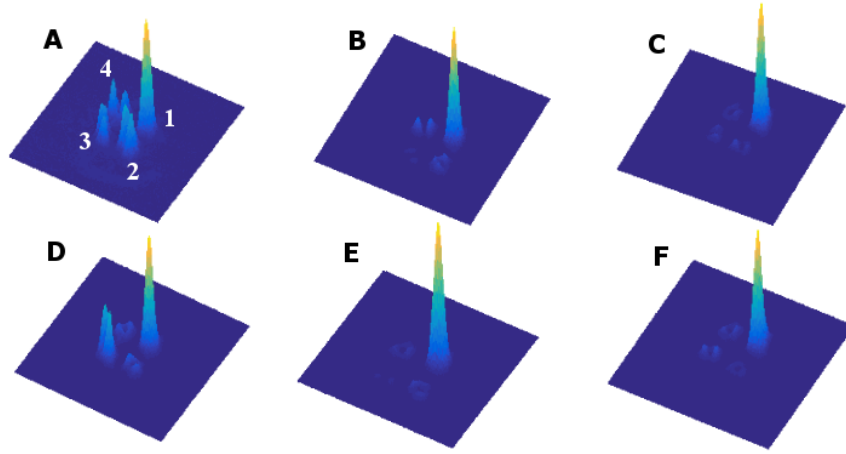


Figure 12 AB inhibition of tunneling in the presence of optical nonlinearities. Output light intensity profiles from a twisted, 24 cm long, four-core fiber when only core #1 is quasi-linearly excited for (A), $\phi = 0$ (no twist), (B), $\phi = \pi/4$, and (C), $\phi \approx 0.27\pi$. In (A-C), the pulses used had a peak power $\sim 500W$ at $\lambda = 1064 \text{ nm}$. Plots (D-F) show similar results when the input peak power is $\sim 6kW$ and hence nonlinear Kerr effects are at play. It is evident that the coupling between cores #1 and #3 is completely suppressed in both cases (B,E), regardless of the power levels used, indicating an immunity of the AB tunneling suppression against nonlinear index changes. For higher input powers (D-F), the self-focusing nonlinearity further suppresses light coupling, even among adjacent cores. The inset on the left depicts numbers in panel (A) depict the relative arrangement of the four cores in this particular experiment.

2.3.4 Suppression of tunneling in higher-order spatial modes

Of interest would be to also investigate the universality of this class of effects even in multimode environments. To do so, we used a CW input excitation at $\lambda = 665 \text{ nm}$ where each core can now support four different sets of modes ($LP_{01}, LP_{11}, LP_{21}, LP_{02}$). The input power used was $\sim 2 \text{ mW}$ so as to ensure linear conditions. For this set of parameters, the highest-order propagating mode incited in this system was LP_{02} . Our simulations indicate that while the coupling coefficients associated with this mode are significant, all other modes exhibit negligible couplings, at least for length scales involved in our experiment. This is in agreement with experimental observations

(section 2.3.5). To study the prospect for Aharonov-Bohm inhibition of tunneling in this multimode case, we again excite the first core while we record the output intensity patterns corresponding to different values of ϕ . These results are summarized in Fig. 13, where it is clearly evident that the tunneling suppression always occurs, regardless of the number of the modes involved in each individual waveguide element.

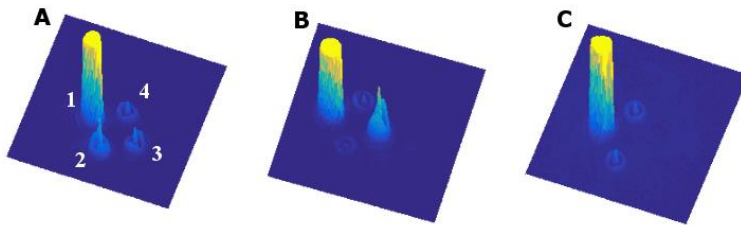


Figure 13 AB tunneling suppression for higher-order modes. Light intensity distributions at the output of a twisted four-core fiber when the higher-order LP_{02} mode is excited with CW light at $\lambda = 665 \text{ nm}$. These results are presented for (A), $\phi = 0$ (no twist), (B), $\phi \approx 0.11\pi$, and (C), $\phi = \pi/4$. Even though in the excited core #1, most of the optical power resides in the fundamental LP_{01} mode, only the LP_{02} mode appears in the remaining cores due to its higher coupling coefficient. Plot (C) clearly reveals that AB suppression of light tunneling occurs in a universal fashion, even for higher-order modes. The inset on the left depicts numbers in panel (A) depict the arrangement of the cores corresponding to these observations.

2.3.5 Experimental methods

For our experimental demonstrations, we fabricated a silica fiber consisting of four coupled cores, each with a diameter of $\sim 7.5 \mu\text{m}$ and a numerical aperture of $NA = 0.12$. The neighboring elements were separated from each other by a distance of $D = 23 \mu\text{m}$. To observe the tunneling suppression between opposite cores, it is essential that any cross couplings are suppressed so that the light propagation dynamics in the system are governed by nearest-neighbor interactions. To

achieve this, we judiciously incorporated a fluorine-doped low-index core in the center of the fiber, having a diameter of $\sim 5 \mu m$. In the absence of any twist, when core #1 is initially excited, the light intensity in cores #1 and #3 varies along the propagation distance z according to $I_1(z) = \cos^4 \kappa z$ and $I_3(z) = \sin^4 \kappa z$, as obtained after solving the dynamical modal evolution equations when $\phi = 0$. In other words, light tends to tunnel between these two waveguide channels through cores #2 and #4, in a way similar to tunneling of electrons in a multi-well potential arranged on a circular geometry.

In order to introduce an artificial “magnetic field” in our arrangement, we twisted the 4-core fiber. The fiber was excited at $\lambda = 1550 \text{ nm}$, with an external cavity laser with a CW output power of $\sim 1 \text{ mW}$. The output intensity profile from the four cores was then recorded on a CMOS-based IR beam profiling camera. Moreover, to discern different cores in the structure, we used a visible imaging camera in order to capture both the input and output facets of the fiber, once it was twisted. In general, for a given twisting rate (corresponding to an AB phase of ϕ), the light intensity in cores #1 and #3 is explicitly given by the expressions:

$$I_{1,3}(L) = \frac{1}{4} [\cos(2\kappa L \cos \phi) \pm \cos(2\kappa L \sin \phi)]^2, \quad (2.19)$$

where L is the length of the four-core fiber. Figure 11 depicts these theoretical results along with experimentally observed values for different values of ϕ when $L = 24 \text{ cm}$. As evident from Eq. 2.19, for the specific case of $\phi = \pi/4$, the third core will always remain dark, irrespective of the length L , in agreement with our experimental results.

For the nonlinear experiments, we used a Q-switched microchip laser emitting high intensity pulses of duration $\sim 400 \text{ ps}$ at a rate of 500 Hz , at $\lambda = 1064 \text{ nm}$. At this wavelength, the highest-order mode supported by the cores happens to be the LP_{11} (see section 2.3.8). Our analysis shows

that this higher order mode strongly couples nearest neighbor elements with a coupling length of $L_c \approx 2.5 \text{ cm}$, while the fundamental mode remains nearly uncoupled. As indicated in section 2.3.9, at high peak powers ($\sim 6 \text{ kW}$), the Kerr nonlinearity associated with silica in the fiber structure results in a detuning in the propagation constant of the excited core. This strong nonlinearly induced detuning starts to compete with the coupling effects, eventually forming discrete solitons in the excited core. This antagonizing effect of the nonlinearity with respect to light coupling is also evident in our experiments (Fig. 12). Finally, for $\lambda = 665 \text{ nm}$, each waveguide is multimoded and the mode with the highest coupling happens to be the LP_{02} , exhibiting $L_c \approx 10 \text{ cm}$ (see section 2.3.8). This is also evident in the experimental results where the intensity profile of the light coupled is clearly that corresponding to a radially symmetric LP_{02} mode.

2.3.6 Supermodes of twisted multicore optical fibers

In this section, we provide analytical derivations for the supermodes of a twisted multicore optical fiber, focusing on the effect of the geometric phase on the eigenstates and their corresponding eigenvalues.

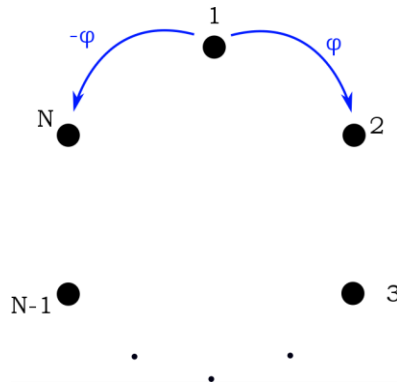


Figure 14 Twisted N-core fiber. The tunneling Aharonov-Bohm phase is depicted in the figure by φ .

As discussed in section 2.3.1, light dynamics in a twisted multicore optical fiber can be described by the following eigenvalue equation:

$$id|\psi\rangle/dz + H|\psi\rangle = 0,$$

$$H = \begin{bmatrix} \beta_1 & \kappa e^{i\phi} & \dots & 0 & \kappa e^{-i\phi} \\ \kappa e^{-i\phi} & \beta_2 & \dots & 0 & 0 \\ \vdots & \vdots & \ddots & \vdots & \vdots \\ 0 & 0 & \dots & \beta_{N-1} & \kappa e^{i\phi} \\ \kappa e^{i\phi} & 0 & \dots & \kappa e^{-i\phi} & \beta_N \end{bmatrix}, \quad (2.20)$$

where $|\psi\rangle = [E_1, E_2, \dots, E_N]^T$ represents the electric field amplitudes of an eigenstate of the system. Here we assume that all the cores are similar, hence $\beta_i = 0$. In this case, the general form of the eigenstates is given by:

$$E_n = A e^{i\mu z} e^{iQn}, \quad (2.21)$$

where μ represents the eigenvalues, while Q denotes the corresponding Bloch momenta of the eigenstates. Substituting this into the eigenvalue equation, one obtains the following form for the eigenvalues:

$$\mu = 2\kappa \cos(Q - \phi). \quad (2.22)$$

Applying periodic boundary conditions results in quantized Bloch momenta $Q = 2\pi m/N, m = 0, 1, \dots, N - 1$. It is evident that the tunneling Aharonov-Bohm phase changes the eigenvalues in this system through shifting the Bloch momentum Q , while it does not affect the form of the eigenstates. This is similar to the way a static magnetic field would modify the electronic states in a periodic 2D arrangement.

By setting $N = 4$, the eigenstates associated with the twisted four-core fiber considered in our experiments can be obtained as:

$$|\psi_0\rangle = \frac{1}{2} \begin{pmatrix} 1 \\ 1 \\ 1 \\ 1 \end{pmatrix}, |\psi_1\rangle = \frac{1}{2} \begin{pmatrix} 1 \\ i \\ -1 \\ -i \end{pmatrix}, |\psi_2\rangle = \frac{1}{2} \begin{pmatrix} 1 \\ -1 \\ 1 \\ -1 \end{pmatrix}, |\psi_3\rangle = \frac{1}{2} \begin{pmatrix} 1 \\ -i \\ -1 \\ i \end{pmatrix}, \quad (2.23)$$

while their respective eigenvalues are:

$$\mu_0 = 2\kappa \cos \phi, \mu_1 = 2\kappa \sin \phi, \mu_2 = -2\kappa \cos \phi, \mu_3 = -2\kappa \sin \phi. \quad (2.24)$$

For a twist rate corresponding to $\phi = \pi/4$, these will form two pairs of degenerate eigenmodes

$\mu_0 = \mu_1 = \sqrt{2}\kappa$ and $\mu_2 = \mu_3 = -\sqrt{2}\kappa$. In this case, if core #1 is excited at the input, the initial state of the system at $z = 0$ can be expanded in terms of the given eigenstates as:

$$|\psi_{in}\rangle = \begin{pmatrix} 1 \\ 0 \\ 0 \\ 0 \end{pmatrix} = \frac{1}{2} \sum_{i=0}^3 |\psi_i\rangle. \quad (2.25)$$

Therefore, the propagated state at an arbitrary distance z will then be:

$$|\psi(z)\rangle = \frac{1}{2} \sum_{i=0}^3 e^{i\mu_i z} |\psi_i\rangle = \frac{1}{2} \begin{pmatrix} \cos(2\kappa z \cos \phi) + \cos(2\kappa z \sin \phi) \\ i \sin(2\kappa z \cos \phi) - \sin(2\kappa z \sin \phi) \\ \cos(2\kappa z \cos \phi) - \cos(2\kappa z \sin \phi) \\ i \sin(2\kappa z \cos \phi) + \sin(2\kappa z \sin \phi) \end{pmatrix}, \quad (2.26)$$

Substituting $\phi = \pi/4$, we find:

$$|\psi(z)\rangle = \frac{1}{2} \begin{pmatrix} 2 \cos(\sqrt{2}\kappa z) \\ (i-1) \sin(\sqrt{2}\kappa z) \\ 0 \\ (i+1) \sin(\sqrt{2}\kappa z) \end{pmatrix}, \quad (2.27)$$

indicating that core #3 will always remain dark irrespective of the length of the fiber.

2.3.7 Perturbation analysis of the tunneling inhibition

In this section, we consider how small perturbations in terms of detuning of individual cores or variations in coupling coefficients between nearby cores would affect the AB tunneling inhibition effect in our four-core twisted fiber.

We first consider a diagonal perturbation in the Hamiltonian describing the structure:

$$H' = H + \Delta H_1,$$

$$H = \begin{pmatrix} 0 & \kappa e^{-i\phi} & 0 & \kappa e^{i\phi} \\ \kappa e^{i\phi} & 0 & \kappa e^{-i\phi} & 0 \\ 0 & \kappa e^{i\phi} & 0 & \kappa e^{-i\phi} \\ \kappa e^{-i\phi} & 0 & \kappa e^{i\phi} & 0 \end{pmatrix}, \quad \Delta H_1 = \begin{pmatrix} \epsilon_1 & 0 & 0 & 0 \\ 0 & \epsilon_2 & 0 & 0 \\ 0 & 0 & \epsilon_3 & 0 \\ 0 & 0 & 0 & \epsilon_4 \end{pmatrix}. \quad (2.28)$$

In this case, the first-order approximation of the perturbed eigenvalues will be:

$$\mu'_i \approx \mu_i + \langle \psi_i | \Delta H_1 | \psi_i \rangle = \mu_i + \Delta \mu_i,$$

$$\Delta \mu_i = \frac{1}{2} \begin{pmatrix} 1 & e^{iQ} & e^{i2Q} & e^{i3Q} \end{pmatrix} \begin{pmatrix} \epsilon_1 & 0 & 0 & 0 \\ 0 & \epsilon_2 & 0 & 0 \\ 0 & 0 & \epsilon_3 & 0 \\ 0 & 0 & 0 & \epsilon_4 \end{pmatrix} \frac{1}{2} \begin{pmatrix} 1 \\ e^{-iQ} \\ e^{-i2Q} \\ e^{-i3Q} \end{pmatrix} = \frac{1}{4} \sum_{i=0}^3 \epsilon_i, \quad (2.29)$$

This shows that a diagonal perturbation would lead into the same first-order correction for all the four eigenvalues. Therefore, to first-order, we still have two pair of degenerate eigenstates and hence the tunneling inhibition is preserved.

Now let us consider a perturbation in the coupling coefficients:

$$H' = H + \Delta H_2, \quad \Delta H_2 = \begin{pmatrix} 0 & \delta \kappa_{12} & 0 & \delta \kappa_{14} \\ \delta \kappa_{12}^* & 0 & \delta \kappa_{23} & 0 \\ 0 & \delta \kappa_{23}^* & 0 & \delta \kappa_{34} \\ \delta \kappa_{14}^* & 0 & \delta \kappa_{34}^* & 0 \end{pmatrix}. \quad (2.30)$$

Similar to the previous case, the first-order perturbations can be obtained as:

$$\Delta \mu_0 = \frac{1}{2} \begin{pmatrix} 1 & 1 & 1 & 1 \end{pmatrix} \Delta H_2 \frac{1}{2} \begin{pmatrix} 1 \\ 1 \\ 1 \\ 1 \end{pmatrix} = \frac{1}{2} \text{Re}\{\delta \kappa_{12} + \delta \kappa_{23} + \delta \kappa_{34} + \delta \kappa_{14}\},$$

$$\Delta \mu_1 = \frac{1}{2} \begin{pmatrix} 1 & -i & -1 & i \end{pmatrix} \Delta H_2 \frac{1}{2} \begin{pmatrix} 1 \\ i \\ -1 \\ -i \end{pmatrix} = -\frac{1}{2} \text{Im}\{\delta \kappa_{12} + \delta \kappa_{23} + \delta \kappa_{34} - \delta \kappa_{14}\},$$

$$\Delta\mu_2 = \frac{1}{2}(1 \quad -1 \quad 1 \quad -1)\Delta H_2 \frac{1}{2} \begin{pmatrix} 1 \\ -1 \\ 1 \\ -1 \end{pmatrix} = -\frac{1}{2} \text{Re}\{\delta\kappa_{12} + \delta\kappa_{23} + \delta\kappa_{34} + \delta\kappa_{14}\},$$

$$\Delta\mu_3 = \frac{1}{2}(1 \quad i \quad -1 \quad -i)\Delta H_2 \frac{1}{2} \begin{pmatrix} 1 \\ -i \\ -1 \\ i \end{pmatrix} = \frac{1}{2} \text{Im}\{\delta\kappa_{12} + \delta\kappa_{23} + \delta\kappa_{34} - \delta\kappa_{14}\}. \quad (2.31)$$

We are particularly interested in perturbations in the magnitudes of the coupling coefficients, therefore we have:

$$\delta\kappa_{12} = |\delta\kappa_{12}|e^{-i\phi}, \delta\kappa_{23} = |\delta\kappa_{23}|e^{-i\phi}, \delta\kappa_{34} = |\delta\kappa_{34}|e^{-i\phi}, \delta\kappa_{14} = |\delta\kappa_{14}|e^{i\phi}, \quad (2.32)$$

Hence:

$$\Delta\mu_0 = \frac{1}{2}(|\delta\kappa_{12}| + |\delta\kappa_{23}| + |\delta\kappa_{34}| + |\delta\kappa_{14}|) \cos \phi,$$

$$\Delta\mu_1 = \frac{1}{2}(|\delta\kappa_{12}| + |\delta\kappa_{23}| + |\delta\kappa_{34}| + |\delta\kappa_{14}|) \sin \phi,$$

$$\Delta\mu_2 = -\frac{1}{2}(|\delta\kappa_{12}| + |\delta\kappa_{23}| + |\delta\kappa_{34}| + |\delta\kappa_{14}|) \cos \phi,$$

$$\Delta\mu_3 = -\frac{1}{2}(|\delta\kappa_{12}| + |\delta\kappa_{23}| + |\delta\kappa_{34}| + |\delta\kappa_{14}|) \sin \phi. \quad (2.33)$$

As indicated by these results, we see that in general, arbitrary perturbations in the coupling strengths result in different corrections $\Delta\mu_i$. However, for the special case where $\phi = \pi/4$ which corresponds to the inhibition of the tunneling, one obtains $\Delta\mu_0 = \Delta\mu_1$ and $\Delta\mu_2 = \Delta\mu_3$, showing that the underlying degeneracy among the eigenstates in our system persists in the presence of this type of disorder. This in turn means that the AB tunneling inhibition itself is robust with respect to both diagonal and off-diagonal perturbations.

2.3.8 Coupling of the fundamental mode and higher-order modes

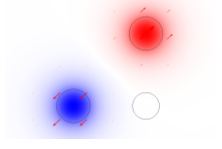
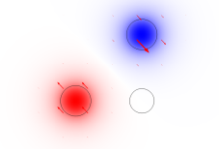
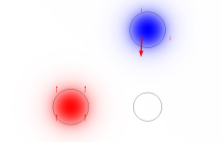
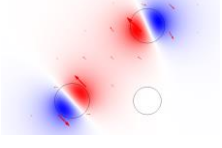
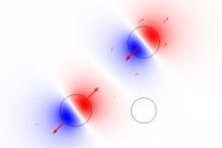
In the first set of our experiments, we used light at a wavelength of $\lambda = 1550 \text{ nm}$. In this case, the associated V number of the individual cores is:

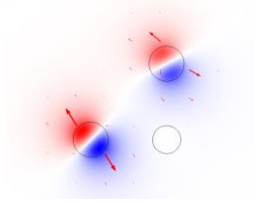
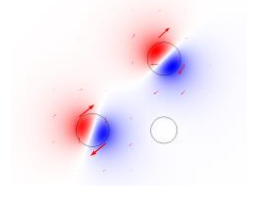
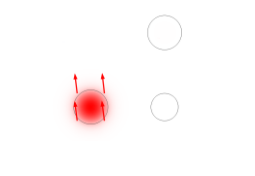
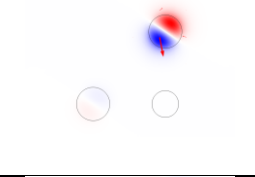
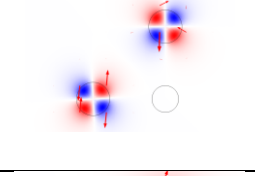
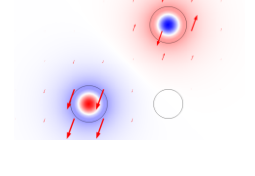
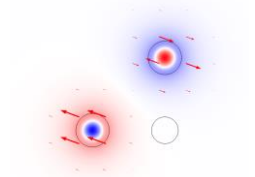
$$V = k_0 r_{core} NA = 1.8, \tag{2.34}$$

and therefore each core is single-moded in this case (LP_{01}). As we decrease the wavelength to $\lambda = 1064 \text{ nm}$ and $\lambda = 665 \text{ nm}$, this V number increases, leading to a multimode behavior within each of the light channels. Table 1 summarizes these results, where the corresponding mode profiles together with their nearest-neighbor coupling coefficients are also reported.

As mentioned in section 2.3.5, to observe the tunneling suppression between opposite cores, it is essential that cross-coupling between them is highly suppressed so that the light propagation dynamics in the system are governed by nearest-neighbor interactions. In order to achieve this, we incorporated a fluorine-doped low-index core in the center of the fiber, having a diameter of $\sim 5 \mu\text{m}$. Our simulations show that in the absence of such measures the cross-coupling is around $\sim 6\%$ of the nearest-neighbor coupling coefficients, while by introducing the refractive index suppression it is reduced to $\sim 2\%$.

Table 1 Effect of surface passivation on current devoted to surface recombination at threshold.

$\lambda = 1550 \text{ nm}$		
Mode	Coupling coefficient $\kappa [m^{-1}]$	Mode profile
LP_{01a}	16	
LP_{01b}	16	
$\lambda = 1064 \text{ nm}$		
LP_{01}	0.24	
LP_{11a}	63	
LP_{11b}	61.5	

$\lambda = 1550 \text{ nm}$		
LP_{11c}	10	
LP_{11d}	11.5	
$\lambda = 665 \text{ nm}$		
LP_{01}	0.01	
LP_{11}	0.08	
LP_{21}	0.38	
LP_{02a}	16	
LP_{02b}	16	

2.3.9 Kerr-induced detuning in high powers

As mentioned in section 2.3.5, our high power experiments were performed at $\lambda = 1064 \text{ nm}$. We used optical pulses of duration $\sim 400 \text{ ps}$ from a Q-switched microchip laser with peak powers of $\sim 500 \text{ W}$ and $\sim 6 \text{ kW}$. Therefore, Kerr induced detuning in the excited core #1 in each case will be:

$$\Delta\beta_{low} = k_0 n_2^I I_{low} \approx 4 \text{ m}^{-1} \quad (2.35)$$

$$\Delta\beta_{high} = k_0 n_2^I I_{high} \approx 48 \text{ m}^{-1}. \quad (2.36)$$

According to these, in the high optical power regime, the nonlinear induced detuning in the propagation constant of the excited core is comparable in magnitude with the coupling coefficient of the higher-order LP_{11} mode. This results in a more confinement of the light in the excited core #1, further decreasing the coupling to the other cores.

2.3.10 Coupling suppression of higher-order modes

Here we consider coupled mode analysis of the twisted fiber for higher-order modes, e.g. the LP_{11} mode arising in our nonlinear experiments. As indicated by our simulations in Table S1, the coupling between cores for higher-order modes can in general differ due to specific orientation of the corresponding mode. As shown in Fig. 15, this can be understood by noting that the coupling between nearby cores supporting e.g. LP_{11} mode is directional, leading to different couplings κ_1 and κ_2 in this case ($\kappa_1 > \kappa_2$).

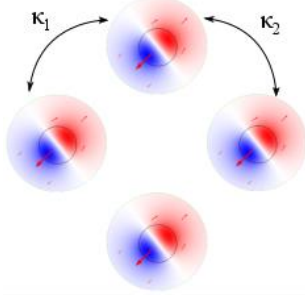


Figure 15 Inhomogeneous couplings among cores. Different coupling coefficients among various nearby cores in a four-core system for an LP_{11} mode.

Consequently, the coupled mode equations can be formulated as discussed in the main text, except that now the equivalent Hamiltonian H is given as

$$H_1 = \begin{pmatrix} 0 & \kappa_2 e^{-i\phi} & 0 & \kappa_1 e^{i\phi} \\ \kappa_2 e^{i\phi} & 0 & \kappa_1 e^{-i\phi} & 0 \\ 0 & \kappa_1 e^{i\phi} & 0 & \kappa_2 e^{-i\phi} \\ \kappa_1 e^{-i\phi} & 0 & \kappa_2 e^{i\phi} & 0 \end{pmatrix}. \quad (2.37)$$

For a twist rate corresponding to $\phi = \pi/4$, it can be shown that H_1 exhibits two pairs of degenerate eigenmodes $\mu_0 = \mu_1 = \mu_- = -\sqrt{\kappa_1^2 + \kappa_2^2}$ and $\mu_2 = \mu_3 = \mu_+ = \sqrt{\kappa_1^2 + \kappa_2^2}$, together with their associated eigenvectors:

$$|\psi_0\rangle = \frac{1}{2} \begin{pmatrix} 1 \\ -e^{-i(\frac{\pi}{4}+\theta)} \\ -1 \\ e^{-i(\frac{\pi}{4}+\theta)} \end{pmatrix}, |\psi_1\rangle = \frac{1}{2} \begin{pmatrix} 1 \\ -e^{-i(\frac{\pi}{4}-\theta)} \\ 1 \\ -e^{-i(\frac{\pi}{4}-\theta)} \end{pmatrix}, |\psi_2\rangle = \frac{1}{2} \begin{pmatrix} 1 \\ e^{-i(\frac{\pi}{4}+\theta)} \\ -1 \\ -e^{-i(\frac{\pi}{4}+\theta)} \end{pmatrix}, |\psi_3\rangle = \frac{1}{2} \begin{pmatrix} 1 \\ -e^{-i(\frac{\pi}{4}-\theta)} \\ 1 \\ e^{-i(\frac{\pi}{4}-\theta)} \end{pmatrix}, \quad (2.38)$$

where $\tan \theta = \kappa_1/\kappa_2$. Under these conditions, if core #1 is initially excited at the input, the initial state of the system at $z = 0$ can be expanded in terms of the given eigenstates as:

$$|\psi_{in}\rangle = \begin{pmatrix} 1 \\ 0 \\ 0 \\ 0 \end{pmatrix} = \frac{1}{2} \sum_{i=0}^3 |\psi_i\rangle. \quad (2.39)$$

Therefore, the propagated state at an arbitrary distance z will then be

$$|\psi(z)\rangle = \frac{1}{2} \sum_{i=0}^3 e^{i\mu_i z} |\psi_i\rangle = \frac{1}{2} \begin{pmatrix} e^{i\mu_- z} + e^{i\mu_+ z} \\ -e^{-\frac{i\pi}{4}} \cos \theta (e^{i\mu_- z} - e^{i\mu_+ z}) \\ 0 \\ -ie^{-\frac{i\pi}{4}} \sin \theta (e^{i\mu_- z} - e^{i\mu_+ z}) \end{pmatrix}, \quad (2.40)$$

indicating that core #3 will always remain dark irrespective of the length of the fiber.

2.4. Zero-DGD multicore optical fibers

In this section we consider how the properties of the individual elements of an array can affect the characteristics of the system [79]. In particular, we ask ourselves whether it is possible to eliminate the modal dispersion in a multicore fiber by judiciously adjusting the properties of the cores. It is shown that the resulting eigenvalue polynomial associated with an N -core MCF structure can be appropriately recast into $N-1$ algebraic equations whose roots can determine the features of the individual waveguide elements needed to achieve zero-DGD conditions. This procedure, based on coupled mode theory, can be employed in a versatile fashion for any MCF arrangement. A number of examples are provided to elucidate this method. By considerably restricting the search space for relevant parameters, these results can be further fine-tuned using finite element methods.

We begin our analysis by considering an N -core MCF system, as shown in Fig. 16 for $N = 6$. In this respect we assume that the propagation constants of each waveguide involved is β_l while the coupling coefficients between different sites is κ_{lm} . The evolution of the (local) modal field amplitudes U_l in this coupled array is described by the following set of equations:

$$i \frac{dU_l}{dz} + \beta_l U_l + \sum_{l \neq m} \kappa_{lm} U_m \quad (2.41)$$

where $l = 1, 2, \dots, N$. The N eigenvalues μ_j associated with the supermodes $\bar{U}_j = \bar{U}_{0j} \exp(i\mu_j z)$ of this array can then be directly obtained from the eigenvalue problem,

$$\begin{vmatrix} \beta_1 - \mu & \kappa_{12} & \cdots & \kappa_{1N} \\ \kappa_{21} & \beta_2 - \mu & \cdots & \kappa_{2N} \\ \vdots & \vdots & \ddots & \vdots \\ \kappa_{N1} & \kappa_{N2} & \cdots & \beta_N - \mu \end{vmatrix} = 0, \quad (2.42)$$

which in turn leads to the following characteristic equation:

$$\mu^N + P_{N-1}(\beta_l, \kappa_{lm}) \mu^{N-1} + P_{N-2}(\beta_l, \kappa_{lm}) \mu^{N-2} + \cdots + P_0(\beta_l, \kappa_{lm}) = 0. \quad (2.43)$$

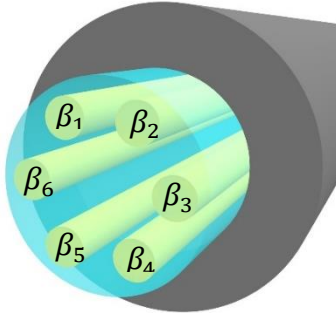


Figure 16 A hexagonal MCF structure involving six dissimilar cores.

Here $P_j(\beta_l, \kappa_{lm})$ represent polynomial functions of the propagation constants and coupling coefficients. At this point we emphasize that both parameters β_l and κ_{lm} are dispersive, i.e. they depend on the optical angular frequency ω . If all the waveguide channels are identical, in which case they exhibit the same propagation constant β_0 , then it is straightforward to show that the resulting eigenvalues are only functions of the inter-site couplings, i.e. $\mu_j = \beta_0 + f_j(\kappa_{lm})$, where f_j represents again a polynomial function. In this particular case DGD can be eliminated only if $d\kappa_{lm}/d\omega = 0$, that is only possible under the conditions mentioned above [80]. Otherwise, a

uniform array will suffer from considerable differential group delay levels. Hence, in order to eliminate DGD one has to resort to multicore fiber designs where the constituent waveguide elements are dissimilar. This fact has been recently recognized in connection with zero-DGD two-core structures with unequal radii [81].

Evidently, under zero-DGD conditions, the eigenvalues of the MCF configuration should satisfy the following relation:

$$\frac{d\mu_1}{d\omega} = \frac{d\mu_2}{d\omega} = \dots = \frac{d\mu_N}{d\omega}, \quad (2.44)$$

where all derivatives are evaluated at the central frequency $\omega = \omega_0$. Equation 2.44 ensures that the group velocities of all N supermodes are equal. By differentiating Eq. (1-42) with respect to ω we obtain:

$$\mu^{N-1} \left(N \frac{d\mu}{d\omega} + \frac{dP_{N-1}}{d\omega} \right) + \sum_{k=0}^{N-2} \left[(k+1)P_{k+1} \frac{d\mu}{d\omega} + \frac{dP_k}{d\omega} \right] \mu^k = 0. \quad (2.45)$$

Equation 2.45 represents a polynomial equation in μ of degree N-1. For Eq. 2.45 to be true for all possible eigenvalues μ , it is necessary that the coefficients of all the terms in this polynomial vanish, i.e. $(k+1)P_{k+1}\mu' + P'_k = 0$, where $\mu' = d\mu/d\omega$, etc. By applying this condition to the first term in Eq. 2.45 and given that $P_{N-1} = -\sum_{l=1}^N \beta_l$ we find that:

$$\frac{1}{v_{gMCF}^{-1}} = \frac{1}{N} \left(\sum_{l=1}^N \frac{1}{v_{gl}^{-1}} \right), \quad (2.46)$$

where $v_{gMCF}^{-1} = \mu'$ and $v_{gl}^{-1} = \beta'_l$. Equation 2.46 directly implies that the expected common group speed in this MCF system should be in fact the average of all the group velocities associated with the different fiber cores involved. In other words, the common group velocity of all the supermodes

in this zero-DGD MCF must be $v_{g_{MCF}}$. From Eq. 2.45 and after using this latter result, one obtains

the following system of N-1 algebraic equations, where $k = 0, 1, \dots, N - 2$.

$$\frac{(k+1)P_{k+1}}{N} \left(\sum_{l=1}^N \frac{d\beta_l}{d\omega} \right) + \frac{dP_k}{d\omega} = 0. \quad (2.47)$$

In general, one can introduce the dissimilarity between cores (needed for zero DGD) either by employing different index profiles, by using unequal dimensions, or both. Here, to demonstrate this method, we assume that the core index profiles are all of the same step index type, while we allow the waveguide channel radii to vary around the radius of the first core, which here is held constant. In other words, we use the radii of the N-1 waveguides as variables to solve the N-1 equations of 2.47. The coupling coefficients between different sites l, m are calculated using the following relation [82]:

$$\kappa_{lm} = (2\Delta_m)^{\frac{1}{2}} \frac{U_l U_m}{R_l V_l} \times \frac{K_0 \left(\frac{W_l d_{lm}}{R_l} \right)}{K_1(W_l) K_1(W_m)} \times \left\{ \frac{\overline{W}_l K_0(W_m) I_1(\overline{W}_l) + W_m K_1(W_m) I_0(\overline{W}_l)}{\overline{W}_l^2 + U_m^2} \right\}, \quad (2.48)$$

where $\overline{W}_l = W_l R_m / R_l$, $I_m(x)$ and $K_m(x)$ are modified Bessel functions of the first and second kind, and R_l are the core radii. Moreover, $\Delta_m = (n_{1,m} - n_{2,m}) / n_{1,m}$ is the normalized index difference, $V_l = k_0 R_l n_{1,l} \sqrt{2\Delta_l}$ represents a dimensionless V number for core l , while $W_l = R_l (\beta_l^2 - k_0^2 n_{2,l}^2)^{1/2}$, $U_l = R_l (k_0^2 n_{1,l}^2 - \beta_l^2)^{1/2}$, where $n_{1,m}$ and $n_{2,m}$ are the core and cladding refractive indices, k_0 is the free-space wavenumber, and d_{lm} is the distance between core centers at sites l and m .

Clearly, for a given set of characteristics, both quantities β_1 and β_1' associated with the first waveguide are known. Therefore, the only unknowns in the system of Eqs. 2.47 are the propagation constants of the remaining N-1 cores and their derivatives with respect to frequency, which are of course functions of the characteristics of the individual waveguides comprising the structure. Here we use the core radii as variables even though in general one can also exploit other degrees of freedom (index contrast, index profile, etc.). It is important to emphasize at this point that the polynomials associated with Eq. 2.47 directly involve the propagation constants β_l (which are inherently large) -hence the resulting eigenvalues μ_j are of the same order. This in turn complicates the numerical search for roots. To alleviate this problem, we rewrite each propagation constant in terms of a reference value, i.e. $\beta_l = \delta\beta_l + \bar{\beta}$, where in our case $\bar{\beta} = k_0(n_1(\omega) + n_2(\omega))/2$. As a result, the common reference value $\bar{\beta}$ drops out from these equations, and instead, the polynomials $P_j(\delta\beta_l, \kappa_{lm})$ now depend only on the smaller differential propagation constants $\delta\beta_l$. This latter normalization further facilitates the numerical search for solutions. In this normalized frame, the eigenvalues μ_j are also rescaled with respect to the reference floor. With this in mind, we computationally search for the N-1 radii capable of simultaneously satisfying the N-1 Eqs. 2.47. In all cases, we seek solutions where each waveguide still remains single-moded, i.e. with a V number less than 2.4. Note that our results, however close to the optimum design, are still not exact due to the approximations inherent in coupled mode theory. Nevertheless, once the search space for relevant core parameters is significantly narrowed down using our approach, the final MCF design can be further fine-tuned using finite element methods.

To demonstrate our method, we first consider a four-core fiber design. The structure is composed of step-index waveguide elements with centers placed on the vertices of a $16\mu\text{m} \times 16\mu\text{m}$ square (Fig. 17). Here we set the radius of the first core to be $R_1 = 4.42 \mu\text{m}$ and we then determine the

remaining cores so that the three equations (of Eq. 2.47) are simultaneously satisfied. For this case, the core radii are found to be: $R_2 = 3.929 \mu m$, $R_3 = 4.095 \mu m$ and $R_4 = 4.219 \mu m$. At $\lambda_0 = 1550 \text{ nm}$, the resulting DGD between any two of the four supermodes (or eight including polarizations) varies between 0.8 and 7.7 ps/km . In other words, zero DGD conditions can only be established provided that all elements are quite dissimilar with respect to each other. The mode intensity profiles of the corresponding supermodes are depicted in Fig. 18.

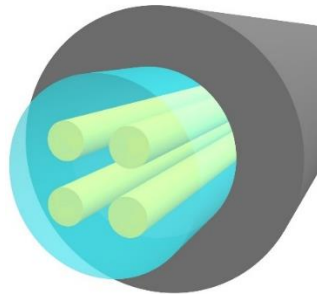


Figure 17 Schematic of a four-core MCF.

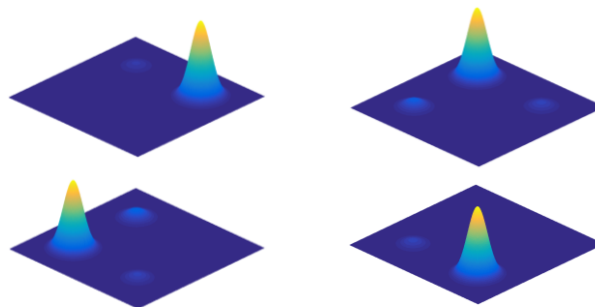


Figure 18 The four supermode intensity profiles of an ultra-low DGD four-core MCF design.

For the scenario explored above, Fig. 18 clearly indicates that each supermode in this four-element system mostly resides in one core-with little penetration into the other three. This

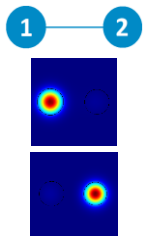
characteristic could be desirable in terms of multiplexing or demultiplexing these modes, in particular in connection to MIMO processing. The effective mode indices corresponding to the four modes shown in Fig. 18 are 1.4463, 1.4462, 1.4461 and 1.4459, while the core and cladding refractive indices are taken here to be 1.449 and 1.444 respectively. Our results suggest that zero DGD is possible even though the different supermode propagation constants are clustered away from the cladding radiation modes of the structure. To assess the efficacy of our method, we compare the DGD values we found to those associated with a similar four-core arrangement, comprised of identical waveguides with a radius of $R_1 = 4.42 \mu m$ (all other characteristics remain the same). For this uniform array, the maximum DGD was 2.3 ns/km, which is nearly 300 times higher than the values obtained for the aforementioned design.

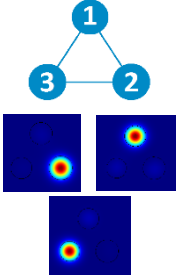
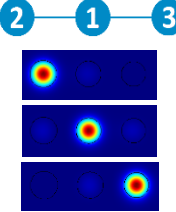
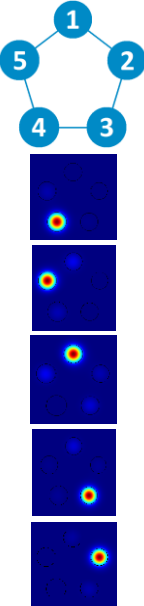
The method presented here is general and can be applied to MCFs with different numbers of cores and geometries. The results for MCFs with two, three, five and six cores, of different geometries, are presented in Table 1. In these examples, all the parameters of the MCF structure (e.g. core and cladding refractive index, center frequency, spacing between elements, etc.) are the same as for the four-core case studied above, and the radii of $N-1$ cores are chosen as unknowns in simultaneously solving the $N-1$ equations of 2.47. The table provides the V numbers of the individual cores in isolation. The maximum expected value of DGD between the various supermodes of the structure, as well as the mode intensity profiles for each supermode is also presented. As in the four-core example considered before, even in more complex geometric patterns, all the core elements must be different when taken in sequence, to achieve low DGD conditions. Moreover, each supermode tends to primarily occupy one waveguide element. Other MCF systems can be analyzed in a similar fashion based on the analytical scheme suggested. Even

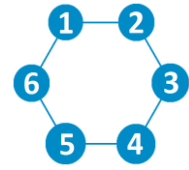
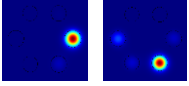
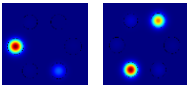
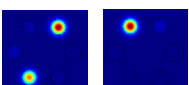
though in our examples we considered step-index elements so as to demonstrate this approach, in principle one can apply the same methodology to more involved graded index cores provided the respective propagation constants and coupling coefficients are evaluated as a function of wavelength.

Moreover, we have considered how the DGD varies as a function of wavelength for the aforementioned designs. As an example, we have numerically obtained the three DGD curves associated with the equilateral three-core design in Table 2. This response was determined across the C-band, around the operating wavelength of $\lambda_0 = 1550 \text{ nm}$ (Fig. 19). Our computations indicate that throughout the C-band, the maximum DGD remains always below 28.4 ps/km . Compared to other equilateral equal-core step-index designs of a similar index contrast, our results show a ten-fold improvement in DGD variations. We note that for this particular design the DGD curves happen to be polarization insensitive. Similar conclusions can be drawn for the other designs in Table 2.

Table 2 Low DGD MCF structures of different geometries

Configuration	Maximum DGD	Waveguide V numbers
	0.5 ps/km	$V_1 = 2.20$ $V_2 = 2.06$

Configuration	Maximum DGD	Waveguide V numbers
	0.6 ps/km	$V_1 = 2.20$ $V_2 = 2.37$ $V_3 = 2.10$
	0.5 ps/km	$V_1 = 2.20$ $V_2 = 2.32$ $V_3 = 2.10$
	10.2 ps /km	$V_1 = 2.17$ $V_2 = 2.04$ $V_3 = 2.15$ $V_4 = 2.37$ $V_5 = 2.24$
	11.0 ps /km	$V_1 = 2.10$ $V_2 = 2.20$ $V_3 = 2.00$ $V_4 = 2.09$

Configuration	Maximum DGD	Waveguide V numbers
		$V_5 = 2.32$ $V_6 = 2.22$
		
		
		

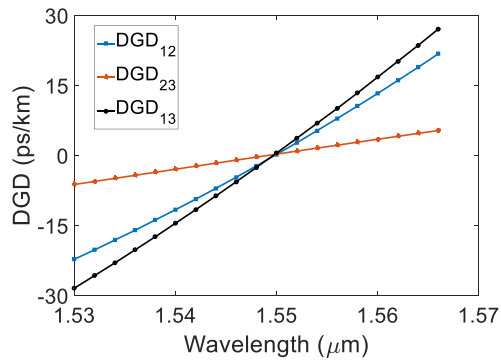


Figure 19 Variation of DGD over the C-band for a three-core fiber design.

2.5. Summary

According to the Aharonov-Bohm effect electron beams acquire a path-dependent phase in their corresponding wavefunctions in the presence of a nonzero magnetic flux [22,23]. This phase shift is not limited to conducting electrons, but also arises within the context of quantum tunneling [21]. Even though the AB effect has been observed for electrons in a superconducting or conductive

platform [83–85], its observation in quantum well tunneling settings has so far remained out of reach, mainly due to the demand for high magnetic fluxes- which are experimentally inaccessible. Quite recently, a relevant observation has been reported [76], where a linear Paul trap was used to establish a bistable potential with two degenerate eigenstates for Ca ions. A magnetic field was then applied to the structure, and the tunneling rate between the corresponding degenerate states was found to be affected by the associated magnetic flux.

In optics, as originally shown by Pancharatnam, a cyclic change in the polarization of a light beam will in general lead to a phase shift accumulated by its corresponding electric field amplitude [69]. This can be viewed as the equivalent of the AB phase, where the magnetic flux is now replaced by the solid angle subtended by the corresponding cyclic curve on the Poincaré sphere for propagating photons [70]. On the other hand, the structure implemented here in our study is analogous to the AB effect for tunneling electrons, as predicted in recent theoretical studies [43]. Here the uniform twist along a circular multi-core fiber acts as a synthetic magnetic field for photon-tunneling between adjacent cores. Accordingly, the magnitude of this gauge field can be conveniently varied through mechanical twisting of the fiber, until a complete suppression of coupling between the two opposite cores can be achieved.

As indicated by our experimental results (Fig. 12), the AB tunneling phase in the twisted multicore structure remains invariant regardless of the presence of optical nonlinearity. Moreover, as confirmed by the observations presented in Fig. 13, this same effect happens in a universal manner even for higher-order modes in our optical fiber platform. We would like to emphasize here that local defects in the individual waveguide channels, something inevitable in any experimental realization, would not significantly affect our results [43]. In other words, this AB-

induced tunneling inhibition effect happens to be robust against perturbations. This is attributed to the topological nature of the AB phase, as can be confirmed by perturbation analysis (section 2.3.7). Our observations suggest that similar twisted fiber systems can be envisioned as viable platforms for studying effects akin to those arising from the interaction of electrons with magnetic fields-especially in connection with topological phenomena.

CHAPTER 3: TOPOLOGICAL INSULATOR LASERS

3.1. Introduction

Topological insulators are a phase of matter featuring an insulating bulk while supporting conducting edge states [3,24,26]. Remarkably, edge-state transport in topological insulators is granted topological protection, a property stemming from the underlying topological invariants [3]. For example, in two-dimensional systems the ensued one-way conduction along the edge of a topological insulator is by nature scatter-free - a direct outcome of the nontrivial topology of the bulk electronic wavefunctions [26]. Although topological protection was initially encountered in the integer quantum Hall effect [2], the field of topological physics rapidly burgeoned after it was recognized that topologically-protected transport can also be observed even in the absence of a magnetic field [25,86]. This in turn, incited a flurry of experimental activities in a number of electronic material systems [87]. The promise of robust transport inspired studies in many and diverse fields beyond solid-state physics, such as optics, ultracold atomic gases, mechanics and acoustics, to mention a few [10,13–15,27–30,36,88–94]. Along these lines, unidirectional topological states were observed in microwave settings [16] in the presence of a magnetic field (the electromagnetic analogue of the quantum Hall effect), while more recently topologically-protected transport phenomena have been successfully demonstrated in optical passive all-dielectric environments by introducing artificial gauge fields [14,62].

In photonics, topological concepts could lead to new families of optical structures and devices by exploiting robust, scatter-free light propagation. Lasers in particular, could directly benefit from such attributes [63,95]. In general, laser cavities are prone to disorder, inevitably arising from fabrication imperfections, operational degradation and malfunction. More specifically, the

presence of disorder in a laser gives rise to spatial light localization within the cavity, ultimately resulting in a degraded overlap of the lasing mode with the gain profile. This in turn implies lower output coupling, multimode lasing, and reduced slope efficiency. These issues become further acute in arrays of coupled laser resonators where a large number of elements is involved. Naturally, of interest would be to employ topological features in designing laser systems that are immune to disorder. In this spirit, recently, edge-mode lasing in topological 1D Su-Schrieffer-Heeger resonator arrays has been studied by several groups [64,96,97]. However, being one-dimensional they lase in a zero-dimensional defect state, which inherently cannot provide protected transport. On the other hand, two-dimensional (2D) laser systems can directly benefit from topological protection. Indeed, it was theoretically shown that it is possible to harness the underlying features of topological insulators in 2D laser arrays - when lasing in an extended topological state [95,98]. As indicated in [95,98], such systems can operate in a single mode fashion with high slope efficiencies in spite of appreciable disorder. In a following development, unidirectional edge-mode lasing was demonstrated in a topological photonic crystal configuration involving a YIG substrate under the action of a magnetic field [99]. In that system, lasing occurred within a narrow spectral bandgap induced by magneto-optic effects. Clearly, of interest would be to pursue magnet-free approaches that are by nature more compatible with fabrication procedures and photonic integration involving low-loss components. In addition, such all-dielectric systems can prove advantageous in terms of substantially expanding the topological bandgap that dictates the degree of protected photon transport.

In this chapter, we report our experimental and theoretical results regarding lasing action in the edge modes of a topological photonic lattice of ring resonators in both 1D and 2D [63,64].

3.2. Lasing in the topological defect of a 1D SSH array

An archetypical example of one-dimensional discrete lattices that is known to be topologically non-trivial (thus allowing edge modes), is that described by the Su-Schrieffer-Heeger (SSH) model [37]. Thus far, this class of SSH structures have been employed to experimentally probe topological phase transitions [100,101] and to demonstrate *PT*-symmetric topologically protected bound states in fused silica coupled waveguide arrays [102]. Yet, in spite of the intense activity in this area, a comprehensive description as to how such topological structures behave under highly non-Hermitian conditions is at this point lacking, and several fundamental questions still remain unanswered. For example, can non-Hermiticity and/or nonlinearity impede or assist topological edge states? In that case, how do topological attributes depend on the gain/loss levels?

In this section, we address the above questions by theoretically and experimentally investigating these topological aspects in one-dimensional SSH laser arrays- structures that are both nonlinear and highly non-Hermitian. As it will be shown, the conventional *C*-symmetry associated with a passive SSH system no longer persists in the presence of non-Hermiticity. Instead, by judiciously engineering the gain and loss profile in the SSH laser array in a way that respects *PT*-symmetry, the ensuing Hamiltonian now possesses *CT*-symmetry, a necessary ingredient in this case for robust topologically protected lasing edge states. Here the complex Berry phase is used to predict the behavior of the active SSH structure for different levels of non-Hermiticity. Based on this analysis, three different phases are identified that depend on the gain levels involved and the coupling strengths. In this respect, one can observe a broad range of behaviors, starting from single edge-mode lasing and eventually ending into multimode emission within the bulk of the array. In all cases, the observed intensity mode profiles and spectra emitted

by this topological laser arrangement are in good agreement with theoretical models that account for carrier dynamics, saturable gain, and laser mode competition. In fact, these latter processes, play a crucial role in stabilizing the lasing edge-modes in such topological arrangements.

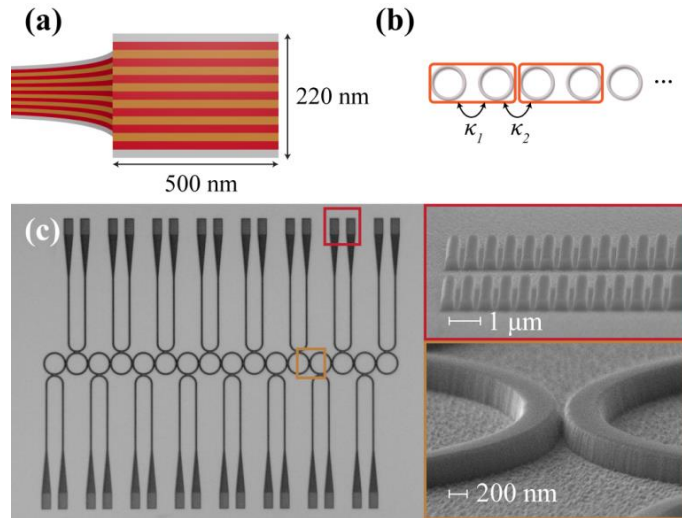


Figure 20 (a) InGaAsP multilayer quantum well structure used in the microrings, (b) a schematic of the SSH microring laser array, and (c) a microscope image of the fabricated structure with 16 elements. Insets show scanning electron microscope images of the grating at the end of the out-coupling waveguides, and the coupling region between two microrings.

In our study, the active SSH array consists of 16 identical coupled microring resonators fabricated on InGaAsP quantum wells. The gain-medium consists of six vertically stacked quantum wells, each composed of a 10 nm thick well ($In_{x=0.56}Ga_{1-x}As_{y=0.93}P_{1-y}$) sandwiched between two 20 nm thick barrier layers ($In_{x=0.74}Ga_{1-x}As_{y=0.57}P_{1-y}$), with an overall height of 200 nm, which is capped with a 10 nm thick layer of InP, as depicted in Fig. 14 (a). The coupling strengths in this SSH structure alternate between $\kappa_1 \approx 8 \times 10^{10} s^{-1}$ and $\kappa_2 \approx 1.4 \times 10^{11} s^{-1}$, as obtained when the distance between successive rings is 200 nm and 150 nm, respectively. The resulting bipartite lattice shown in Fig. 20(b) involves a nontrivial termination, capable of

supporting edge modes. Figure 20 (c) shows a microscope image of a fabricated SSH structure (eight unit cells), with each ring being weakly coupled to a waveguide that happens to be equipped with two out-coupling gratings - necessary to interrogate the array. Within the tight-binding formalism, the unit cell dynamics in this SSH configuration can be described by the following Hamiltonian:

$$\begin{aligned}
H_0 = & \epsilon_A \sum_n \hat{c}_n^{A\dagger} \hat{c}_n^A + \epsilon_B \sum_n \hat{c}_n^{B\dagger} \hat{c}_n^B \\
& + \sum_n \left(\kappa_1 \left(\hat{c}_n^{B\dagger} \hat{c}_n^A + \hat{c}_n^{A\dagger} \hat{c}_n^B \right) + \kappa_2 \left(\hat{c}_{n-1}^{B\dagger} \hat{c}_n^A + \hat{c}_n^{A\dagger} \hat{c}_{n-1}^B \right) \right),
\end{aligned} \tag{3.1}$$

where $\hat{c}_n^{A\dagger}$ and $\hat{c}_n^{B\dagger}$ denote photon creation operators at site n in the sublattices A and B of this structure, while ϵ_A and ϵ_B represent the complex on-site eigenfrequencies (potentials) of the corresponding active rings. Again, κ_1 and κ_2 are the intra-cell and inter-cell coupling coefficients, respectively. The ratio between these two coupling values, here denoted as $\nu = \kappa_2/\kappa_1$, determines the dimerization of the SSH structure. In a momentum space representation, the Bloch mode Hamiltonian can be obtained via a Fourier transform, i.e.:

$$H_0(k) = \begin{pmatrix} \epsilon_A & \kappa_1 + \kappa_2 e^{-ik} \\ \kappa_1 + \kappa_2 e^{+ik} & \epsilon_B \end{pmatrix}. \tag{3.2}$$

If the array system is Hermitian and is composed of identical rings ($\epsilon_A = \epsilon_B = 0$), then the Hamiltonian of Eq. 3.2 anti-commutes with the chiral operator $\mathbf{C} = \sigma_z$. Hence in this case, the eigenvalues are symmetrically distributed around zero, with the two zero-energy edge states being located at the ends of the Brillouin zone $k = \pm\pi$ (Fig. 21 (a)). The field profiles associated with these two edge states are displayed in the insets of Fig. 15 (a). On the other hand, if the SSH

structure is active, then the on-site potentials are now purely imaginary, i.e. $\epsilon_A = -ig_A$ and $\epsilon_B = -ig_B$. In this latter case, it is easy to show that the structure no longer possesses \mathbf{C} -symmetry, i.e. $\mathbf{C}H_0\mathbf{C}^{-1} \neq -H_0$. In our experimental realization (Fig. 20 (b)), the parameters g_A and g_B are dictated by the linear gain coefficients associated with the two sublattices A and B , as induced by differential pumping. In general, the dynamics of such an active SSH lattice are described by the following set of rate equations [103]:

$$\begin{aligned}
\frac{dE_n^A}{dt} &= \frac{1}{2}[-\gamma + \sigma(N_n^A - 1)](1 - i\alpha_H)E_n^A + i\kappa_1 E_n^B + i\kappa_2 E_{n-1}^B \\
\frac{dE_n^B}{dt} &= \frac{1}{2}[-\gamma + \sigma(N_n^B - 1)](1 - i\alpha_H)E_n^B + i\kappa_1 E_n^A + i\kappa_2 E_{n+1}^A \\
\frac{dN_n^A}{dt} &= R_A - \frac{N_n^A}{\tau_r} - F(N_n^A - 1)|E_n^A|^2 \\
\frac{dN_n^B}{dt} &= R_B - \frac{N_n^B}{\tau_r} - F(N_n^B - 1)|E_n^B|^2.
\end{aligned} \tag{3.3}$$

Here, E_n^A and E_n^B denote the electric modal field amplitudes in sublattices A and B , γ is inversely proportional to the photon lifetime in each of these identical cavities, and N_n^A and N_n^B represent the carrier population densities normalized with respect to the transparency value N_0 . In addition, α_H is the linewidth enhancement factor, $\sigma = \Gamma v_g a N_0$ is proportional to the unsaturated loss in the absence of pumping, Γ is the confinement factor, a is the gain proportionality factor, and $v_g = c/n_g$ denotes the group velocity within the cavity. In these equations R_A and R_B are normalized (with respect to N_0) pump rates, while τ_r indicates the carrier recombination lifetime in the InGaAsP quantum wells. Finally, $F = (\Gamma v_g a \epsilon_0 n_e n_g)/2\hbar\omega$, where ϵ_0 is the vacuum permittivity,

n_e is the mode effective index, \hbar is the reduced Planck's constant, and ω is the angular frequency of the emitted light. The linear gain coefficients can be directly obtained from the above parameters via $g_{A,B} = \sigma/2[(R_{A,B} - 1/\tau_r)/(1/\tau_r + F|E|^2)]$.

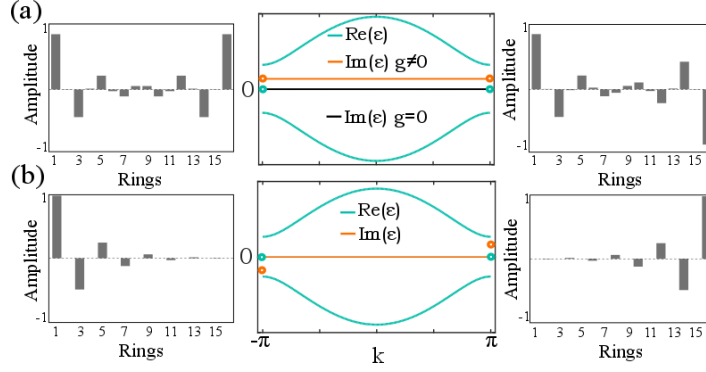


Figure 21 Eigenvalue diagrams of (a) Hermitian and uniformly pumped ($g = 0$ and $g \neq 0$) and (b) PT -symmetric SSH lattice. The field profiles of the edge states are also depicted in the right and left insets.

In order to address the aforementioned aspects, we first consider the simplest possible case, i.e. when the pumping is uniform $g_A = g_B = g$. The linear band structure of this SSH laser system under this condition is also depicted in Fig. 21 (a). The optical field distributions corresponding to the two edge states are identical to those in the Hermitian case. It is evident that in this scenario, the eigenvalues are no longer symmetrically distributed around the zero level, instead, they all rise by the same amount $-ig$ (in their imaginary part), corresponding to an equal amount of gain g for all supermodes involved. This situation drastically changes once PT -symmetry is introduced, i.e. $g_A = -g_B = g$. In this regime, the Hamiltonian of Eq. 3.2 now takes the form:

$$H_0(k) = \begin{pmatrix} -ig & \rho \\ \rho^* & ig \end{pmatrix}, \quad (3.4)$$

where $\rho = \kappa_1 + \kappa_2 e^{-ik}$. As previously indicated, this Hamiltonian does not respect C -symmetry.

Instead, H_0 satisfies:

$$\mathbf{C}T H_0 T^{-1} \mathbf{C}^{-1} = H_0, \quad (3.5)$$

where the time reversal operator T is here defined as $T = i\sigma_y K$, with K denoting complex conjugation. In this respect, if $|\psi\rangle$ is an eigenstate of H_0 ($H_0|\psi\rangle = \varepsilon|\psi\rangle$), then $\mathbf{C}T|\psi\rangle$ is also an eigenstate of H_0 , only this time its eigenvalue happens to be the complex conjugate ε^* . While PT-symmetry is imposed in real space, the CT operator acts in the momentum domain. Figure 21(b) shows the eigenvalues of this CT -symmetric Hamiltonian when $g < |\kappa_2 - \kappa_1|$. The inset in this figure displays the field amplitudes of the edge states corresponding to the two imaginary eigenvalues marked in the plot. Evidently, the field distributions of these states only occupy one of the sublattices (A or B), and alternate in sign. As a result, one of these modes is expected to experience gain, while the other one an equal amount of loss. Note that under PT-symmetric conditions, all the bulk modes remain neutral. It is also evident that the edge states in this SSH configuration, unlike bulk modes, exhibit spontaneous breaking of CT -symmetry, in other words, the left and right edge modes can be converted into one another through the CT operator.

Figure 22 (a) shows the steady-state intensity distribution as obtained from numerical simulations (Eqs. 3.3), for a 16-element SSH laser system when uniformly pumped at $R_{A,B} = 1.05/\tau_r$. In these simulations, we assume that $\alpha_H = 4$, $\tau_r = 4 \text{ ns}$, and $\sigma = 3 \times 10^{11} \text{ s}^{-1}$. It is clear that in this case the resulting lasing profile is a complex mixture of all the supermodes (including the edge states) supported in this laser array. This is because all modes experience the same gain. Nevertheless, the wavelength emission in the array greatly depends on the site number (insets of Fig. 22). Our theoretical analysis suggests that the edge state will always lase at the

resonance frequency ω_0 ($\Omega/\kappa_1 \approx 0$) with a relatively narrow linewidth. Conversely, the spectrum emanating from rings in the bulk (bulk modes) will have a considerably more complex structure because of mode competition effects. On the other hand, Fig. 22 (b) shows the expected intensity distribution under PT-symmetric conditions after numerically solving Eqs. 3.3 – starting from noise. In this case, only sublattice A is pumped at $R_A = 1.05/\tau_r$ while B is kept in the dark. In this regime, our simulations show that only one of the edge modes (the one enjoying gain) is favored and hence lases, while all the bulk modes are suppressed. In direct contrast to the results presented in Fig. 22 (a), CT-symmetry now promotes only the edge state. Consequently, the spectrum emitted at the edge happens to be close to the ring resonance ω_0 and is single-moded.

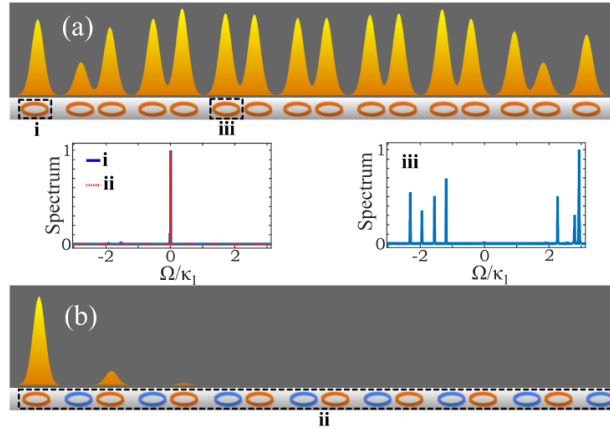


Figure 22 Theoretically predicted steady-state lasing profiles for a) uniformly pumped and b) PT-symmetric SSH lattice. The insets show the power spectra corresponding to the edge mode and bulk modes as obtained from different locations in the array.

The dynamics of this CT-symmetric SSH laser system can be theoretically predicted by considering the non-Hermitian Berry phase associated with the Hamiltonian of Eq. 3.4. In general,

the Berry phase ϕ corresponding to an eigenstate of a non-Hermitian Hamiltonian $H(\mathbf{q})$ is given by [104]:

$$\phi = \oint \langle \lambda(\mathbf{q}) | i \nabla_{\mathbf{q}} \psi(\mathbf{q}) \rangle \cdot d\mathbf{q}, \quad (3.6)$$

where the integral is evaluated on a closed path traced by \mathbf{q} in the parameter space on which $H(\mathbf{q})$ is defined, while $|\psi(\mathbf{q})\rangle$ and $|\lambda(\mathbf{q})\rangle$ are the right and left (biorthogonal) eigenstates of $H(\mathbf{q})$, respectively. From here, the complex Berry phase acquired from the upper (+) and lower (-) bands of the Hamiltonian can be obtained from the following integral [105]:

$$\phi_{\pm} = \frac{1}{2} \oint (1 \pm \cos \alpha) \frac{d\theta}{dk} dk, \quad (3.7)$$

where $\alpha = \tan^{-1} \left(\frac{|\rho|}{ig} \right)$, and $\theta = -\arg(\rho)$. The integration in Eq. 3.7 is performed over the Brillouin zone of the Hamiltonian, i.e. $k \in [-\pi, \pi]$. In the Hermitian limit of $g = 0$, this phase ϕ_h coincides with the conventional Zak phase [106]:

$$\phi_+ = \phi_- = \phi_h = \frac{1}{2} \int_{k=-\pi}^{\pi} d\theta = \begin{cases} \pi & \nu > 1 \\ 0 & \nu < 1 \end{cases} \quad (3.8)$$

Equation 3.8 clearly indicates that the dimerization ratio $\nu = \kappa_2/\kappa_1$ plays an important role in establishing a topological phase transition, a well-known result when dealing with Hermitian SSH arrays. On the other hand, in the presence of non-Hermiticity ($g \neq 0$), the cosine term in the integral of Eq. 3.7 will lead to a complex Berry phase. In what follows, we show how different phase transitions of this PT-symmetric laser SSH system can be predicted by examining this

complex phase. Under these conditions, the integral of Eq. 3.7 can be analytically obtained in closed form. In this case, the complex Berry phase is given by [105]:

$$\Phi_{\pm} = \Phi_h \pm \frac{i\eta}{2} \sqrt{\frac{y}{v}} \left(K(y) + \frac{v-1}{v+1} \Pi(x, y) \right). \quad (3.9)$$

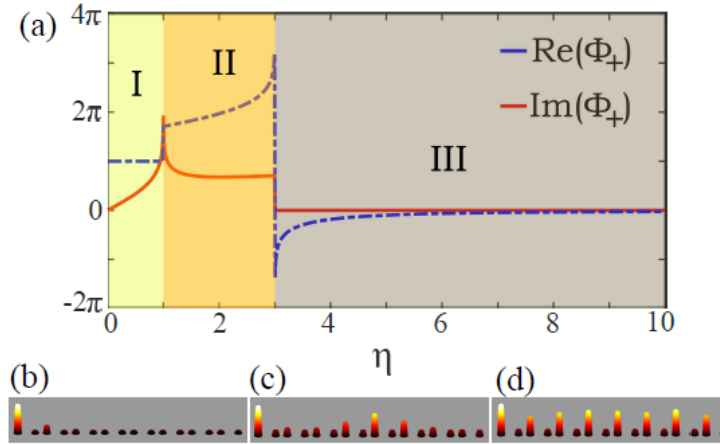


Figure 23 The complex Berry phase Φ_+ as a function of the normalized gain η . The different phases are indicated through different colors. The simulated intensity distributions corresponding to these three distinct phases I, II, and III are depicted in (b), (c), and (d), respectively.

In this expression the real quantities $x = \frac{4v}{(v+1)^2}$, $y = \frac{4v}{(v+1)^2 - \eta^2}$ depend on both the normalized gain $\eta = g/\kappa_1$ and the dimerization coefficient v , while K and Π denote complete elliptic integrals of the first and third kind, respectively. Figure 23 (a) shows the Berry phase associated with the upper band Φ_+ as a function of the normalized gain η when $v = 2$. A close inspection of this figure reveals three distinct phases, as predicted from Eq. 3.9. More specifically, if the SSH system is operated in the range of $0 < \eta < v - 1$ (denoted as phase I), only the edge state is expected to lase. In this domain, under steady-state conditions (Eqs. 3.3) the structure is single-moded and the

intensity profile across the array varies exponentially with the site number (Fig. 23 (b)). As the gain in the system increases, i.e. for $\nu - 1 < \eta < \nu + 1$ in Fig. 23 (a), the SSH structure enters phase II, where some of the bulk modes of the structure start to acquire complex eigenvalues (after entering the *PT*-symmetry broken phase), resulting in a multimode operation (Fig. 17 (c)). Note that in phase II the intensity profile across the array is asymmetrically one-sided, biased towards the edge mode. Finally, for even higher values of gain/loss contrast, i.e. $\eta > \nu + 1$, the system crosses another threshold and moves into phase III, as also corroborated by analyzing Eqs. 3.3. At this point, all of the bulk modes of the active lattice break their *PT*-symmetry, and as such, they start to lase - all competing for the gain. Unlike what happens in the first two phases, after crossing into phase III, the edge state is now obscured by bulk modes. This in turn results into a more uniform intensity profile, as shown in Fig. 23 (d). In other words, in this range, the pumped sublattice is uniformly lasing, while its lossy counterpart remains dark. The theoretically expected spectra corresponding to these three phases can be found in section 3.2.1. We would like to note that the phase transition points coincide with the three distinct morphing stages of the complex band structure of this non-Hermitian *PT*-symmetric SSH lattice (section 3.2.1).

To verify these predictions, we have conducted a series of experiments with a 16 ring SSH array, each having a radius of $5 \mu m$. To enforce single-transverse mode operation at $1.59 \mu m$, the width of the resonators was set to $500 nm$. In order to reduce the lasing threshold, the microrings were surrounded by a low-index dielectric, entailing a higher confinement. As previously indicated, each ring was individually interrogated (intensity-wise and spectrally) through an extraction bus waveguide, featuring a pair of grating out-couplers (Fig. 20 (c)). To introduce *PT*-symmetry, the microresonators were alternately pumped at $1.06 \mu m$ by using a titanium amplitude

mask. Figure 24 shows the extracted intensity profile from every ring, the corresponding raw data as imaged onto an infrared InGaAs camera as well as the spectra associated with the three phases previously mentioned. In particular, (a), (b), and (c) present the data corresponding to phase I, II, and III.

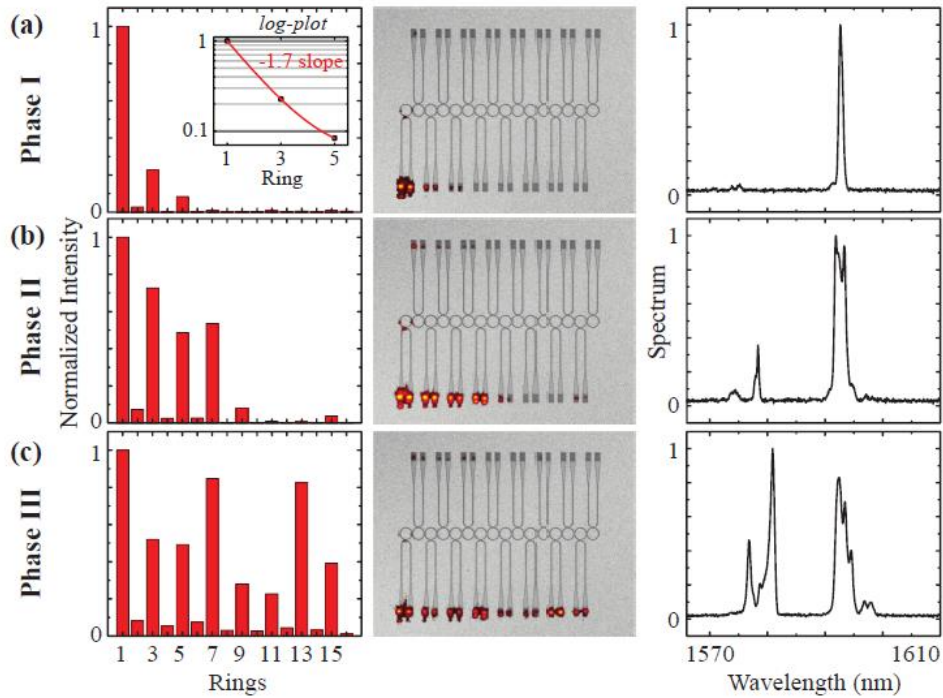


Figure 24 The left panels depict the measured intensity distributions in the 16-element SSH array at every site. The middle panels show raw data from the extraction ports, while the right panels the corresponding power spectra. Each of the successive rows (a), (b), and (c) are progressively associated with phase I, II, and III observations. The inset in (a) provides the exponential intensity distribution of the lasing edge-state in a log-linear scale.

At a pump intensity of $I = 26 \text{ kW/cm}^2$ the edge mode is the only one to lase (Fig. 24 (a)). Once the first phase transition occurs, other modes start competing for the gain (Fig. 24 (b) at $I = 41 \text{ kW/cm}^2$) and eventually the edge mode is obscured (Fig. 24 (c) at $I = 83 \text{ kW/cm}^2$). The emergence of these

three phases is also evident in their spectra. While the spectrum of the edge mode is single-moded, once the first phase transition occurs, bulk modes also appear, with upshifted frequencies as expected from theory (section 2.1.2). Interestingly, Fig. 18 (a) reveals that the exponential intensity decay of the edge mode (log-linear inset) is in good agreement with that expected from theory ($\sim \left(\frac{\kappa_1}{\kappa_2}\right)^{2n}$) when $\nu = 1.7$. Finally, in all our experiments we found that gain saturation plays a prominent role in stabilizing the lasing edge mode at different pumping levels.

3.2.1 Theoretically predicted spectra emitted by the PT-symmetric SSH laser array

The simulated spectra expected for the three different phases of the PT-symmetric SSH laser array corresponding to Fig. (23) of the main text are presented in Fig. 25. As evident in this figure, phase I involves single edge-mode operation, which lases close to the central frequency ω_0 (Fig. 25 (a)). In phase II, bulk modes of the system will enter the PT-symmetry broken phase, resulting in extra emission lines in the spectra (Fig. 25 (b)). Finally, in phase III all the supermodes (including the edge modes) acquire nonzero gain and loss. This leads to a more involved emission spectra corresponding to those supermodes associated with gain, as shown in Fig. 20 (c). The qualitative behavior of the system as summarized here is consistent with the experimental results of the right panels in Fig. (26).

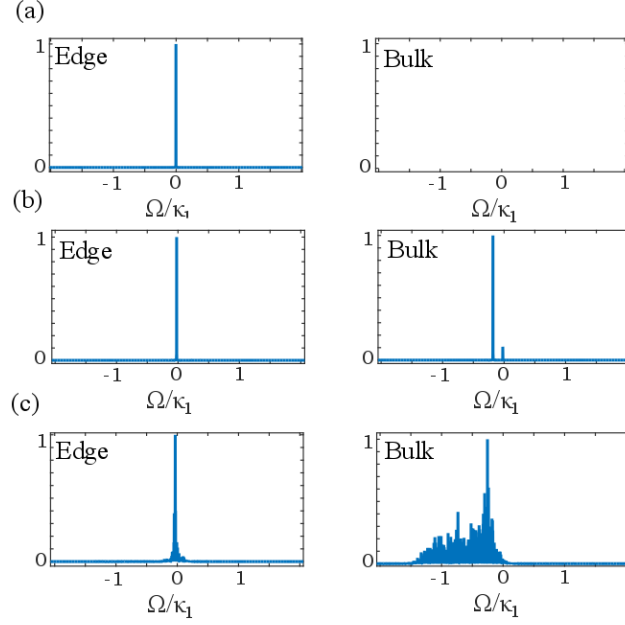


Figure 25 Calculated spectra for the system considered in Fig. 17 in (a) phase I, (b) phase II, and (c) phase III.

3.2.2 Complex band structure of the CT-symmetric Hamiltonian

Consider the Hamiltonian:

$$H_0(k) = \begin{pmatrix} -ig & \kappa_1 + \kappa_2 e^{-ik} \\ \kappa_1 + \kappa_2 e^{ik} & ig \end{pmatrix}, \quad (3.10)$$

with the eigenvalues:

$$\varepsilon(k) = \pm \kappa_1 \sqrt{1 + \nu^2 + 2\nu \cos(k) - \eta^2}. \quad (3.11)$$

The eigenvalue diagrams corresponding to Eq. 3.11 for three different regimes of $\eta < \nu - 1$, $\nu - 1 < \eta < \nu + 1$, and $\nu + 1 < \eta$ are shown in Fig. 20, where $\nu = 2$. It can be observed that in the first regime (phase I), only the edge states of the SSH structure cross the PT-symmetry threshold (the threshold for these modes is at $g = 0$), while all the bulk modes are in the PT-symmetry unbroken phase. This is shown in Fig. 20 (a) for $\eta = 0.9$, where the eigenvalues of the bulk modes

of H_0 are all real. As the gain parameter is increased such that the structure enters phase II, part of the spectrum becomes complex for some values of the Bloch momentum k . This morphing of the spectrum is depicted in Fig. 26 (b) when the normalized gain is $\eta = 1.5$. Finally, as the gain is increased even further, the system will operate in phase III and the Hamiltonian of Eq. 3.10 exhibits an entirely imaginary spectrum for all values of k . Consequently, all the modes of this active SSH lattice (including edge modes as well as bulk modes) now experience nonzero gain and loss, so that half of the modes enjoy the gain provided by the system. As a result, there will be a gain competition among these modes which in turn results into a more complex emitted spectrum by this SSH array. Figure 26 (c) illustrates this effect for $\eta = 3.1$.

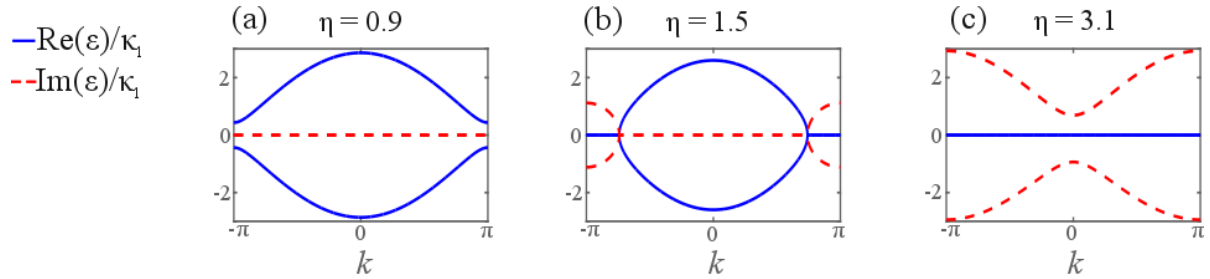


Figure 26 Eigenvalue diagrams associated with the CT-symmetric Hamiltonian of Eq. (2-10) for three different normalized gain values indicated at the top. The three diagrams correspond to (a) phase I, (b) phase II, and (c) phase III.

3.2.3 Frequency upshift in the spectra

In this section we present the theoretical analysis which explains the upshift in the frequency spectrum in the PT-symmetric SSH laser array, due to a positive linewidth enhancement factor. In this respect, we consider the modified version of the Hamiltonian of Eq. 3.4:

$$H_1(k) = \begin{pmatrix} -ig(1 - i\alpha_H) & \rho \\ \rho^* & ig(1 - i\alpha_H) \end{pmatrix}, \quad (3.12)$$

where again $\rho = \kappa_1 + \kappa_2 e^{-ik}$, and α_H represents the linewidth enhancement factor. The eigenvalues of this new Hamiltonian can be obtained as:

$$\varepsilon'_{\pm} = \pm \sqrt{|\rho|^2 - g^2(1 - i\alpha_H)^2}. \quad (3.13)$$

For relatively high values of gain which satisfy $|g\alpha_H| \gg |\rho|$, the result of Eq. (2-13) can be simplified as:

$$\varepsilon'_{\pm} \approx \pm ig(1 - i\alpha_H). \quad (3.14)$$

Now the supermodes which experience gain are the ones associated with $\varepsilon'_- \approx -ig - g\alpha_H$, where the negative real part signals an upshift in the resonance frequency for $g, \alpha_H > 0$, due to the chosen base $e^{-i\omega t}$. In other words, in a PT-symmetric active SSH array, the emission spectra of the lasing bulk modes (when the system is operated in phases II and III) will be upshifted with respect to the central frequency ω_0 of the individual rings.

3.2.4 Analytical solution for the edge state in the SSH array

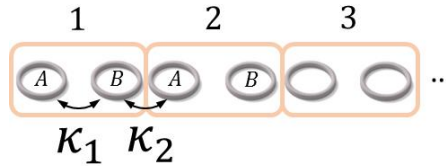


Figure 27 A schematic of a semi-infinite PT-symmetric SSH microring laser array.

Consider the semi-infinite PT-symmetric SSH array depicted schematically in Fig. 27. The coupled mode equations involving the modal field amplitudes inside the rings are given by:

$$\frac{dE_n^A}{dt} = gE_n^A + i\kappa_1 E_n^B + i\kappa_2 E_{n-1}^B \quad (3.15)$$

$$\frac{dE_n^B}{dt} = -gE_n^B + i\kappa_1 E_n^A + i\kappa_2 E_{n+1}^A,$$

with the boundary condition:

$$\frac{dE_1^A}{dt} = gE_1^A + i\kappa_1 E_1^B. \quad (3.16)$$

We seek solutions of the form $E_n^A = Ae^{iQn}e^{-Pn}e^{\xi t}$ and $E_n^B = Be^{iQn}e^{-Pn}e^{\xi t}$. By direct substitution of these solutions in Eqs. (2-15, 2-16), one obtains the following solution for the edge state:

$$\begin{aligned} \xi &= g \\ B &= 0 \\ Q &= \pm\pi \\ e^{-P} &= \frac{\kappa_1}{\kappa_2}. \end{aligned} \quad (3.17)$$

Therefore, the solution for the edge mode in this semi-infinite PT-symmetric SSH array is given by:

$$\begin{aligned} E_n^A &= A \left(-\frac{\kappa_1}{\kappa_2} \right)^n \\ E_n^B &= 0. \end{aligned} \quad (3.18)$$

3.3. 2D Topological laser

In this section, we report our observation of topologically-protected edge-mode lasing in nonmagnetic, two-dimensional topological cavity arrays. These systems can operate in single mode, even considerably above threshold, with a slope efficiency that is considerably higher than that achieved in their corresponding trivial realizations. Moreover, we show experimentally that

the topological protection is still manifested, thus leading to high efficiencies, even in the presence of defects. Finally, we assemble a topological system based on S-chiral resonator elements, which – in addition to the topological properties – also displays unidirectional transport of light in the cavity.

To demonstrate topological lasing, we fabricate a 10×10 coupled ring-resonator array on an active platform involving vertically stacked 30 nm thick InGaAsP quantum wells (see section 3.3.2), as shown in Fig. 28 (A). The array is interrogated at specific sites using out-coupling gratings (Fig. 28 (B), corresponding to the yellow framed regions in Fig. 28 (A)). The active lattice investigated here employs a topological architecture that is similar to that suggested in Refs. [13,95]. This 2D setting is comprised of a square lattice of ring resonators which are coupled to each other via link rings (Fig. 28, A and C). The link rings are designed so as to be antiresonant to the main ring resonators. In this all-dielectric design, the intermediary links are judiciously spatially-shifted along the y-axis, with respect to the ring resonators, to introduce an asymmetric set of hopping phases. The phase shift is sequentially increased along the y-axis in integer multiples of $\pm 2\pi\alpha$, where in our case $\alpha = 0.25$. In this way, a round trip along any plaquette (consisting of 4 rings and 4 links) results in a total accumulated phase of $\pm 2\pi\alpha$, where the sign depends on the direction of the path along this unit cell. This provides the lattice with a synthetic magnetic field and establishes two topologically non-trivial bandgaps, as shown in Fig. 28 (D). The cross-section of each ring (500 nm width and 210 nm height) is designed to ensure single transverse mode conditions at the wavelength of operation 1,550 nm (see section 3.3.2). The nominal separation between the ring-resonators and off-resonant links is 150 nm, thus leading to two frequency bandgaps, each having a width of 80 GHz (0.64 nm). The spectral size of the two bandgaps was

obtained by experimentally measuring the frequency splitting (0.8 nm) in a binary system of primary resonators, linked via an intermediate racetrack ring. In order to promote protected edge-mode lasing, we optically pump only the outer perimeter of this array at 1064 nm with 10 ns pulses (Fig. 28E). This is achieved using a set of appropriate amplitude masks (see section 3.3.1). The intensity structure of the lasing modes is captured using an InGaAs infrared camera, and their spectral content is then analyzed using a spectrometer with an array detector. In what follows we compare the features of the topological insulator lasers ($\alpha = 0.25$) with those of their trivial counterparts ($\alpha = 0$) under various conditions.

As shown in [95], edge mode lasing can be incited by pumping the boundary of the topological array. In this case, a clear signature of topological lasing would be a highly efficient single-mode emission even at gain values high above the threshold. To experimentally observe these features, we pump the perimeter of the topological and trivial arrays, and measure the lasing output power (integrated over the two out-coupling gratings) and its spectral content. The measured light-light curves for the topological and the trivial arrays are shown in Fig. 29A, clearly indicating that the topological system lases with a higher efficiency than its trivial counterpart. Their measured spectra are shown in Fig. 29 (B-D). We observe that the topological arrays remain single-moded over a wide range of pumping densities (Fig. 29C), whereas the trivial arrays (tested over multiple samples) always emit in multiple wavelengths with considerably broader linewidths (Fig. 29D).

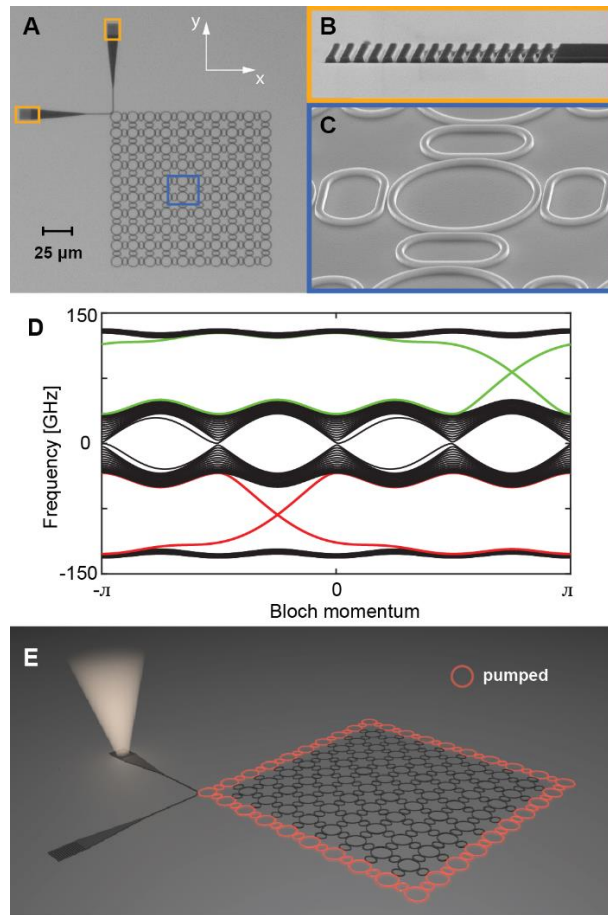


Figure 28 Topological insulator laser: lattice geometry and associated band structure. (A) Microscope image of an active InGaAsP topologically non-trivial 10×10 micro-resonator array. (B) SEM image of the out-coupling grating structures used to probe the array at the location indicated in (A). (C) SEM micrograph of a unit cell comprised of a primary ring site surrounded by four identical intermediary racetrack links. (D) Frequency band diagram corresponding to an infinite ribbon structure based on the topological lattice used in this study. The bulk bands are colored in black, while the two counter-propagating edge-state bands in green and red. (E) A schematic of the topological array when pumped along the perimeter so as to promote edge mode transport. The directionality of energy flow is monitored through the power extracted from the out-coupling gratings.

Importantly, if we only compare the power emitted in the dominant (longitudinal) mode, the topological array outperforms the trivial one by more than an order of magnitude. This difference

in performance is attributed to the physical properties of the topological edge-modes. The trivial array suffers from several drawbacks. First, the trivial lasing modes extend into the lossy bulk, thus experiencing suppressed emission. Second, the trivial lasing modes try to avoid the output coupler so as to optimize their gain. And finally, due to intrinsic disorder in fabrication, the lasing mode localizes in several different parts of the trivial lattice, each lasing at a different frequency, thereby giving rise to a multimode behavior. Conversely, apart from a weak exponential penetration, in topological arrays the edge-states are completely decoupled from the bulk. Moreover, since they only flow around the perimeter, they are always in contact with the output coupler. Finally, because of its inherent topological properties, the lasing edge mode does not suffer from localization, and therefore it uniformly extends around the perimeter (in single mode), using all the available gain in the system by suppressing any other parasitic mode.

In order to demonstrate that these active lattices exhibit topological features, we compare their lasing response against that of their trivial counterparts ($\alpha = 0$) when their periphery is pumped. The emission intensity profiles obtained from these two systems are shown in Figs. 30 (A, B). To check whether the lasing modes are extended or localized around the perimeter of the lattice, we measure the spectrum of the light emitted from different sites around the arrays (Figs. 30 (C, D)). For the trivial array, we observe that the spectrum varies around the lattice, with emission occurring over a wide wavelength range spanning from 1543nm to 1570nm, as shown in Fig. 30 (C). This is an indication that the trivial array lases in localized domains, each one at a different frequency. In sharp contrast, in the topological array, all sites emit coherently at the same wavelength (Fig. 30 (D)). This lasing, in a single extended topological edge mode is a direct manifestation of a topologically-protected transport, akin to that taking place in topological

insulators. These results are consistent with those presented in Fig. 29. Topological transport in these structures is further investigated by selectively pumping the lattice. First, we pump only one edge of the 2D array, as depicted in Fig. 30 (E). Under these conditions, the lasing mode in the trivial system is confined to the pumped region (Fig. 30 (E)). In this arrangement, the emission is heavily suppressed both in the bulk as well as along the perimeter and consequently no light is extracted from any of the output grating couplers. In contrast, for the topological array, even though only one side is pumped, the edge mode flows along the periphery - finally reaching the output coupler, as shown in Fig. 30 (F). In this case, only one output coupler grating emits strongly. This indicates that the lasing mode that reaches the output coupler has a definite chirality in each ring. Given that the emission is in a single mode, one can conclude that lasing takes place in only one topological mode. To show that indeed the bulk states are mostly suppressed in the trivial arrangement, we then expand the pumping region at the bottom edge (Fig. 30 (G)). In the trivial case, even though pumping over a larger area is now provided, still no laser light reaches the output ports. On the other hand, for the topological array, the lasing edge mode reaches the output coupler with a fixed chirality within each ring (Fig. 30 (H)). This shows that the topological lasing mode extends around the perimeter, whereas the lasing in the trivial case occurs in stationary localized modes. In this vein, we tested multiple samples, and found that these same features consistently emerged in a number of different designs (different resonance frequencies, couplings, etc.) in a universal manner.

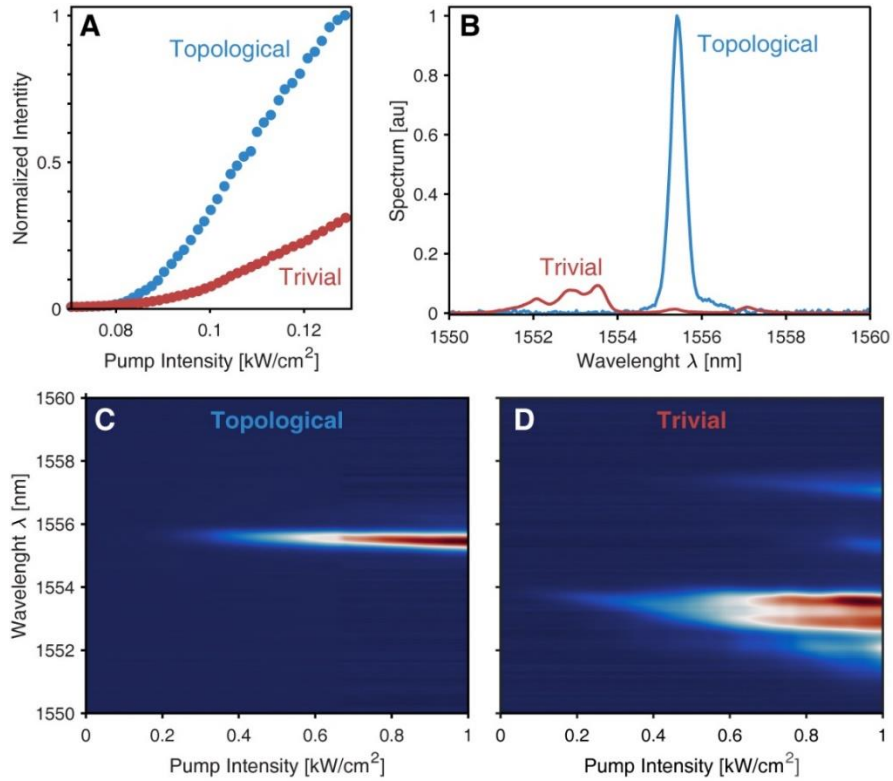


Figure 29 Slope efficiencies and associated spectra of topological and trivial lattices. (A) Output intensity vs. pump density for a 10x10 topological array with $\alpha = 0.25$ and its corresponding trivial counterpart ($\alpha = 0$). In this experiment the enhancement of the slope efficiency ratio is approximately 3x. (B) Emission spectra from a trivial and a topological array when pumped at 23.5 kW/cm². Evolution of the spectrum as a function of the pumping levels for (C) topological and (D) trivial arrays. Single-mode, narrow-linewidth lasing in (C) is clearly evident.

Next, we study lasing in a topological structure and in its trivial counterpart, in the presence of defects, which are intentionally introduced into the structures. To do so, we removed specific microrings along the perimeter, where pumping is provided. Figure 31 shows the light emission from these two types of structures. These results demonstrate that in a topological system (Fig. 31 (A)), light is capable of bypassing the defects by penetrating into the lossy bulk and displaying lasing in an extended edge mode of almost uniform intensity. Conversely, in the trivial structure

(Fig. 31 (B)), the intensity of the emitted light is considerably subdued, and the defects are subdividing the perimeter into separate regions which lase independently. Hence, the topological insulator laser is robust against defects, even when introduced into the gain regions.

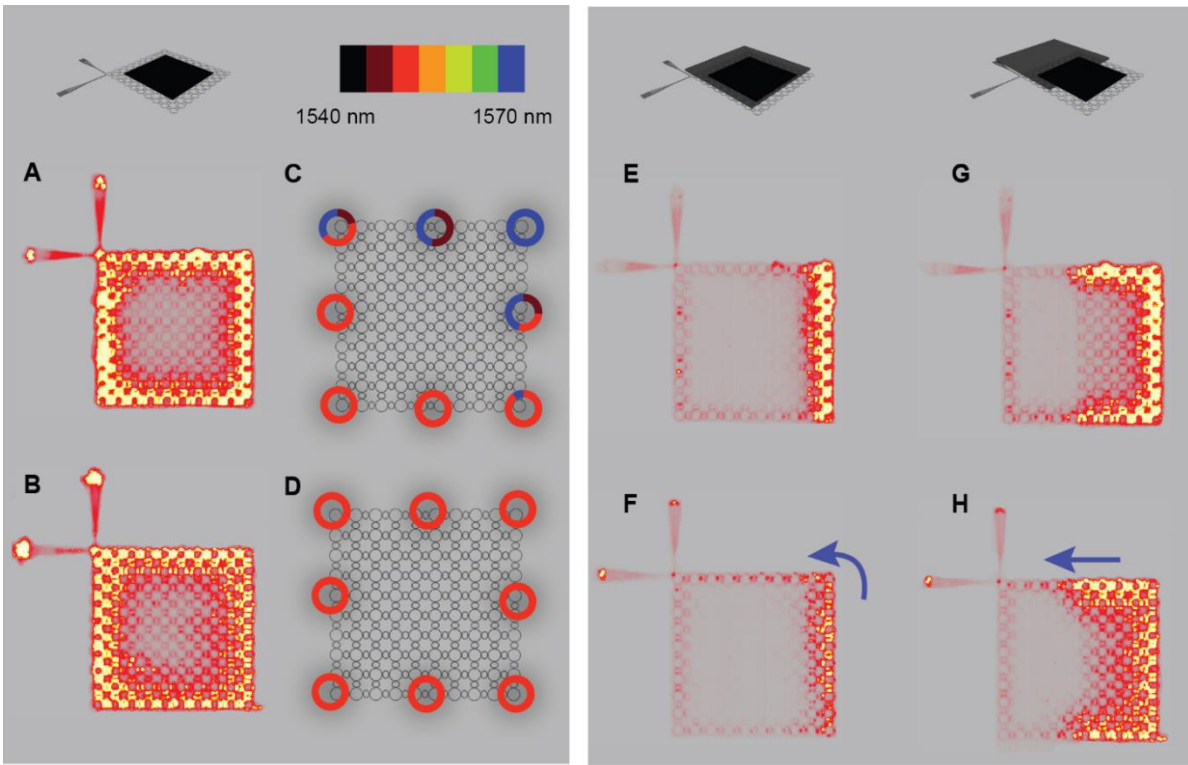


Figure 30 Lasing characteristics of topological lattices vs. that of their corresponding trivial counterparts under different pumping conditions. Lasing in a (A) non-topological and (B) topological array when only their periphery is selectively pumped. (C) and (D) represent the spectral content as obtained from specific edge-sites of the arrays as depicted in (A) and (B), correspondingly. Notice that the topological lattice remain single-moded while the trivial one emits in several modes. Lasing transport in a (E) trivial array and in a (F) topological lattice when the bottom side is pumped. The excitation of the edge-mode in (F) is clearly visible. (G) and (H) present similar results when the pumping region at the bottom side is further extended. In (H) the edge-mode is again excited. No laser radiation is observed from the extracting ports in the trivial lattice (G). The pumping conditions are shown in the insets at the top.

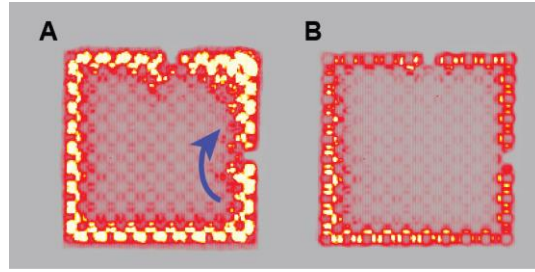


Figure 31 Robust behavior of the lasing edge mode with respect to defects in a topological array. Lasing response of a (A) topological and (B) trivial array in the presence of two defects intentionally inserted on the periphery. Note that the edge mode transport in (A) clearly bypasses the defects, whereas no such behavior is observed in its trivial counterpart.

At this point, it is important to recall that in the absence of a magnetic field, all passive photonic topological insulators demonstrated thus far are by nature reciprocal. This raises an interesting question: is it possible to enforce unidirectionality in an all-dielectric lasing topological array? To address this aspect, we break the symmetry between the clockwise (CW) and counter-clockwise (CCW) topological edge modes. To do so, we modify the individual resonators: instead of using conventional rings we employ a special S-bend design [107], for each primary cavity element in the topological lattice (Fig. 32 A and B). The intermediary links remain the same as in the previous designs (Fig. 28A). In this system, each laser micro-resonator operates in a single spin-like manner, i.e. in either the CW or the CCW direction by exploiting gain saturation and energy recirculation among these modes. To some extent, this imposed unidirectionality is analogous to the spin-orbit coupling process enabling one-way topological conduction in magnet-free electronic topological insulators. The S-chiral elements involved, allow one to add unidirectionality to the topological protection of transport. In other words, edge mode lasing takes place in a topologically protected, scatter-free, unidirectional fashion even in the absence of a magnetic field. In our experiments, we

observe a 9 dB suppression between the right- and left-hand spins in each resonator. Finite difference time domain simulations (see section 3.3.6) also indicate that the differential photon lifetime between the right/left spins in these S-bend cavities is approximately 3 ps, corresponding to an equivalent loss coefficient of 10 cm^{-1} . The field distribution in the prevalent spinning mode in these active S-resonators is shown in Fig. 32 (C), featuring a high degree of power-recirculation through the S-structure that is responsible for the spin-like mode discrimination. The corresponding intensity distribution associated with this unidirectional edge-mode energy transport is shown in Fig. 32 (D). As expected in this case, energy is pre-dominantly extracted from only one of the two out-coupling gratings (with a 9 dB rejection ratio) – a direct indication of unidirectional energy flow in this topological array.

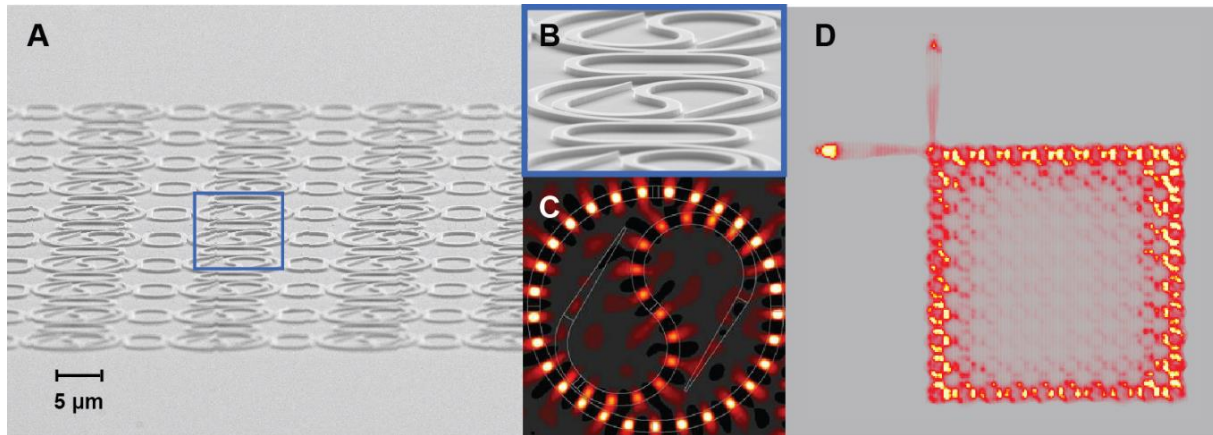


Figure 32 Topological active array involving chiral S-micro-resonator elements. (A) SEM image of a 10x10 topological array. The primary resonators feature an internal S-bend for enforcing in this case a right-spin, while the intermediate link design is the same as in Fig. 1 (C). (B) A closeup SEM micrograph of the basic elements involved. (C) Field distribution in an individual S-element as obtained from FDTD-simulations. (D) Measured intensity profile associated with the lasing edge-mode in a topological array with $\alpha = 0.25$. In this system, the periphery is selectively pumped, and the energy flows unidirectionally in a clock-wise manner, as also indicated by the radiation emerging from the extracting ports.

3.3.1 Characterization setup

In order to pump, and spatially/spectrally resolve the output of the micro-resonator arrays a measurement setup as depicted in Fig. 33 (A) was employed. The micro-resonator arrangements were optically pumped with a pulsed 1064 nm laser beam (SPI fiber laser). The diameter of the beam was arranged such that at the surface of the sample it had a diameter of $\sim 300 \mu\text{m}$. A microscope objective with a numerical aperture of 0.42 was used to project the pump beam on the rings, as well as to collect the output light from the samples. Alignment of the pump beam to the samples was performed by imaging the sample surface through two cascaded 4-f imaging systems onto an IR camera (Xenics Inc.), using a broadband IR light source. Output spectra were obtained using a spectrometer (Horiba Scientific iHR320) equipped with a 900 g/mm grating in conjunction

with an electrically cooled InGaAs detector (Synapse EM). The spectrometer entrance slit was set to 100 μm in order to obtain a resolution of ~ 0.13 nm. The micro-resonator array was pumped by imaging a titanium mask onto the surface of the sample leaving only the perimeter to be pumped. Additionally, both out-coupling waveguides were obscured with a knife-edge as indicated in Fig. 33 (B).

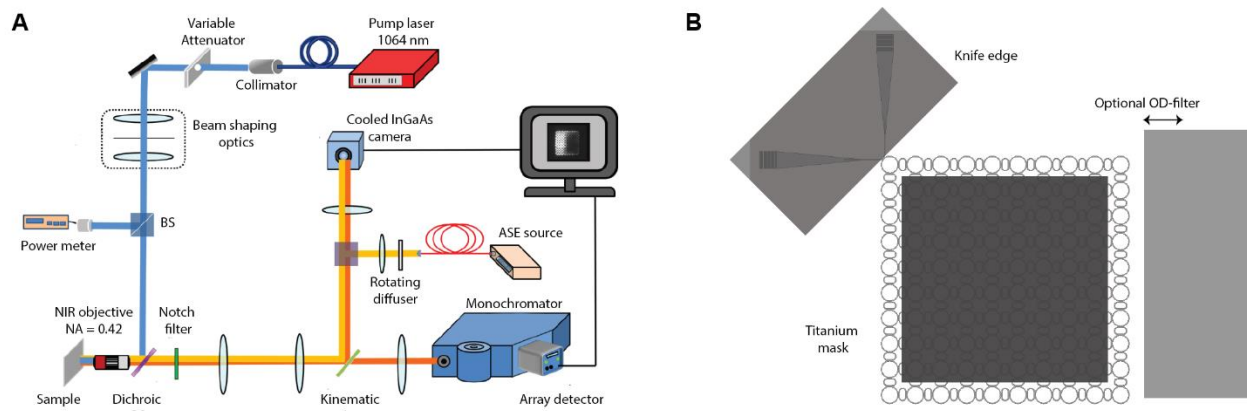


Figure 33 (A) Sketch of the measurement setup: sample on the lower left, pump laser on top and analysis setup on the right. (B) Pumping scheme and masks employed for the interrogation of the micro-resonator arrays.

3.3.2 Fabrication procedures

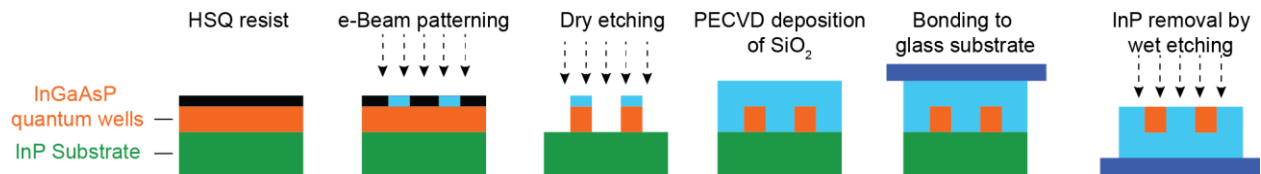


Figure 34 Manufacturing steps of the micro-ring resonators.

This section discusses the steps (Fig. 33) followed to fabricate the investigated micro-resonator arrays. The multiple quantum well gain system is comprised of six $\text{In}_{x=0.74}\text{Ga}_{1-x}\text{As}_{y=0.57}\text{P}_{1-y}$ wells (thickness: 10 nm each) and is sandwiched between two cladding layers of $\text{In}_{x=0.56}\text{Ga}_{1-x}\text{As}_{y=0.93}\text{P}_{1-y}$ (thickness: 20 nm), all grown on a p-type InP substrate. The quantum wells are covered by a 10 nm thick InP protective layer. The MOCVD epitaxially-grown wafer was supplied by OEpic Inc. To fabricate the microring resonators, a hydrogen silsesquioxane (HSQ) solution in methyl isobutyl ketone (MIBK) was first spin-coated on the wafer as a negative tone inorganic electron beam resist and patterned using electron beam lithography. The structures were developed with tetramethylammonium hydroxide (TMAH) and subsequently transferred to the wafer through a reactive ion etching process. The dry etching used the gases $\text{H}_2:\text{CH}_4:\text{Ar}$ with flows of 40:4:20 SCCM, RIE/ICP power of 150 W, and a chamber pressure of 30 mT. Scanning electron micrograph (SEM) images of samples at the end of this step are shown in Fig. 28 (B, C). To remove the remaining resist the structures were immersed into BOE for 10s. Next, a 3 μm silicon dioxide (SiO_2) film was deposited on the structure using plasma enhanced chemical vapor deposition (PECVD). SiO_2 increases the confinement factor of the propagating modes and additionally gives mechanical support to the micro-resonators once the InP substrate is removed. Subsequently, the SiO_2 film was covered with SU8 photoresist and attached to a glass slide. Finally, the InP substrate was removed by wet etching in hydrochloric acid (HCl). This wet etching process is highly selective and abruptly stops after removing InP substrate, leaving the InGaAsP quantum wells intact. After this process, the micro-rings are partially embedded in the SiO_2 matrix and partially exposed to air.

3.3.3 Spectra from extended edge states

The spectra used to extract the spectral content from eight different positions along the perimeter to create Fig. 29 (G, H) in the previous sections are displayed in Fig.35. While the perimeter of the (A) trivial array exhibits a position dependent spectral content, the one of the (B) topological lattice features only one mode along the whole array. This is because of the extended nature of the edge-state.

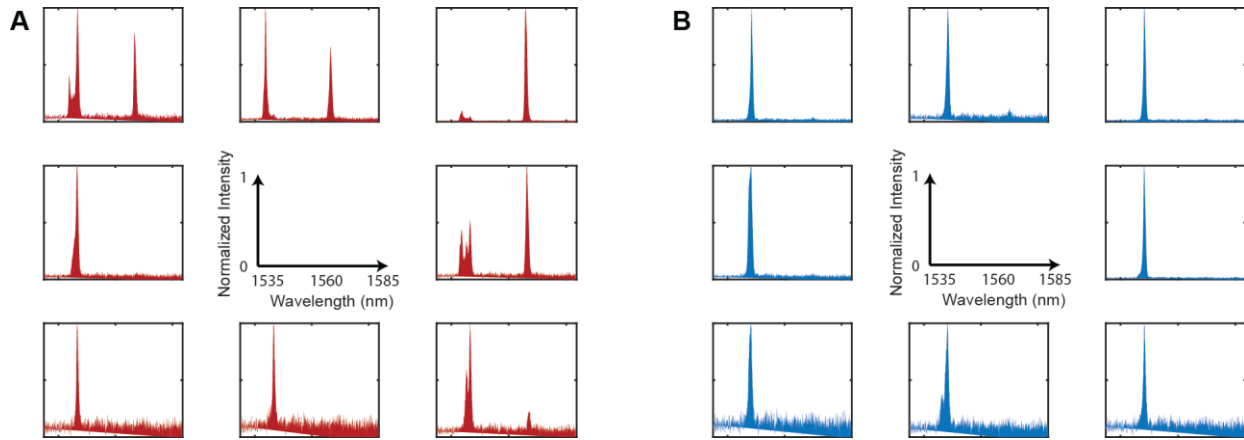


Figure 35 Spectra along the perimeter for (A) trivial and (B) topological sample. The axes are the same for all graphs and are denoted in the center.

3.3.4 Calibration of output couplers

The out-coupling gratings were calibrated such as to allow a comparison of their emitted intensities. To this end, two knife edges were introduced into the pump beam, one covering the gratings completely, the other edge blocking most of the array leaving only the closest rings to the grating to be pumped (Fig. 36 (A)). A camera image at low pump power and without the notch filter (Fig. 33 (A)) is shown in Fig. 36 (B). Employing OD filters in order to not saturate the camera, all micro-resonator arrays were pumped at the same pump level and the total output of

each grating output port was determined (example of a raw data set in Fig. 36 (C)). By this means, the light-light curves in Fig. 30 were corrected.

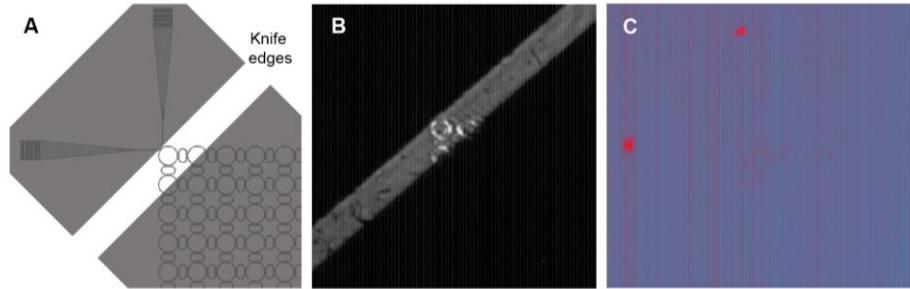


Figure 36 (A) Pumping scheme of micro-resonator arrays. (B) Camera image of a sample pumped as shown in (A). (C) Recorded intensity profiles from the two out-coupling ports.

3.3.5 Mode directionality depending on pumping conditions

Pumping conditions were found to have a great impact on the directionality of the mode and coupling to the probing grating. With an OD filter inserted at 45 degrees into the pump beam (Fig. 37 (A)) the two ports were selectively excited depending on the position of the OD filter. The field intensity profiles at two different configurations are shown in Fig. 37 (B, C) with the corresponding spectra from both ports to the right. It is clearly visible that depending on the position of the filter the excited out-coupling port changes and hence the direction of the edge-mode.

3.3.6 FDTD simulation of microring resonator involving an S-bend

In order to further understand the principles behind the chiral operation of the S-bend microresonators, we analyzed an individual primary S-microring resonator, as shown in Fig. 38, identical to those embedded in our topological array shown in Fig. 31. To do so, we used finite-difference-time-domain method to analyze the temporal evolution of a pulse in this type of cavities,

both for the clockwise and anti-clockwise modes. Figure 38 shows this time dependence for the anti-clockwise mode, where an exponential decay in the pulse peaks is detected.

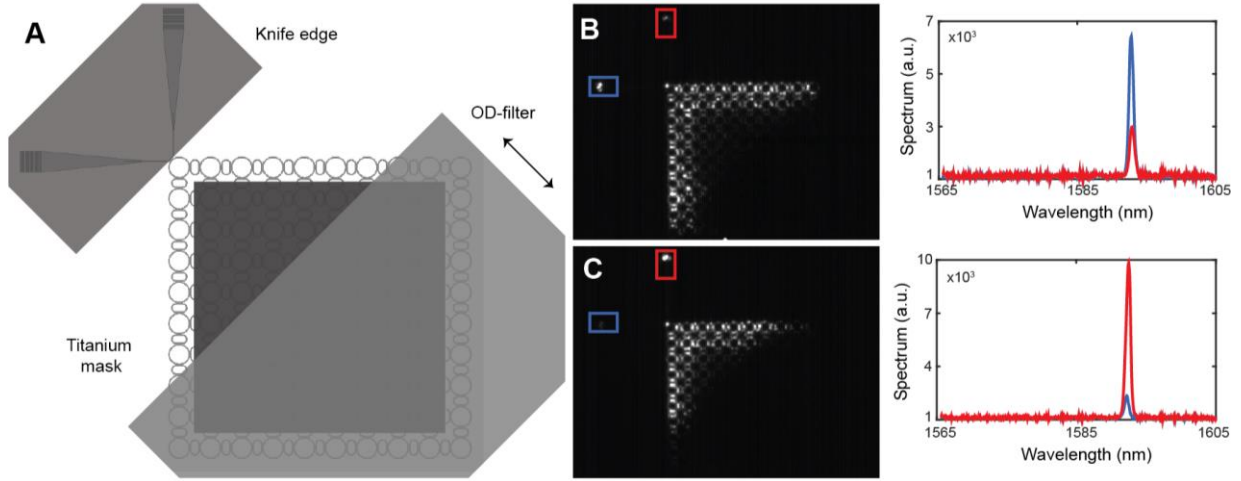


Figure 37 (A) pumping configuration, (B) and (C) field intensity profiles at different OD filter positions with spectra of the two ports to the right.

Using this method, the differential photon lifetime can be deduced from the corresponding lifetimes of the two counter-propagating modes of this chiral cavity using $1/\Delta\tau_p = 1/\tau_{p1} - 1/\tau_{p2}$, resulting in $\Delta\tau_p = 3 \text{ ps}$ and subsequently $\Delta\alpha \sim 10 \text{ cm}^{-1}$.

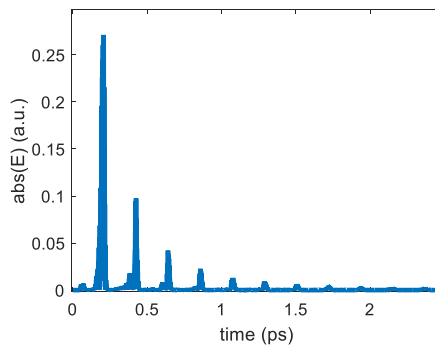


Figure 38 Exponential decay in the amplitude of an anti-clockwise pulse in an S-microresonator cavity identical to those implemented in the design of Fig. 32.

3.4. Summary

Topological insulators are a new phase of matter which have insulating properties in their bulk but are conductors in their edges. This peculiar behavior is a result of the particular band structure in these systems, where a nontrivial bandgap is a host of topologically protected “edge modes”. Moreover, this conduction in the edge is fundamentally different from a conventional conductor, in the sense that it is unidirectional and robust against local perturbations. Our idea was to properly implement such robustness and unique behavior of topological insulators in arrays of laser systems. Laser cavities are in general prone to disorder, which is inevitable due to fabrication imperfections, operational degradation and failure. It is well-known that the presence of disorder in a laser results in spatial light localization in the cavity, giving rise to several performance issues including lower output coupling, multimode lasing and reduced slope efficiency. Therefore, it is natural to contemplate exploiting topological features to design laser systems that are immune to disorder.

In our research, we introduced the “topological insulator lasers” in 1D and 2D. In 1D, we developed a successful theoretical model that captures the complex dynamics of photons in the system which involves a mixture of nonlinear effects including gain saturation, carrier dynamics associated with the gain material, as well as linewidth enhancement effect. We then designed an experimental realization for our theoretical model based on semiconductor multilayer quantum well structures (InGaAsP material), and used the operational parameters associated with the experimental setup in my simulations to predict the behavior of the system under different pumping levels. We successfully demonstrated that the introduction of topology in 1D lasers leads into robust lasing in the defect mode of the structure with ultra-stable emission frequency, in sharp

contrast to conventional 1D lasers which are highly prone to disorder. We further generalized our ideas to higher dimensions and devised a 2D topological insulator laser. After fabrication, our measurements confirmed our theoretical predictions regarding desirable attributes of the 2D topological insulator laser in contrast to a conventional laser array. More specifically, we were able to observe scatter-free, single edge-mode lasing even in pump powers well above lasing threshold. This in turn led into a considerably higher slope-efficiency as compared to trivial systems. In addition, our predictions in terms of spectral purity of the emission from the device were confirmed by detailed experimental measurements.

CHAPTER 4: SPIN-LIKE BEHAVIOR AND GEOMETRICAL FRUSTRATION IN NANOLASER ARRAYS

4.1. Introduction

Geometric frustration occurs when a certain type of local order, associated with a minimum energy state, cannot extend throughout a system due to geometrical constraints [108]. This effect appears in a variety of physical problems and settings, ranging from residual entropy in water [109] and spin ice [110,111], to orbital exchange in Mott insulators [112] and the emergence of the blue phases in cholesteric liquid crystals [113]. In magnetic materials, frustration is typically associated with a set of highly degenerate ground states of a spin Hamiltonian, which in turn leads to complex macroscopic behaviors such as those observed in spin-liquid or spin-ice phases [114].

In recent years, there has been a number of attempts to cast various computational optimization problems in terms of finding the ground state of a corresponding spin Hamiltonian [115,116]. In this regard, ultracold atomic platforms have been extensively pursued to emulate magnetic-like interactions [117–120]. Alternatively, active optical configurations provide an attractive approach for physically implementing and effectively studying such spin Hamiltonians. In contrast to other methodologies that rely on classical or quantum annealing, optical schemes can quickly converge to the global minimum loss, once gain is introduced. This has incited a flurry of activities in designing photonic “machines” capable of emulating classical Ising or XY Hamiltonians. So far, such active spin systems have been demonstrated using optical parametric oscillators [121–123], polaritonic arrangements [124,125], and degenerate laser cavities [126,127]. Of interest will be to open up new possibilities by introducing additional degrees of freedom through the vectorial nature of the electromagnetic modes in ultracompact spin-like optical resonant structures. Such systems

can enable addressing large-scale optimization problems in nanoscale integrated platforms.

In this chapter, we show how the interactions among resonant vectorial modes in coupled metallic nanolaser arrays lead to Hamiltonians akin to those encountered in classical XY spin systems. Consequently, by designing the array elements, two regimes of exchange coupling can be identified, signifying the occurrence of a ferromagnetic (FM) and an antiferromagnetic (AF) phase (Fig. 39 a). By observing the diffraction patterns as well as the winding numbers associated with the vortices formed within the structures, one can then experimentally characterize these phases. Depending on the vectorial profile of the modes involved, in the AF state, we demonstrate geometrical frustration in various scenarios, in full accord with theoretical predictions. In what follows, we will outline the mathematical foundation required to explain our results and will present experimental observations corroborating the role of the vectorial nature of light in producing spin-like behaviors in active optical nanocavities – a response that is in sharp contrast with scalar optical settings or oscillator networks [128–130].

4.2. Theory of coupled metallic nanolasers

To illustrate the spin-like behavior in metallic nanolaser arrays, we consider a circular array of N identical metallic nanodisk lasers, as depicted in the SEM image of Fig. 39b for $N = 6$. Here, the coupling between the nearest-neighbor cavity elements takes place via their overlapping near-fields. In the weak coupling regime, one can obtain the transverse distribution of the resonant electromagnetic fields within the nanodisk j from the corresponding longitudinal component of

the electric (magnetic) field of the associated TM (TE) mode, i.e. $\psi_j \propto J_n(k_\rho \rho) \cos(n\phi + \phi_j)$. The integer n denotes the azimuthal mode number, while ϕ_j is the relative phase with respect to the local coordinates of each site. In such an arrangement, the metallic cladding leads to a mode-dependent dissipation. More specifically, the average power loss for the TE_{nm} and TM_{nm} modes can be expressed as

$$\mathcal{P}_L \propto \begin{cases} \mathcal{P}_1 - \mathcal{P}_{z,TE} \sum_{j=1}^N \cos\left(j \frac{2\pi}{N} n + \phi_j\right) \cos\left(-n\pi + j \frac{2\pi}{N} n + \phi_{j+1}\right) \\ \quad + \mathcal{P}_{\phi,TE} \sum_{j=1}^N \sin\left(j \frac{2\pi}{N} n + \phi_j\right) \sin\left(-n\pi + j \frac{2\pi}{N} n + \phi_{j+1}\right), & TE \\ \mathcal{P}_2 + \mathcal{P}_{\phi,TM} \sum_{j=1}^N \cos\left(j \frac{2\pi}{N} n + \phi_j\right) \cos\left(-n\pi + j \frac{2\pi}{N} n + \phi_{j+1}\right), & TM. \end{cases} \quad (4.1)$$

In Eq. 4.1, $\mathcal{P}_{1,2}$ represent constant loss terms for the TE, TM modes, while \mathcal{P}_z and \mathcal{P}_ϕ depend on the relative strengths of the longitudinal (H_z) and transverse (H_ϕ) magnetic field components, respectively (see section 4.6). The resulting lasing supermodes supported by this lattice can then be found by minimizing the total loss function \mathcal{P}_L which defines the energy landscape of the system. In order to preserve the discrete symmetry associated with the geometry of the structure, the respective solutions are expected to exhibit a constant discrete rotation $\Delta\phi$ between consecutive cavity elements, i.e. $\phi_{j+1} = \phi_j + \Delta\phi$. Equivalently, the extrema of Eq. 4.1 correspond to the minimum energy eigenstates of the following Hamiltonian (\mathcal{H}) (see section 4.6):

$$\mathcal{H} = \mathcal{H}_{\text{XY}} + \mathcal{H}_0,$$

$$\mathcal{H}_{\text{XY}} = \sum_{j=1}^N J_{j,j+1} \vec{\sigma}_j \cdot \vec{\sigma}_{j+1}, \quad (4.2)$$

$$\mathcal{H}_0 = \sum_{j=1}^N J_{0j,j+1} \cos[\phi_j + \phi_{j+1} + 2j \times 2n\pi/N],$$

where \mathcal{H}_{XY} is the XY Hamiltonian describing exchange interactions between the ensuing classical pseudospins defined in each laser cavity as $\vec{\sigma}_j = (\cos \phi_j, \sin \phi_j)$, while \mathcal{H}_0 represents a Hamiltonian component responsible for lifting the continuous U(1) symmetry within individual cylindrical disks. The corresponding coupling strengths J and J_0 for the TE and TM modes are polarization dependent and are respectively given by $J_{\text{TE}} = (\mathcal{P}_{\phi, \text{TE}} - \mathcal{P}_{z, \text{TE}})/2 \times (-1)^n$, $J_{0, \text{TE}} = (\mathcal{P}_{\phi, \text{TE}} + \mathcal{P}_{z, \text{TE}})/2 \times (-1)^{n+1}$ and $J_{0, \text{TM}} = J_{\text{TM}} = \mathcal{P}_{\phi, \text{TM}}/2 \times (-1)^n$. Meanwhile, the second term \mathcal{H}_0 in the Hamiltonian can lead to additional minima in the eigenvalue spectrum of the system. Depending on the modes involved, such states with minimal dissipation can coincide with those associated with the original XY Hamiltonian, or may introduce new stable lasing supermodes. As we will show, in the latter case, this will induce richer frustration patterns in the lasing eigenstates of such nanolaser lattices.

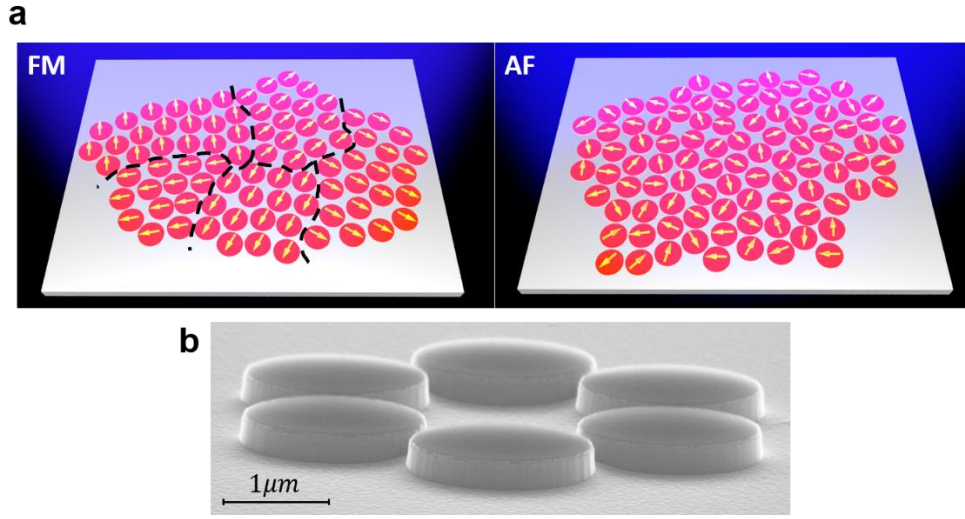


Figure 39 Spin-like behavior in coupled metallic nanolaser arrays. a, Different regimes in spin systems with ferromagnetic (FM) and anti-ferromagnetic (AF) exchange interactions. b, SEM image of an array of six coupled active nanodisks (before silver deposition) used in this study.

The Hamiltonian presented in Eq. 4.2 can give rise to a variety of field patterns corresponding to ferromagnetic-like (FM) or antiferromagnetic-like (AF) interactions between neighboring pseudospins $\vec{\sigma}_j$. For instance, as shown in Fig. 40 a, in a simple two-element arrangement, the resonant TE_{22} mode leads to a negative exchange, $J_{TE} < 0$, that in turn results in an FM-like coupling between the associated pseudospins. On the other hand, for a similar configuration albeit with a slightly different size, once the TE_{14} lasing mode dominates, the underlying coupling becomes positive ($J_{TE} > 0$), as expected from an AF Hamiltonian (Fig. 40 b). When dealing with larger lattices, the AF coupling condition can lead to more complex ground states. In this respect, the competing interactions arising from various nearest neighbor couplings can result in a scenario where the anti-aligned solution is prevented from extending across the entire structure due to geometrical constraints. Consequently, instead of having a single global minimum, the energy

spectrum of the respective Hamiltonian acquires multiple local minima – representing a set of degenerate ground eigenstates, the so-called geometrically frustrated states. Perhaps the simplest known example of such an effect is the way three magnetic spins with AF couplings can arrange themselves on a triangle. Figures 4.0 c show two possible degenerate ground states of such a system with opposite winding numbers (± 1). The geometric frustration in this three-coupled nanolaser configuration is evident in Figs. 4.2 c, d. We note that in this three-element system, the degeneracy between the two eigenstates shown in Figs. 4.0 c, d can be lifted in the presence of \mathcal{H}_0 , in which case, the vortex mode with winding number $+1$ emerges as the ground state.

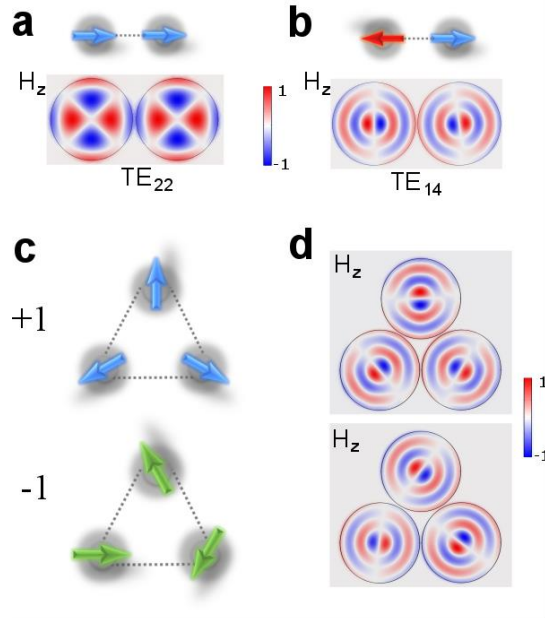


Figure 40 Lasing supermodes in coupled nanolasers and their corresponding pseudospins when arranged in simple geometric configurations. a, Ferromagnetic and b, anti-ferromagnetic interactions between pseudospins associated with the longitudinal component of the magnetic field in coupled nanodisk lasers. Depending on the size of the individual elements (575 nm in a, or 930 nm in b), different TE_{22} and TE_{14} electromagnetic modes predominantly lase, leading to an FM and an AF regime of coupling between nanodisk dimers. c, Geometrically frustrated ground states of the classical XY Hamiltonian corresponding to vortices with opposite winding numbers +1 (top) and -1 (bottom). d, Resonant electromagnetic supermodes in a triangular array of AF-coupled metallic nanodisks associated with the frustrated states of c.

4.3. Observing ferromagnetic and antiferromagnetic behavior in coupled nanolasers

In order to experimentally demonstrate the aforementioned FM and AF behaviors in nanolaser networks, we fabricated multiple structures consisting of several coupled elements. Figure 39 b shows a scanning electron microscope (SEM) image of an array with $N = 6$ coupled nanodisks before metal deposition. Each nanodisk is cladded with silver, and is separated from its adjacent

elements through a metallic silver gap. The gain medium comprises of six InGaAsP quantum wells (with an overall height of 200 nm) and is covered by a 10 nm InP layer for protection. The top and bottom sides of each disk are terminated nominally by a 50 nm SiO₂ and a 30 nm air plug, respectively (section 4.7). The nanolaser arrays are characterized using a micro-photoluminescence setup as described in section 4.8. In order to identify the pertinent cavity lasing modes, we closely study the experimentally observed diffraction patterns for structures of various sizes in terms of their spatial profile, polarization, and wavelength. Along these lines, different states (FM and AF) are promoted by varying the size of the nanodisks involved as well as the lattice configuration. In some cases, laser ambient temperature has been adjusted (78K to room-temperature) in order to match the desired cavity mode with the gain lineshape of the active medium.

Figure 41 presents experimental results demonstrating FM and AF behaviors in arrays involving four nanodisk lasers. For characterizing the FM-like response ($J < 0$), we designed cavity elements having a radius of 575 nm and a 50 nm separation from its nearest neighbors. Our FEM simulations indicate that the individual disks tend to predominately lase in the TE_{22} mode. Meanwhile, from Eq. 4.2 one can conclude that in such polygonal arrays comprised of four elements, this same mode can give rise to an FM-like exchange coupling between adjacent pseudospins. The resulting ground state corresponding to this case is illustrated in Figs. 41 a-c, along with experimental results, corroborating these predictions. On the other hand, a different design is used in order to observe AF-like interactions. In this case, the nanodisk elements involved in the $N = 4$ array have a radius of 940 nm and are separated from each other by 50 nm . From simulations, this cavity is expected to lase instead in the TE_{14} mode – at a wavelength coinciding with the gain bandwidth of the QWs.

Unlike the FM case, here the exchange term is positive ($J > 0$), resulting in an anti-aligned field distribution in the neighboring elements (Figs. 41 d-f). The experimental results corresponding to the AF case were obtained at a wavelength of 1415 nm . In all cases depicted in Fig. 41, the fields are aligned in such a way so as to enable the system to reach its global minimum in the energy landscape.

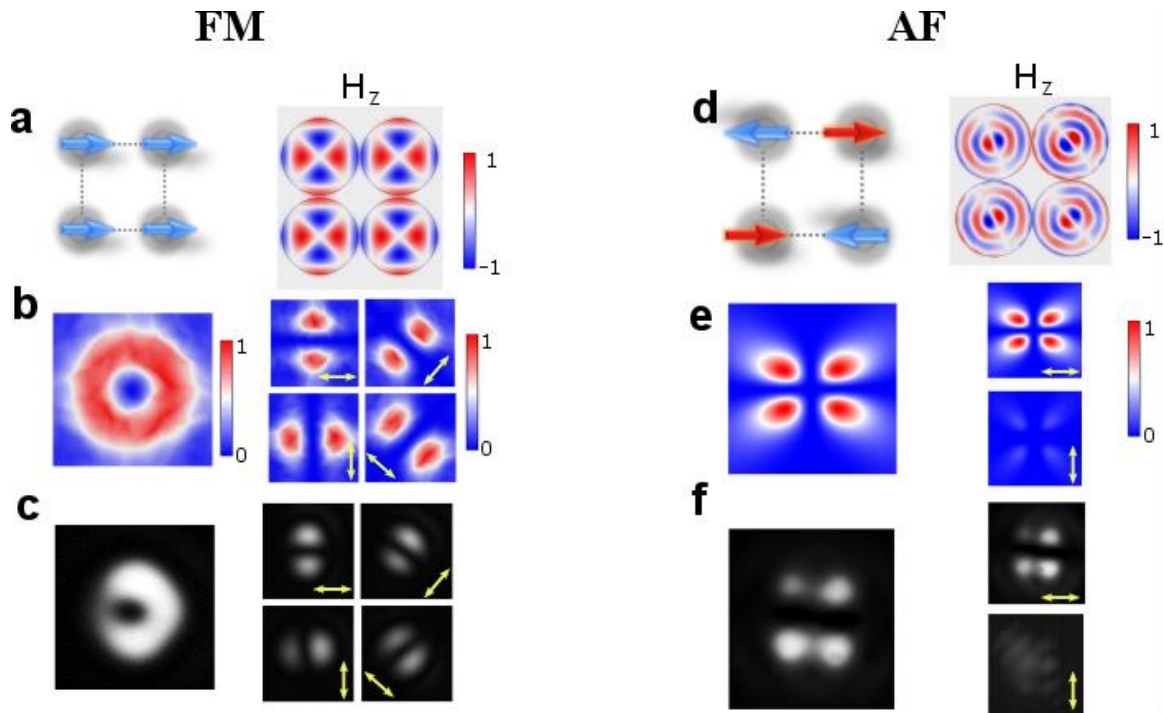


Figure 41 FM and AF interactions in four-element coupled nanodisk lasers. Observation of FM (a-c) and AF (d-f) states in different scenarios of coupled metallic nanolasers with various sizes. a, Longitudinal magnetic field profiles corresponding to the lasing TE_{22} mode in four coupled nanodisks of radius 575 nm . b, Theoretically predicted and c, experimentally measured optical field intensities and polarization characteristics of the light emitted by such an array. d-f, Similar results for the AF case where nanodisks having radii of 940 nm are employed in the same square geometry. The yellow arrows indicate the direction of the linear polarizer. No geometric frustration is observed in either the FM or the AF regimes.

4.4. Geometric frustration in nanolaser lattices

We next consider situations where the competing constraints imposed by dissipative interactions among nearest neighbors lead to geometric frustration. Such states occur in AF systems with $J > 0$, in which case the ground state of the optical Hamiltonian no longer follows an anti-aligned field distribution because of the geometry of the lattice configuration itself. To experimentally demonstrate such states, we fabricated two arrays with $N = 3, 5$ elements, where each nanodisk has a radius of 930 nm . FEM simulations in this case predict a TE_{14} lasing mode in each element. Figures 42 a-h show simulation results of the arrays together with experimentally measured intensity profiles and topological charges associated with the lasing supermodes of these lattices. The associated pseudospins in these cases display a 120° and 144° rotation between consecutive elements, respectively (illustrated in Figs. 42 c, g). These results match the geometrically frustrated ground states of the XY Hamiltonian. As mentioned earlier, in some cases, the presence of the second term \mathcal{H}_0 in Eq. 4.2 poses additional constraints on the ground states of the system. An interesting example in this regard is the case of a hexagonal nanodisk laser arrangement ($N = 6$) with AF interactions, exhibiting geometric frustration (Fig. 42 i). To observe this behavior, we fabricated 850 nm nanodisks, each supporting a TE_{13} lasing mode. In this scenario, the competing interactions described by \mathcal{H}_{XY} and \mathcal{H}_0 lead to a frustrated ground state with successive 120° rotations between adjacent pseudospins, as shown in Figs. 42 i-k.

The geometrically frustrated states in Fig. 42 represent vortices with a nonzero topological charge. One can map the corresponding orbital angular momenta to a discrete set of spots by monitoring the far-field diffraction patterns after passing through an equilateral triangular aperture [131]. Using this technique, a light beam carrying orbital angular momentum (OAM) with

charge q , emerges in the far field as a triangular intensity distribution with $|q| + 1$ spots on each side. Moreover, the sign of the associated topological charge can be inferred from the direction of this diffracted triangular pattern (see section 4.8). Experimental results obtained from such measurements for $N = 3, 5, 6$ lattices are depicted in Figs. 42 d, h, l, clearly indicating that in these cases the vortex charge is $l = +1, -2, -2$, respectively. One may improve the characterization precision of the modal profile of the lattice by using near field scanning microscopy.

4.5. Lasing in the ferromagnetic state of a square lattice

In order to extend our analysis to larger arrays, we consider a square lattice of FM coupled nanolasers involving 20×20 elements (Figs. 43 a-c). Each nanolaser in this structure is designed so as to emit in the TE_{22} lasing mode at $\lambda = 1445 \text{ nm}$. The far-field diffraction from this array was experimentally characterized both below and above the lasing threshold. As shown in Fig. 43 d, in the sub-threshold regime, the spontaneously emitted far-field has a Gaussian profile and is unpolarized (Fig. 43 b) – in a way analogous to that anticipated from randomly-oriented pseudospins. As the power of the optical pump is increased, the structure starts to lase and consequently the system settles in the FM ground state of the XY Hamiltonian where the corresponding pseudospins are all aligned (Fig. 43 c). This FM state is corroborated by far-field and polarization measurements – as expected from the emission of aligned vectorial fields in this nanolaser system (Fig. 43 e). In this regard, the pump sets the “temperature” in this platform, as in actual magnetic materials [127,132].

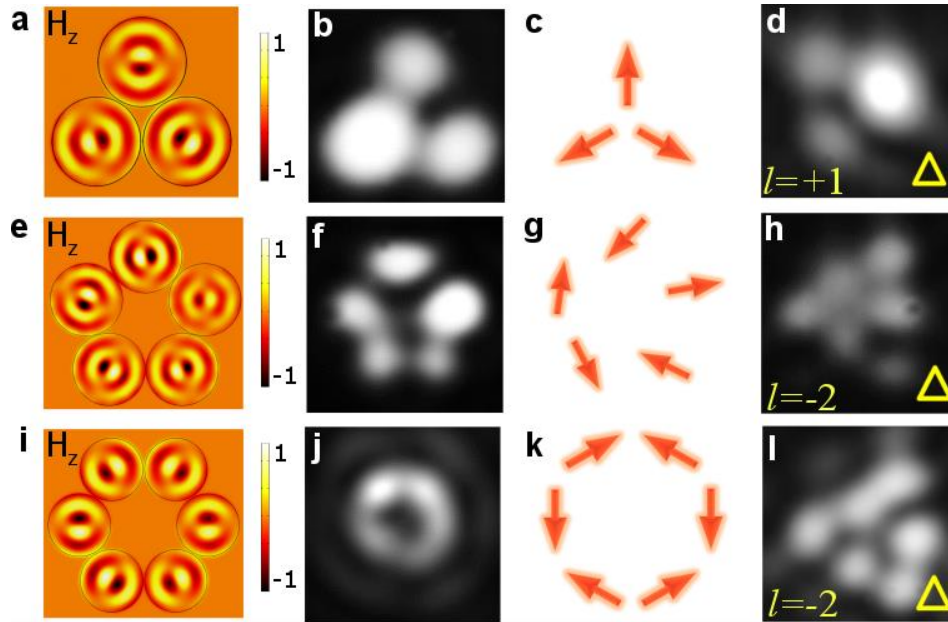


Figure 42 Frustrated states in spin-like lasing fields emerging from nanolaser arrays. a, Simulated lasing profile, b, experimentally measured optical intensities, and c, associated pseudospin configuration for a geometrically frustrated lasing supermode emitted from an $N = 3$ nanolaser array with an AF-type interaction. In this case each nanodisk has a radius of 930 nm , leading to a TE_{14} cavity mode. d, Optical intensity pattern obtained after diffraction from a triangular aperture, indicating a topological charge of $l = +1$, as expected from the pseudospin arrangement of c. e-h & i-l present similar results for $N = 5$ and $N = 6$ nanolaser arrays involving elements with radii 930 nm and 850 nm (TE_{13} mode), respectively. Note that for these structures the triangular diffraction pattern indicates an $l = -2$ topological charge (h & l). The triangular diffraction measurements were all performed by incorporating a $\lambda/4$ waveplate before the aperture followed by a linear polarizer so as to filter for the right-hand circularly polarized component.

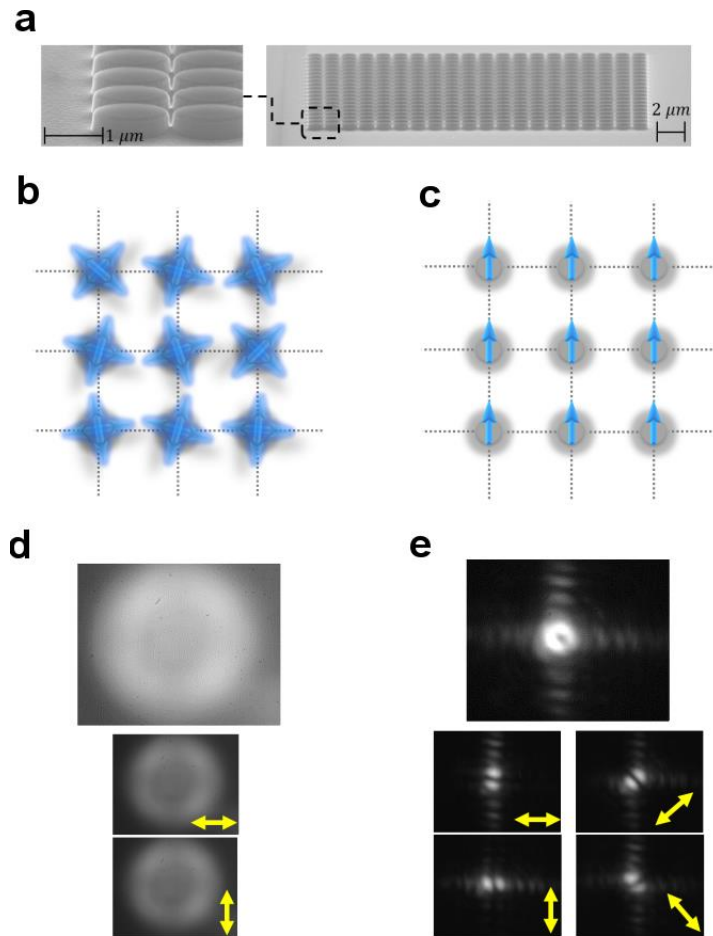


Figure 43 Square lattice of 20×20 nanolasers exhibiting FM spin-like behavior. a, SEM image of a 20×20 square lattice of coupled active nanodisks used in this study. b, Below the lasing threshold, the orientation of the pseudospins associated with the electromagnetic TE_{22} mode within each laser element are randomly fluctuating. c, Once the pump exceeds the threshold, the array starts to lase in an FM state, with the pseudospins aligned in the same direction. d & e, Experimentally measured optical intensity patterns and polarization characteristics of the light emitted by this square lattice below (spontaneous emission) and above the lasing threshold, respectively. In the lasing regime, the far-field from this nanolaser square lattice clearly indicates in-phase coherent emission in the TE_{22} mode (ferromagnetic state). The yellow arrows indicate the orientation of the linear polarizer.

4.6. Derivation of the energy landscape function

In order to obtain the resonant modes supported by the nanodisks, we consider the two general sets of transverse electric (*TE*) and transverse magnetic (*TM*) modes. Using separation of variables, and after solving the Helmholtz equation in cylindrical coordinates, one finds the field components for TE_{nm} modes in a nanodisk at site j as

$$\begin{aligned}
 E_{\rho,j} &\propto \frac{n}{\rho} J_n(k_\rho \rho) \sin(n\phi + \phi_j), \\
 E_{\phi,j} &\propto \frac{k_\rho}{2} [J_{n-1}(k_\rho \rho) - J_{n+1}(k_\rho \rho)] \cos(n\phi + \phi_j) \\
 E_{z,j} &= 0 \\
 H_{\rho,j} &\propto \frac{-\sqrt{k^2 - k_\rho^2} \times k_\rho}{2\omega\mu_0} [J_{n-1}(k_\rho \rho) - J_{n+1}(k_\rho \rho)] \cos(n\phi + \phi_j) \quad (4.3) \\
 H_{\phi,j} &\propto \frac{n\sqrt{k^2 - k_\rho^2}}{\omega\mu_0\rho} J_n(k_\rho \rho) \sin(n\phi + \phi_j) \\
 H_{z,j} &\propto \frac{ik_\rho^2}{\omega\mu_0} J_n(k_\rho \rho) \cos(n\phi + \phi_j).
 \end{aligned}$$

On the other hand, the expression for the total dissipated electromagnetic power due to the metallic walls can be obtained from the surface integrals

$$\begin{aligned}
\mathcal{P}_{L,T} \propto & \sum_{j=1}^N \int_{S_j} [|H_{\phi,j}|^2 + |H_{z,j}|^2] ds \\
& - \Delta S \sum_{j=1}^N \left\{ |H_{z,j}|^2 + |H_{z,j+1}|^2 - |H_{z,j+1} - H_{z,j}|^2 \right\} \\
& + \left\{ |H_{\phi,j}|^2 + |H_{\phi,j+1}|^2 - |H_{\phi,j+1} + H_{\phi,j}|^2 \right\},
\end{aligned} \tag{4.4}$$

where S_j is the cylindrical surface of the j th nanodisk, while ΔS is the effective common area between nearby nanodisks. From equations (S-1), one can further simplify equation (S-2) as follows

$$\begin{aligned}
\mathcal{P}_{L,TE} \propto & \mathcal{P}_1 - \mathcal{P}_{z,TE} \sum_{j=1}^N \cos\left(j \frac{2\pi}{N} n + \phi_j\right) \cos\left(-n\pi + j \frac{2\pi}{N} n + \phi_{j+1}\right) \\
& + \mathcal{P}_{\phi,TE} \sum_{j=1}^N \sin\left(j \frac{2\pi}{N} n + \phi_j\right) \sin\left(-n\pi + j \frac{2\pi}{N} n + \phi_{j+1}\right)
\end{aligned} \tag{4.5}$$

where $\mathcal{P}_{z,TE} = 2\Delta S \frac{k_\rho^4}{\omega^2 \mu_0^2} J_n^2(k_\rho a)$, $\mathcal{P}_{\phi,TE} = 2\Delta S \frac{n^2(k^2 - k_\rho^2)}{\omega^2 \mu_0^2 a^2} J_n^2(k_\rho a)$, and a is the radius of the nanodisks. Equation (S-3) can be rewritten as

$$\begin{aligned}
\mathcal{P}_{L,TE} \propto & \mathcal{P}_1 + (-1)^{n+1} \sum_{j=1}^N \left\{ \frac{\mathcal{P}_{z,TE} - \mathcal{P}_{\phi,TE}}{2} \cos[\phi_{j+1} - \phi_j] \right. \\
& \left. + \frac{\mathcal{P}_{z,TE} + \mathcal{P}_{\phi,TE}}{2} \cos\left[\phi_{j+1} + \phi_j + 2j \times \frac{2n\pi}{N}\right] \right\}.
\end{aligned} \tag{4.6}$$

Similarly, for TM_{nm} modes, the fields within cavities are given according to

$$\begin{aligned}
E_{\rho,j} &\propto \frac{-\sqrt{k^2 - k_\rho^2} \times k_\rho}{2\omega\epsilon_0} [J_{n-1}(k_\rho\rho) - J_{n+1}(k_\rho\rho)] \cos(n\phi + \phi_j), \\
E_{\phi,j} &\propto \frac{n\sqrt{k^2 - k_\rho^2}}{\omega\epsilon_0\rho} J_n(k_\rho\rho) \sin(n\phi + \phi_j) \\
E_{z,j} &\propto \frac{ik_\rho^2}{\omega\epsilon_0} J_n(k_\rho\rho) \cos(n\phi + \phi_j) \\
H_{\rho,j} &\propto -\frac{n}{\rho} J_n(k_\rho\rho) \sin(n\phi + \phi_j) \\
H_{\phi,j} &\propto -\frac{k_\rho}{2} [J_{n-1}(k_\rho\rho) - J_{n+1}(k_\rho\rho)] \cos(n\phi + \phi_j) \\
H_{z,j} &= 0.
\end{aligned} \tag{4.7}$$

Therefore, the total dissipated power can again be obtained in a similar way:

$$\mathcal{P}_{L,TM} \propto \mathcal{P}_2 + \mathcal{P}_{\phi,TM} \sum_{j=1}^N \cos\left(j\frac{2\pi}{N}n + \phi_j\right) \cos\left(-n\pi + j\frac{2\pi}{N}n + \phi_{j+1}\right), \tag{4.8}$$

where $\mathcal{P}_{\phi,TM} = \frac{k_\rho^2}{2} \Delta S [J_{n-1}(k_\rho\rho) - J_{n+1}(k_\rho\rho)]^2$. Using this, it is straightforward to show that

$$\begin{aligned}
\mathcal{P}_{L,TM} &\propto \mathcal{P}_2 + (-1)^n \mathcal{P}_{\phi,TM} \sum_{j=1}^N \left\{ \frac{1}{2} \cos[\phi_{j+1} - \phi_j] \right. \\
&\quad \left. + \frac{1}{2} \cos\left[\phi_{j+1} + \phi_j + 2j \times \frac{2n\pi}{N}\right] \right\}.
\end{aligned} \tag{4.9}$$

Equations 4.1 and 4.2 in section 4.2 can be directly extracted from Eqs. 4.5, 4.8 and 4.6, 4.9, respectively. These equations provide the energy landscape functions associated with the Hamiltonians of this system.

4.7. Fabrication procedure and SEM images

The fabrication steps involved in implementing metallic nanolaser lattices are depicted in Fig. 44. The wafer (grown by OEpic Inc.) consists of six quantum wells of $\text{In}_{x=0.734}\text{Ga}_{1-x}\text{As}_{y=0.57}\text{P}_{1-y}$ (thickness: 10 nm), each sandwiched between two cladding layers of $\text{In}_{x=0.56}\text{Ga}_{1-x}\text{As}_{y=0.938}\text{P}_{1-y}$ (thickness: 20 nm), with an overall height of 200 nm, grown on an InP substrate. The quantum wells are covered by a 10 nm thick InP over-layer for protection (Fig. 44 a). An XR-1541 hydrogen silsesquioxane (HSQ) solution in methyl isobutyl ketone (MIBK) is used as a negative electron beam resist. The resist is spun onto the wafer, resulting in a thickness of 50 nm (Fig. 44 b). The lattices are then patterned by electron beam lithography (Fig. 44 c). The wafer is next immersed in tetramethylammonium hydroxide (TMAH) to develop the patterns. The HSQ exposed to the electron beam now remains and serves as a mask for the subsequent reactive ion etching process. To perform the dry etching, a mixture of $\text{H}_2:\text{CH}_4:\text{Ar}$ gas is used with a ratio of 40:6:15 sccm, RIE power of 150 W, and ICP power of 150 W at a chamber pressure of 35 mT (Fig. 44 d). The wafer is then cleaned with oxygen plasma to remove organic contaminations and polymers that form during the dry etching process. After this, a 1000 nm layer of silver is deposited onto the sample using electron beam evaporation at a pressure of 5×10^{-7} Torr at a rate of $0.1 \text{ \AA}/\text{s}$ for the first 400 nm, at which point the rate is ramped up to $1 \text{ \AA}/\text{s}$ (Fig. S1e). SU-8 is then used to bond the silver side to a glass substrate for support (Fig. 44 f). Lastly, the sample is wet etched in hydrochloric acid to remove the InP substrate (Fig. 44 g). SEM images of all lattices discussed in the main text are provided in Fig. 45, after the intermediate dry etching step.

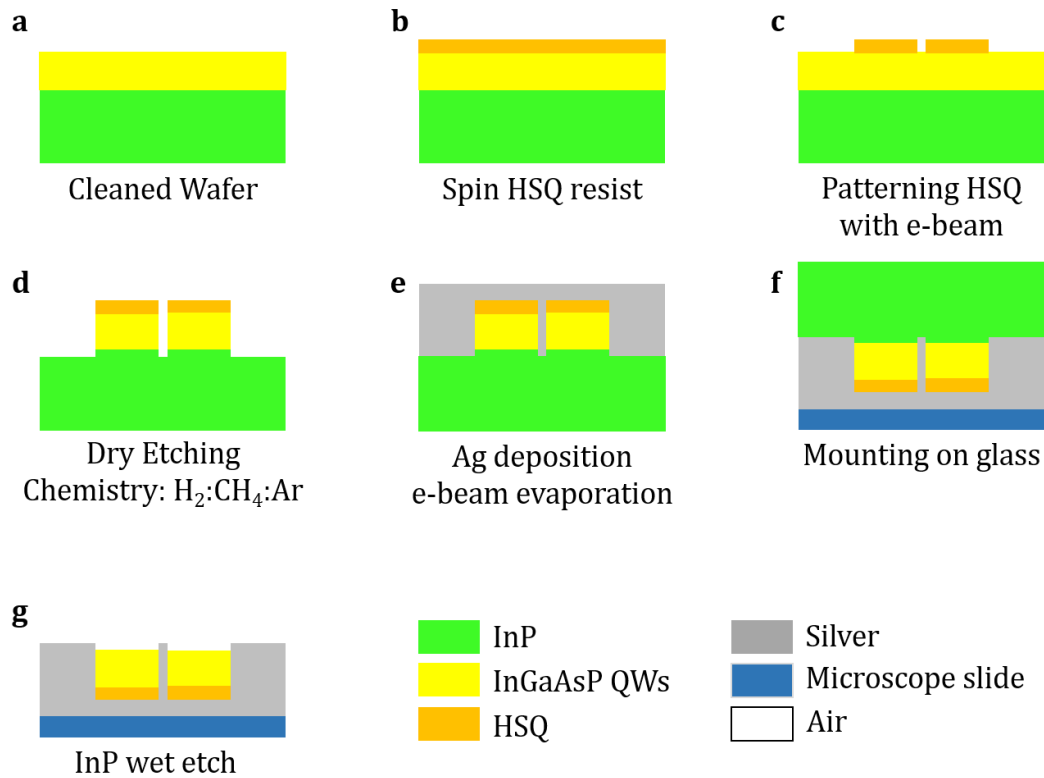


Figure 44 Fabrication process of a metallic nanolaser lattice. This same process is used in other geometries as well. The bottom right corner provides a legend to the materials of the structure. a, Cleaned wafer with InGaAsP quantum wells grown on an InP substrate. b, A thin layer of negative tone HSQ ebeam resist is spun onto the sample. c, The wafer is patterned by ebeam lithography and the resist is developed. d, A dry etching process is used to define the lattice. e, 1 μm Ag is deposited by means of ebeam evaporation. f, The sample is mounted and bonded to a glass microscope slide silver side down with SU-8. g, Sample is

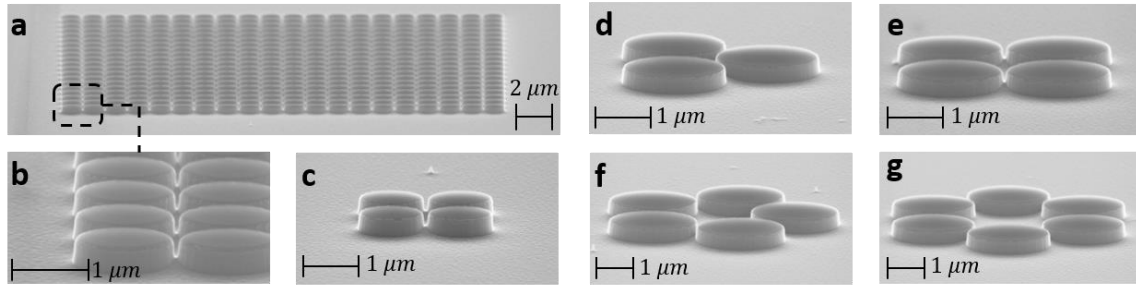


Figure 45 SEM images of the lattices. In all lattices the nanodisks elements are separated by 50 nm. a, 20 x 20 array of nanodisks (radius 545 nm). b, zoomed in view of the front left corner of the 20 x 20 array. c, 4-element array of nanodisks (radius 575 nm). d, e, & f, 3-, 4-, & 5-element arrays (radius 930 nm, 940 nm, and 930 nm, respectively). g, 6-element array (radius 850 nm).

4.8. Characterization setup

A micro-photoluminescence (μ -PL) setup, depicted in Fig. 46, is used to characterize the metallic nanolaser lattices. The lattices are optically pumped by a pulsed laser (duration: 15 ns, repetition rate: 290 kHz) operating at a wavelength of 1064 nm (SPI fiber laser). A beam shaping system is implemented to realize the desired pump profile. In this study, the pump focus spot on the sample has a diameter of 45 μ m. A 50x microscope objective (NA: 0.42) is used to project the pump beam on the lattice and also serves to collect the emission. For temperature tuning, the sample is inserted into a cryostat (Janis ST-500) and cooled. The surface of the sample is imaged by two cascaded 4-f imaging systems in an IR camera (Xenics Inc.). A broadband ASE source passed through a rotating ground glass is used to illuminate the sample surface for pattern identification. A notch filter is placed in the path of emission to attenuate the pump beam. Output spectra are obtained by a monochromator equipped with an attached InGaAs linear array detector. A powermeter is inserted at the focus of the beam to collect the output power of the laser lattices. A linear polarizer

is placed in the setup to observe the polarization resolved intensity distribution. To measure the topological charge of the light emitted by the lattices, a removable equilateral triangular aperture is inserted at the back focal plan of the lens before the IR camera, to facilitate a Fourier-transform. A quarter-wave plate is used to extract the right- and left-handed components of the polarization.

To measure the orbital angular momentum of the emitted light emitted, different techniques can be used based on interference, including self-interference and interference of the OAM beam with a plane wave. In these circumstances, the phase information is assessed by analyzing the fringes. In particular, the formation of a fork-like structure at the center of the vortex is an indication of a topological charge. Here the topological charge measurements are augmented using a different approach based on the relationship between the phase of the light carrying OAM and its diffraction. This latter technique provides an unambiguous measurement of the order and sign of a vortex beam's topological charge. In short, when a *scalar* light beam carrying orbital angular momentum passes through an equilateral triangular aperture, the beam diffracts, hence generating a truncated triangular optical lattice rotated by $\pm 30^\circ$, with respect to the aperture, in the far-field. This lattice then reveals the value of the topological charge (q), given by the relationship $|q| = s - 1$, where s is the number of spots along each side of the formed triangular lattice. The sign of the charge is determined by the direction that the triangle rotates. For example, in our setup, a triangle pointed right has a positive OAM, while the sign is negative if it points to the left.

To establish the validity of the triangular aperture approach for measuring the topological charge of an optical vortex beam, we compare the results of the triangle technique experimentally to that of a simulated vectorially rotating electric field. In the experiment, we tested a 7-element lattice laser at room temperature (Fig 47 a). As the TE_{13} is a quasi-linear like mode, we simulate

this structure by considering six dipoles arranged in a hexagonal ring, emitting radiation with an electric field $\vec{E} \propto -\cos(2\varphi) \hat{x} + \sin(2\varphi) \hat{y}$, where φ is the angle of rotation along the periphery. This in turn can be represented in terms of left- (\hat{L}) and right-hand circular polarizations (\hat{R}) (L,RHCP), $\vec{E} \propto -e^{i2\varphi} \hat{L} - e^{-i2\varphi} \hat{R}$. Figures 47 b, c, & d provide the simulated intensity and the polarization resolved intensity distributions, which are in excellent agreement with the observed modal profiles (Fig. 47 e, f, & g). Figure 47 h shows the result of the simulated diffraction pattern when filtering for the RHCP, and compares it to the experimentally observed diffraction profile (Fig. 47 i). Lastly, the associated light-light (L-L) and spectral evolution curves are provided in Fig. 47 j & k, respectively, clearly showing the threshold characteristic associated with lasing as well as linewidth narrowing.

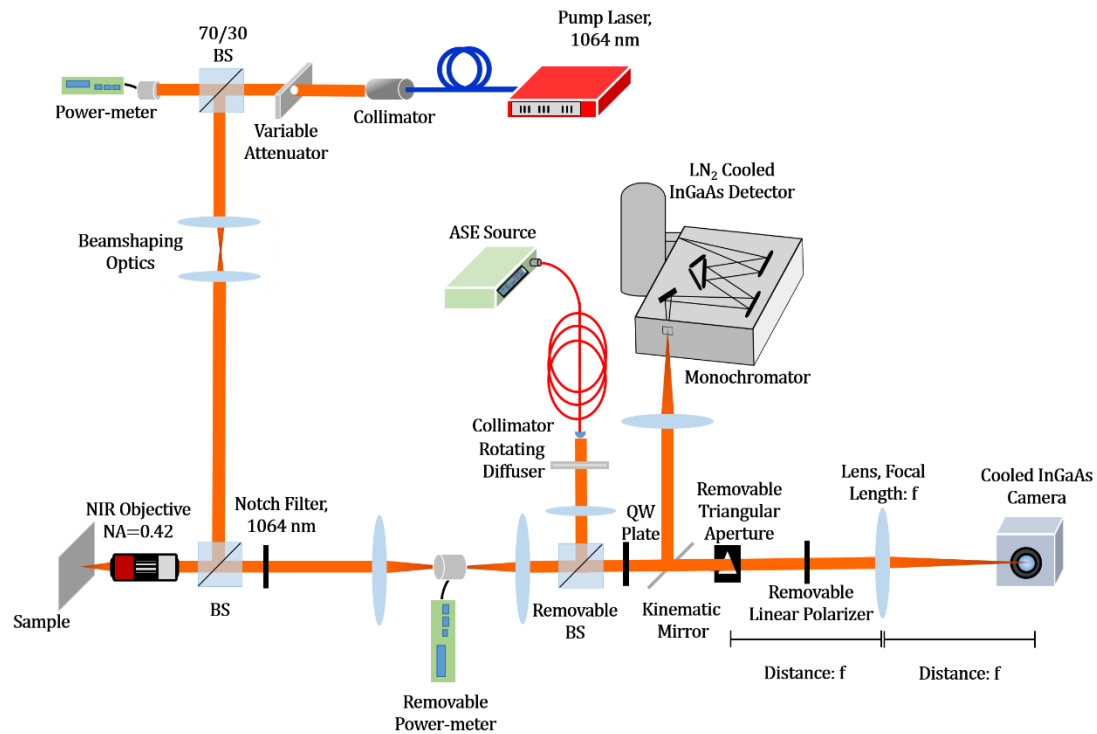


Figure 46 Characterization microphotoluminescence setup schematic. The samples are pumped with a 1064 nm fiber laser and focus onto the sample with a 50x objective (N.A. 0.42). Light is either directed to an InGaAs camera to observe emission patterns, or to a monochromator with an attached InGaAs linear array detector. The emission power is collected at the location of the first focus after the pump notch filter. The triangular aperture used to reveal the OAM of the radiated beams is removable so as to not obstruct imaging the sample surface and to collect proper modal profiles.

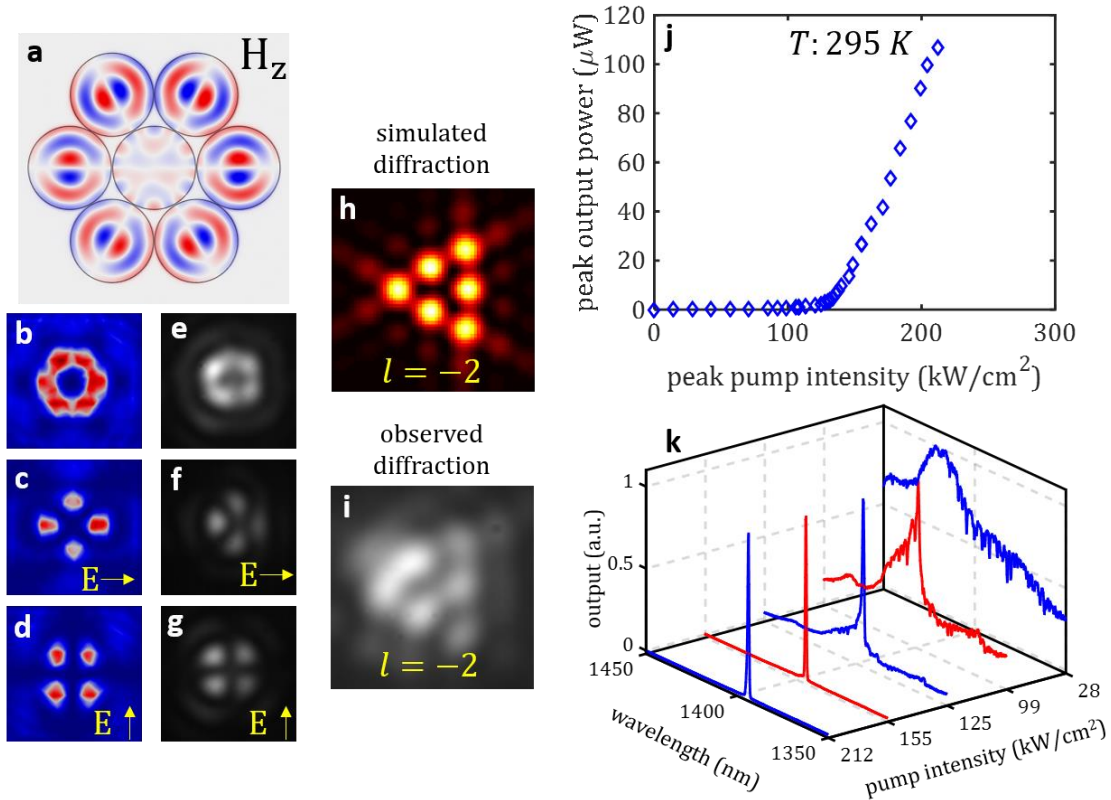


Figure 47 Characterization of charge measurement using a 7-element metallic lattice operating at room temperature. a, Simulated z-component of the magnetic field. b, c, & d, The simulated intensity profile and the polarization resolved intensity distributions when filtered for horizontal (c) and vertical (d) polarizations. e, f, & g, The experimentally observed emission pattern and intensity distributions. h, The simulated far-field diffraction pattern of the lattice after passing through a triangular aperture. i, The experimentally observed profile is in agreement and has $l = -2$. j, The light-light curve shows a clear onset in lasing. k, The spectral evolution of this laser shows linewidth narrowing and single-mode behavior.

4.9. Light-light curves and spectral evolutions

In addition to the emission profile and topological charges provided in the main text, light-light and spectral evolution curves were also collected for these metallic nanolaser lattices. As mentioned before, the ambient temperature of the lasers was tuned in order to promote lasing in certain desired modes. All of the curves shown in this section of the supplementary display a threshold and a linewidth narrowing behaviors with increased pumping, attributes associated with lasing. The reported pump intensities represent the incident light at the sample surface. Figure 48 provides the L-L and spectral evolutions of the four lattices that orient their fields in an antiferromagnetic-like arrangement. The 3-, 4-, & 5-element structures have individual element radii of 930 nm, 940 nm, and 930 nm, respectively, (TE_{14} mode) and are tuned to a temperature of 225 K (Fig. 48 a-f). On the other hand, the 6-element lattice (nanodisk radius of 850 nm) is left at room temperature to promote lasing in the TE_{13} mode (Fig. 48 g & h).

Figure 49 shows the curves for the lattices that orient their fields in a ferromagnetic-like manner. In these lattices all the cavities support the TE_{22} mode. The 4-element arrangement operates at a temperature of 78 K and the characteristics of the L-L and spectral evolution (575 nm nanodisk radius) is provided in Fig. 49 a & b. In the case of the 20×20 element array, the nanodisks have a smaller radius of 545 nm and were operated at an ambient temperature of 225 K (Fig. 49 c & d).

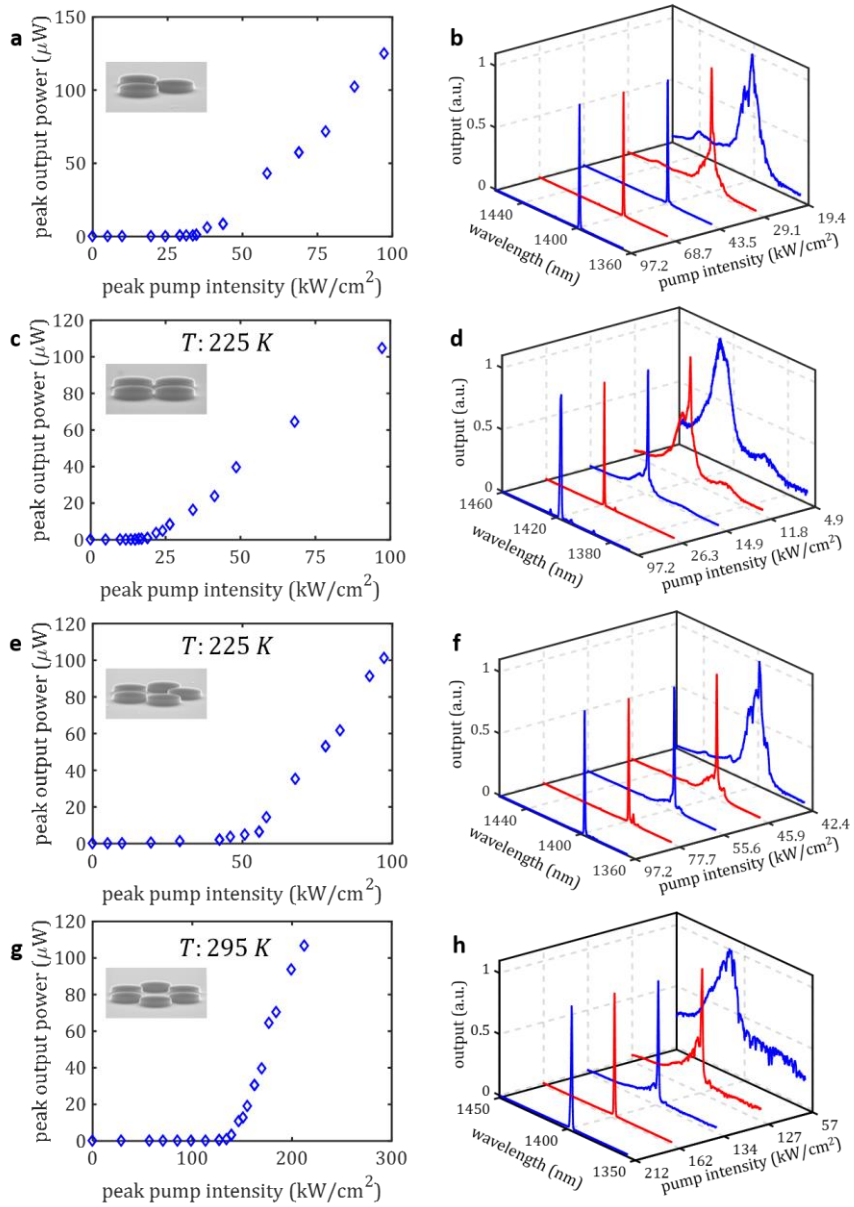


Figure 48 Light-light and spectral evolutions curves for the lattices with antiferromagnetic-like coupling. All the lattices indicate a clear onset of lasing and linewidth narrowing. a & b, c & d, and e & f, show the light-light and the spectral evolutions of lattices operating in the TE_{14} mode at temperature of 225 K for the 3-, 4-, & 5-element lattices, respectively. The radii of the nanodisks are 930 nm, 940 nm, and 930 nm, respectively. g & h the 6-element lattice supports lasing at room temperature in the TE_{13} mode (850 nm radius elements).

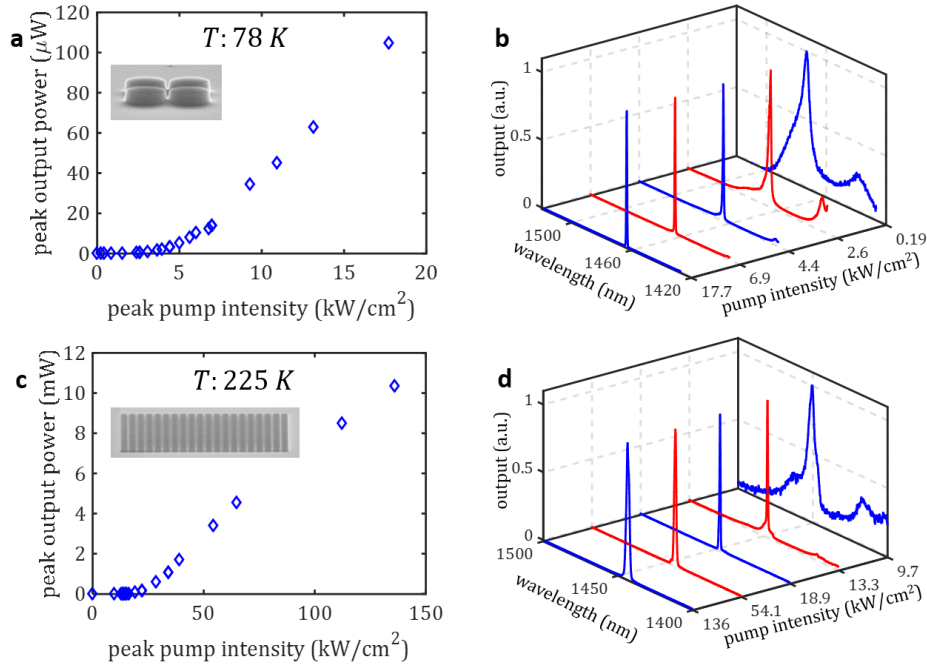


Figure 49 Output characteristics of the 4-element and 20×20 -element array displaying ferromagnetic like coupling. Both lattices operate in the TE_{22} mode, albeit at differing temperatures. a & b, the 4-element arrangement is cooled to 78 K and has disks with radii of 575 nm. c & d, the 20×20 -element lattice (radius of 545 nm) generates more than 10 mW peak output power.

4.10. Tuning the exchange couplings J_{ij}

In order to show the versatility of the coupled nanolaser array platform to realize XY Hamiltonians with various exchange couplings, one may consider varying the metallic gap between nanodisks as a means to adjust the associated exchange couplings in equation (2). To demonstrate this aspect, we study an asymmetric three-element configuration, as depicted schematically in Fig. 50 a. In this configuration, we adjust the relative strengths of the corresponding exchange couplings in the equivalent Hamiltonian of equation (2) such that $J_{12} =$

$J_{13} \approx J_{23}/3$. This is obtained by incorporating a larger gap distance between the top nanodisk and the remaining ones on the bottom of the structure (50 nm versus 25 nm). Each of the nanodisks in this case have a radius of 775 nm and emit in the TE_{13} mode. In this case, one expects that the previous 120° arrangement of the pseudospins in an equilateral geometry to be modified towards an anti-aligned pseudospin configuration for the sites located on the bottom of the triangle, as expected from the limiting case of an AF-like coupled dimer geometry. Figure 50 b shows simulated field profile of the associated supermode with the lowest loss in such a geometry, as expected from such asymmetric couplings. Figures 50 c-h display the measured diffracted field intensities and polarization characteristics of light emitted by such a structure (top) together with the associated simulation results (bottom). The coupling between the adjacent elements can be further tuned by depositing additional metallic barriers using focused ion beams.

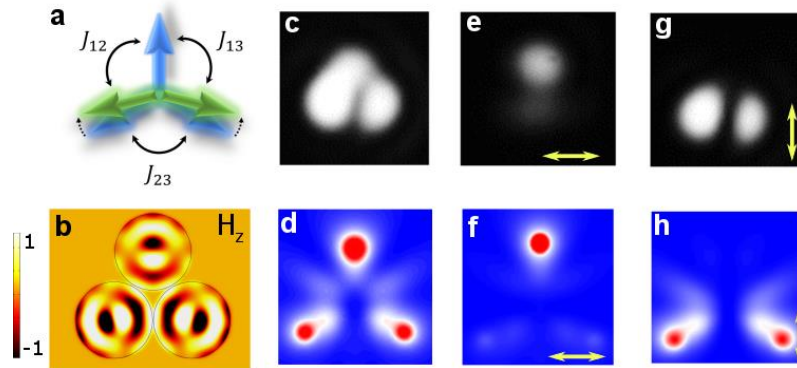


Figure 50 Asymmetric triangle geometry. a, A schematic of three pseudospins arranged on a triangle with asymmetric exchange couplings. In this case, the angles of the bottom pseudospins are expected to change as shown in the figure. b, FEM simulation of the lasing supermode in an asymmetric triangular array of nanodisks. Each nanodisk supports a TE_{13} mode. c-h Experimental measurements (top) together with theoretically calculated results for diffraction intensities and polarization states of the optical fields emitted by such a nanodisk array. The arrows depict the direction of the linear polarizer.

4.11. Polarization measurements for frustrated states

To further characterize the lasing supermodes in the case of arrays with $N = 3, 5, 6$ nanodisk lasers with an AF-type coupling, we performed polarization measurements in each case and compared the results with those expected from simulations (Fig. 51). These observations further corroborate the results in Fig. 42 of the manuscript.

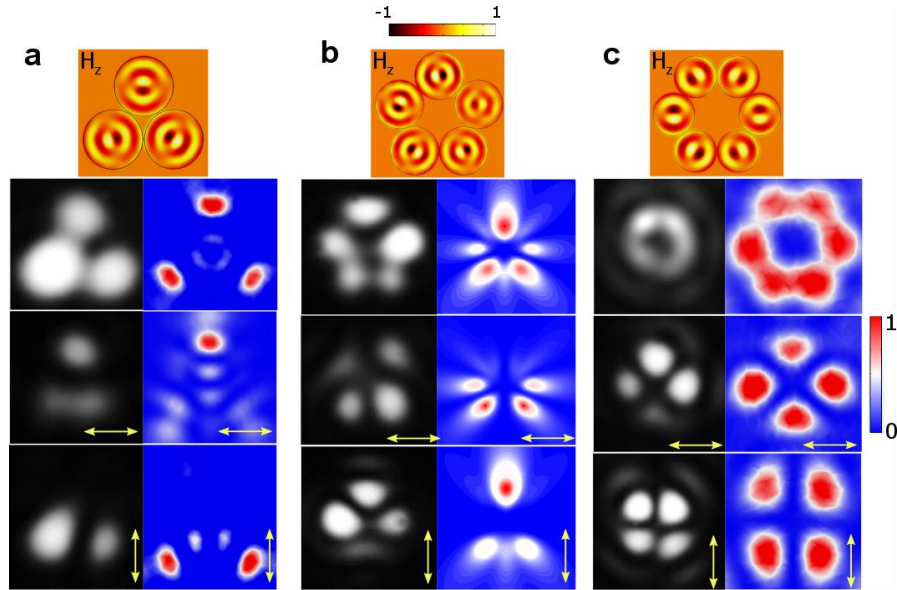


Figure 51 Polarization measurements for frustrated states. Theoretically predicted and experimentally measured polarization profiles for lasing supermodes in arrays of a, $N = 3$, b, $N = 5$, and c, $N = 6$ nanodisk laser arrays. The arrows indicate the direction of linear polarizations.

4.12. Summary

We have shown for the first time that the classical XY Hamiltonian can be realized by exploiting the dissipative cooperative interplay among vectorial electromagnetic modes. Using coupled metallic nanolaser lattices, both ferromagnetic and anti-ferromagnetic phases have been demonstrated experimentally, while in the AF regime, geometric frustration has been realized in full accord with theoretical predictions. In general, the proposed optical spin arrangement can be judiciously tailored so as to attain broader classes of XY Hamiltonians with arbitrary exchange couplings J_{ij} (section 4.10). Furthermore, in principle, it is possible to extend the use of this platform for implementing Ising Hamiltonian by modifying the mode in individual cavity elements. Finally, by providing a radically integrated solution for realizing photonic spin

machines, this platform could pave the way towards emulating more complex networks wherein a wide class of optimization algorithms and phase transition phenomena can be studied.

CHAPTER 5: CONCLUDING REMARKS

It is known that electrons interacting with a magnetic field can display an array of interesting and counterintuitive effects. These include for example topological insulators - a new phase of matter which have insulating properties in their bulk but are conductors in their edges. This peculiar behavior is a result of the particular band structure in these systems, where a nontrivial bandgap is a host of topologically protected “edge modes”. Moreover, this conduction in the edge is fundamentally different from a conventional conductor, in the sense that it is unidirectional and robust against local perturbations.

In recent years, the possibility of observing similar effects that arise from the interaction of magnetic fields with electrons, has been largely explored in photonic settings. However, the main challenge in such arrangements is the fact that photons, as neutral bosons, are in general not affected by magnetic fields. One possibility to circumvent such a limitation is to use magneto-optic materials, where applying a magnetic field would change optical properties of the medium. Even though such an idea might seem appealing in the first glance, the limitations in terms of weak magneto-optic coefficients for the existing materials and also the high costs imposed by the use of such materials make such propositions impractical. Therefore, clearly of interest would be to devise schemes based on standard optical material systems which exhibit some type of synthetic magnetic fields for photons. This can be achieved, in general, by exploiting the aforementioned connection between geometric phases in such photonic systems and the Aharonov-Bohm phase in electronic structures. In addition to fundamental science, such results are expected to provide new optical functionalities including unidirectional light propagation and novel sensors.

As detailed in Chapter 2, here we used the duality between the geometric phase arising in the tunneling of light in a twisted multicore fiber structure and the Aharonov-Bohm phase to experimentally observe an artificial magnetic field in such arrangements. To observe this coupling phase, we proposed an interferometric technique based on a four-core fiber system, and showed that the magnitude of the equivalent artificial magnetic field can be experimentally tuned by changing the rate of twist in the structure. Based on this, we demonstrated for the first time the Aharonov-Bohm suppression of tunneling in a photonic setting. In addition, I showed both theoretically and experimentally that this new type of geometric phase remains invariant in the presence of optical nonlinearity and multimode behavior.

In Chapter 3, we introduced the “topological insulator lasers” in both 1- and 2-dimensions. Laser cavities are in general prone to disorder, which is inevitable due to fabrication imperfections, operational degradation and failure. It is well-known that the presence of disorder in a laser results in spatial light localization in the cavity, giving rise to several performance issues including lower output coupling, multimode lasing and reduced slope efficiency. Therefore, it is natural to contemplate exploiting topological features to design laser systems that are immune to disorder. In 1D, we developed a successful theoretical model that captures the complex dynamics of photons in the system which involves a mixture of nonlinear effects including gain saturation, carrier dynamics associated with the gain material, as well as the linewidth enhancement effect. We designed an experimental realization for our theoretical model based on semiconductor multilayer quantum well structures (InGaAsP material), and used the operational parameters associated with the experimental setup in our simulation models to predict the behavior of the system under different pumping levels. We successfully demonstrated that the introduction of topology in 1D

lasers leads into robust lasing in the defect mode of the structure with ultra-stable emission frequency, in sharp contrast to conventional 1D lasers which are highly prone to disorder. We further generalized our ideas to higher dimensions and devised a 2D topological insulator laser. After fabrication, our measurements confirmed our theoretical predictions regarding desirable attributes of the 2D topological insulator laser in contrast to a conventional laser array. More specifically, we were able to observe scatter-free, single edge-mode lasing even in pump powers well above lasing threshold. This in turn led into a considerably higher slope-efficiency as compared to trivial systems. Also, our predictions in terms of spectral purity of the emission from the device was confirmed by detailed experimental measurements.

Finally, in Chapter 4 we showed for the first time that spin Hamiltonians can be realized by exploiting the dissipative cooperative interplay among vectorial electromagnetic modes. Using coupled metallic nanolaser lattices, both ferromagnetic and anti-ferromagnetic phases were demonstrated experimentally. In the AF regime, geometric frustration was realized in full accord with theoretical predictions. In general, the proposed optical spin arrangement can be judiciously tailored so as to attain broader classes of XY Hamiltonians with arbitrary exchange couplings J_{ij} . Furthermore, in principle, it is possible to extend the use of this platform for implementing Ising Hamiltonian by modifying the mode in individual cavity elements. Finally, by providing a radically integrated solution for realizing photonic spin machines, this platform could pave the way towards emulating more complex networks wherein a wide class of optimization algorithms and phase transition phenomena can be studied.

REFERENCES

1. L. D. Landau and E. M. Lifshitz, *Quantum Mechanics: Non-Relativistic Theory* (Elsevier, 2013).
2. K. v. Klitzing, G. Dorda, and M. Pepper, "New Method for High-Accuracy Determination of the Fine-Structure Constant Based on Quantized Hall Resistance," *Phys. Rev. Lett.* **45**, 494–497 (1980).
3. M. Z. Hasan and C. L. Kane, "Colloquium: Topological insulators," *Rev. Mod. Phys.* **82**, 3045–3067 (2010).
4. N. Byers and C. N. Yang, "Theoretical Considerations Concerning Quantized Magnetic Flux in Superconducting Cylinders," *Phys. Rev. Lett.* **7**, 46–49 (1961).
5. T. Weiss, G. K. L. Wong, F. Biancalana, S. M. Barnett, X. M. Xi, and P. S. J. Russell, "Topological Zeeman effect and circular birefringence in twisted photonic crystal fibers," *JOSA B* **30**, 2921–2927 (2013).
6. M. Ornigotti, G. D. Valle, D. Gatti, and S. Longhi, "Topological suppression of optical tunneling in a twisted annular fiber," *Phys. Rev. A* **76**, 023833 (2007).
7. S. Longhi, "Bound states in the continuum in PT-symmetric optical lattices," *Opt. Lett.* **39**, 1697–1700 (2014).
8. S. Longhi, "Light transfer control and diffraction management in circular fibre waveguide arrays," *J. Phys. B At. Mol. Opt. Phys.* **40**, 4477 (2007).
9. S. Longhi, "Effective magnetic fields for photons in waveguide and coupled resonator lattices," *Opt. Lett.* **38**, 3570–3573 (2013).

10. K. Fang, Z. Yu, and S. Fan, "Realizing effective magnetic field for photons by controlling the phase of dynamic modulation," *Nat. Photonics* **6**, 782–787 (2012).
11. S. Longhi, "Bloch dynamics of light waves in helical optical waveguide arrays," *Phys. Rev. B* **76**, 195119 (2007).
12. J. Dalibard, F. Gerbier, G. Juzeliūnas, and P. Öhberg, "Colloquium," *Rev. Mod. Phys.* **83**, 1523–1543 (2011).
13. M. Hafezi, E. A. Demler, M. D. Lukin, and J. M. Taylor, "Robust optical delay lines with topological protection," *Nat. Phys.* **7**, 907–912 (2011).
14. M. C. Rechtsman, J. M. Zeuner, Y. Plotnik, Y. Lumer, D. Podolsky, F. Dreisow, S. Nolte, M. Segev, and A. Szameit, "Photonic Floquet topological insulators," *Nature* **496**, 196–200 (2013).
15. A. B. Khanikaev, S. Hossein Mousavi, W.-K. Tse, M. Kargarian, A. H. MacDonald, and G. Shvets, "Photonic topological insulators," *Nat. Mater.* **12**, 233–239 (2013).
16. Z. Wang, Y. Chong, J. D. Joannopoulos, and M. Soljačić, "Observation of unidirectional backscattering-immune topological electromagnetic states," *Nature* **461**, 772–775 (2009).
17. M. V. Berry, "Quantal Phase Factors Accompanying Adiabatic Changes," *Proc. R. Soc. Lond. Math. Phys. Eng. Sci.* **392**, 45–57 (1984).
18. J. N. Ross, "The rotation of the polarization in low birefringence monomode optical fibres due to geometric effects," *Opt. Quantum Electron.* **16**, 455–461 (1984).
19. R. Y. Chiao and Y.-S. Wu, "Manifestations of Berry's Topological Phase for the Photon," *Phys. Rev. Lett.* **57**, 933–936 (1986).

20. A. Tomita and R. Y. Chiao, "Observation of Berry's Topological Phase by Use of an Optical Fiber," *Phys. Rev. Lett.* **57**, 937–940 (1986).
21. S. Weigert, "Topological quenching of the tunnel splitting for a particle in a double-well potential on a planar loop," *Phys. Rev. A* **50**, 4572–4581 (1994).
22. Y. Aharonov and D. Bohm, "Significance of Electromagnetic Potentials in the Quantum Theory," *Phys. Rev.* **115**, 485–491 (1959).
23. Y. Aharonov and D. Bohm, "Further Considerations on Electromagnetic Potentials in the Quantum Theory," *Phys. Rev.* **123**, 1511–1524 (1961).
24. D. J. Thouless, M. Kohmoto, M. P. Nightingale, and M. den Nijs, "Quantized Hall Conductance in a Two-Dimensional Periodic Potential," *Phys. Rev. Lett.* **49**, 405–408 (1982).
25. C. L. Kane and E. J. Mele, "Quantum Spin Hall Effect in Graphene," *Phys. Rev. Lett.* **95**, 226801 (2005).
26. X.-L. Qi and S.-C. Zhang, "Topological insulators and superconductors," *Rev. Mod. Phys.* **83**, 1057–1110 (2011).
27. C. L. Kane and T. C. Lubensky, "Topological boundary modes in isostatic lattices," *Nat. Phys.* **10**, 39–45 (2014).
28. Z. Yang, F. Gao, X. Shi, X. Lin, Z. Gao, Y. Chong, and B. Zhang, "Topological Acoustics," *Phys. Rev. Lett.* **114**, 114301 (2015).
29. L. Tarruell, D. Greif, T. Uehlinger, G. Jotzu, and T. Esslinger, "Creating, moving and merging Dirac points with a Fermi gas in a tunable honeycomb lattice," *Nature* **483**, 302–305 (2012).

30. L. Lu, J. D. Joannopoulos, and M. Soljačić, "Topological photonics," *Nat. Photonics* **8**, 821–829 (2014).
31. S. Malzard, C. Poli, and H. Schomerus, "Topologically Protected Defect States in Open Photonic Systems with Non-Hermitian Charge-Conjugation and Parity-Time Symmetry," *Phys. Rev. Lett.* **115**, 200402 (2015).
32. C.-E. Bardyn, M. A. Baranov, C. V. Kraus, E. Rico, A. İmamoğlu, P. Zoller, and S. Diehl, "Topology by dissipation," *New J. Phys.* **15**, 085001 (2013).
33. D. Leykam, K. Y. Bliokh, C. Huang, Y. D. Chong, and F. Nori, "Edge Modes, Degeneracies, and Topological Numbers in Non-Hermitian Systems," *Phys. Rev. Lett.* **118**, 040401 (2017).
34. C. E. Ruter, K. G. Makris, R. El-Ganainy, D. N. Christodoulides, M. Segev, and D. Kip, "Observation of parity-time symmetry in optics," *Nat. Phys.* **6**, 192–195 (2010).
35. H. Hodaei, M.-A. Miri, M. Heinrich, D. N. Christodoulides, and M. Khajavikhan, "Parity-time-symmetric microring lasers," *Science* **346**, 975–978 (2014).
36. F. D. M. Haldane and S. Raghu, "Possible Realization of Directional Optical Waveguides in Photonic Crystals with Broken Time-Reversal Symmetry," *Phys. Rev. Lett.* **100**, 013904 (2008).
37. W. P. Su, J. R. Schrieffer, and A. J. Heeger, "Solitons in Polyacetylene," *Phys. Rev. Lett.* **42**, 1698–1701 (1979).
38. S. Longhi, "PT phase control in circular multi-core fibers," *Opt. Lett.* **41**, 1897–1900 (2016).

39. C. Castro-Castro, Y. Shen, G. Srinivasan, A. B. Aceves, and P. G. Kevrekidis, "Light dynamics in nonlinear trimers and twisted multicore fibers," *J. Nonlinear Opt. Phys. Mater.* **25**, 1650042 (2016).
40. P. S. Westbrook, T. Kremp, K. S. Feder, W. Ko, E. M. Monberg, H. Wu, D. A. Simoff, T. F. Taunay, and R. M. Ortiz, "Continuous Multicore Optical Fiber Grating Arrays for Distributed Sensing Applications," *J. Light. Technol.* **35**, 1248–1252 (2017).
41. X. Ma, C.-H. Liu, G. Chang, and A. Galvanauskas, "Angular-momentum coupled optical waves in chirally-coupled-core fibers," *Opt. Express* **19**, 26515–26528 (2011).
42. G. K. L. Wong, M. S. Kang, H. W. Lee, F. Biancalana, C. Conti, T. Weiss, and P. S. J. Russell, "Excitation of Orbital Angular Momentum Resonances in Helically Twisted Photonic Crystal Fiber," *Science* **337**, 446–449 (2012).
43. M. Parto, H. Lopez-Aviles, M. Khajavikhan, R. Amezcua-Correa, and D. N. Christodoulides, "Topological Aharonov-Bohm suppression of optical tunneling in twisted nonlinear multicore fibers," *Phys. Rev. A* **96**, 043816 (2017).
44. M. Parto, H. Lopez-Aviles, J. E. Antonio-Lopez, M. Khajavikhan, R. Amezcua-Correa, and D. N. Christodoulides, "Observation of twist-induced geometric phases and inhibition of optical tunneling via Aharonov-Bohm effects," *Sci. Adv.* **5**, eaau8135 (2019).
45. K. G. Makris and D. N. Christodoulides, "Method of images in optical discrete systems," *Phys. Rev. E* **73**, 036616 (2006).
46. *Handbook of Elliptic Integrals for Engineers and Scientists* / Paul F. Byrd / Springer (n.d.).
47. S. Trillo and S. Wabnitz, "Nonlinear nonreciprocity in a coherent mismatched directional coupler," *Appl. Phys. Lett.* **49**, 752–754 (1986).

48. B. Daino, G. Gregori, and S. Wabnitz, "Stability analysis of nonlinear coherent coupling," *J. Appl. Phys.* **58**, 4512–4514 (1985).
49. C. Zener, "A theory of the electrical breakdown of solid dielectrics," *Proc R Soc Lond A* **145**, 523–529 (1934).
50. L. D. Landau, "A Theory of Energy Transfer II," *Phys. Z. Sowjetunion* **2**, 46 (1932).
51. C. Zener, "Non-adiabatic crossing of energy levels," *Proc R Soc Lond A* **137**, 696–702 (1932).
52. E. C. G. Stückelberg, "Theory of Inelastic Collisions Between Atoms," *Helv. Phys. Acta* **5**, 369 (1932).
53. E. Majorana, "Oriented atoms in a variable magnetic field," *Nuovo Cimento* **9**, 45 (1932).
54. F. Grossmann, T. Dittrich, P. Jung, and P. Hänggi, "Coherent destruction of tunneling," *Phys. Rev. Lett.* **67**, 516–519 (1991).
55. D. H. Dunlap and V. M. Kenkre, "Dynamic localization of a charged particle moving under the influence of an electric field," *Phys. Rev. B* **34**, 3625–3633 (1986).
56. A. Szameit, I. L. Garanovich, M. Heinrich, A. A. Sukhorukov, F. Dreisow, T. Pertsch, S. Nolte, A. Tünnermann, and Y. S. Kivshar, "Polychromatic dynamic localization in curved photonic lattices," *Nat. Phys.* **5**, 271–275 (2009).
57. J. Dalibard, F. Gerbier, G. Juzeliūnas, and P. Öhberg, "Colloquium: Artificial gauge potentials for neutral atoms," *Rev. Mod. Phys.* **83**, 1523–1543 (2011).
58. Y.-J. Lin, R. L. Compton, K. Jiménez-García, J. V. Porto, and I. B. Spielman, "Synthetic magnetic fields for ultracold neutral atoms," *Nature* **462**, 628–632 (2009).

59. R. O. Umucalılar and I. Carusotto, "Artificial gauge field for photons in coupled cavity arrays," *Phys. Rev. A* **84**, 043804 (2011).
60. A. L. Fetter, "Rotating trapped Bose-Einstein condensates," *Rev. Mod. Phys.* **81**, 647–691 (2009).
61. S.-M. Cui, "Nonadiabatic Berry phase in rotating systems," *Phys. Rev. A* **45**, 5255–5257 (1992).
62. M. Hafezi, S. Mittal, J. Fan, A. Migdall, and J. M. Taylor, "Imaging topological edge states in silicon photonics," *Nat. Photonics* **7**, 1001–1005 (2013).
63. M. A. Bandres, S. Wittek, G. Harari, M. Parto, J. Ren, M. Segev, D. N. Christodoulides, and M. Khajavikhan, "Topological insulator laser: Experiments," *Science* **359**, eaar4005 (2018).
64. M. Parto, S. Wittek, H. Hodaei, G. Harari, M. A. Bandres, J. Ren, M. C. Rechtsman, M. Segev, D. N. Christodoulides, and M. Khajavikhan, "Edge-Mode Lasing in 1D Topological Active Arrays," *Phys. Rev. Lett.* **120**, 113901 (2018).
65. M. C. Rechtsman, J. M. Zeuner, A. Tünnermann, S. Nolte, M. Segev, and A. Szameit, "Strain-induced pseudomagnetic field and photonic Landau levels in dielectric structures," *Nat. Photonics* **7**, 153–158 (2013).
66. N. Schine, A. Ryou, A. Gromov, A. Sommer, and J. Simon, "Synthetic Landau levels for photons," *Nature* **534**, 671 (2016).
67. I. Bloch, J. Dalibard, and W. Zwerger, "Many-body physics with ultracold gases," *Rev. Mod. Phys.* **80**, 885–964 (2008).

68. D. Jaksch and P. Zoller, "Creation of effective magnetic fields in optical lattices: the Hofstadter butterfly for cold neutral atoms," *New J. Phys.* **5**, 56 (2003).
69. S. Pancharatnam, "Generalized theory of interference, and its applications," *Proc. Indian Acad. Sci. - Sect. A* **44**, 247–262 (1956).
70. M. V. Berry, "The Adiabatic Phase and Pancharatnam's Phase for Polarized Light," *J Mod Opt* **34**, 1401–1407 (1987).
71. "JETP Letters: issues online," http://www.jetpletters.ac.ru/ps/1311/article_19812.shtml.
72. I. V. Kataevskaya and N. D. Kundikova, "Influence of the helical shape of a fibre waveguide on the propagation of light," *Quantum Electron.* **25**, 927 (1995).
73. R. Beravat, G. K. L. Wong, M. H. Frosz, X. M. Xi, and P. S. J. Russell, "Twist-induced guidance in coreless photonic crystal fiber: A helical channel for light," *Sci. Adv.* **2**, e1601421 (2016).
74. X. M. Xi, T. Weiss, G. K. L. Wong, F. Biancalana, S. M. Barnett, M. J. Padgett, and P. S. J. Russell, "Optical Activity in Twisted Solid-Core Photonic Crystal Fibers," *Phys. Rev. Lett.* **110**, 143903 (2013).
75. X. M. Xi, G. K. L. Wong, M. H. Frosz, F. Babic, G. Ahmed, X. Jiang, T. G. Euser, and P. S. J. Russell, "Orbital-angular-momentum-preserving helical Bloch modes in twisted photonic crystal fiber," *Optica* **1**, 165–169 (2014).
76. A. Noguchi, Y. Shikano, K. Toyoda, and S. Urabe, "Aharonov–Bohm effect in the tunnelling of a quantum rotor in a linear Paul trap," *Nat. Commun.* **5**, 3868 (2014).
77. C.-H. Tsai and D. Neilson, "New quantum interference effect in rotating systems," *Phys. Rev. A* **37**, 619–621 (1988).

78. R. Peierls, "Zur Theorie des Diamagnetismus von Leitungselektronen," *Z. Für Phys.* **80**, 763–791 (1933).
79. M. Parto, M. A. Eftekhar, M.-A. Miri, R. Amezcua-Correa, G. Li, and D. N. Christodoulides, "Systematic approach for designing zero-DGD coupled multi-core optical fibers," *Opt. Lett.* **41**, 1917–1920 (2016).
80. Y. Wu and K. S. Chiang, "Compact three-core fibers with ultra-low differential group delays for broadband mode-division multiplexing," *Opt. Express* **23**, 20867–20875 (2015).
81. T. Sakamoto, T. Mori, M. Wada, T. Yamamoto, and F. Yamamoto, "Coupled Multicore Fiber Design With Low Intercore Differential Mode Delay for High-Density Space Division Multiplexing," *J. Light. Technol.* **33**, 1175–1181 (2015).
82. A. W. Snyder and A. Ankiewicz, "Optical fiber couplers-optimum solution for unequal cores," *J. Light. Technol.* **6**, 463–474 (1988).
83. A. Tonomura, N. Osakabe, T. Matsuda, T. Kawasaki, J. Endo, S. Yano, and H. Yamada, "Evidence for Aharonov-Bohm effect with magnetic field completely shielded from electron wave," *Phys. Rev. Lett.* **56**, 792–795 (1986).
84. A. Bachtold, C. Strunk, J.-P. Salvetat, J.-M. Bonard, L. Forró, T. Nussbaumer, and C. Schönenberger, "Aharonov–Bohm oscillations in carbon nanotubes," *Nature* **397**, 673–675 (1999).
85. H. Peng, K. Lai, D. Kong, S. Meister, Y. Chen, X.-L. Qi, S.-C. Zhang, Z.-X. Shen, and Y. Cui, "Aharonov-Bohm interference in topological insulator nanoribbons," *Nat. Mater.* **9**, 225–229 (2010).

86. B. A. Bernevig, T. L. Hughes, and S.-C. Zhang, "Quantum Spin Hall Effect and Topological Phase Transition in HgTe Quantum Wells," *Science* **314**, 1757–1761 (2006).
87. M. König, S. Wiedmann, C. Brüne, A. Roth, H. Buhmann, L. W. Molenkamp, X.-L. Qi, and S.-C. Zhang, "Quantum Spin Hall Insulator State in HgTe Quantum Wells," *Science* **318**, 766–770 (2007).
88. M. Atala, M. Aidelsburger, J. T. Barreiro, D. Abanin, T. Kitagawa, E. Demler, and I. Bloch, "Direct Measurement of the Zak phase in Topological Bloch Bands," arXiv:1212.0572 (2012).
89. R. Fleury, A. B. Khanikaev, and A. Alù, "Floquet topological insulators for sound," *Nat. Commun.* **7**, 11744 (2016).
90. Z. Yu, G. Veronis, Z. Wang, and S. Fan, "One-Way Electromagnetic Waveguide Formed at the Interface between a Plasmonic Metal under a Static Magnetic Field and a Photonic Crystal," *Phys. Rev. Lett.* **100**, 023902 (2008).
91. X. Cheng, C. Jouvaud, X. Ni, S. H. Mousavi, A. Z. Genack, and A. B. Khanikaev, "Robust reconfigurable electromagnetic pathways within a photonic topological insulator," *Nat. Mater.* **15**, 542–548 (2016).
92. G. Jotzu, M. Messer, R. Desbuquois, M. Lebrat, T. Uehlinger, D. Greif, and T. Esslinger, "Experimental realization of the topological Haldane model with ultracold fermions," *Nature* **515**, 237–240 (2014).
93. M. Aidelsburger, M. Lohse, C. Schweizer, M. Atala, J. T. Barreiro, S. Nascimbène, N. R. Cooper, I. Bloch, and N. Goldman, "Measuring the Chern number of Hofstadter bands with ultracold bosonic atoms," *Nat. Phys.* **11**, 162–166 (2015).

94. A. P. Slobozhanyuk, A. B. Khanikaev, D. S. Filonov, D. A. Smirnova, A. E. Miroshnichenko, and Y. S. Kivshar, "Experimental demonstration of topological effects in bianisotropic metamaterials," *Sci. Rep.* **6**, 22270 (2016).
95. G. Harari, M. A. Bandres, Y. Lumer, M. C. Rechtsman, Y. D. Chong, M. Khajavikhan, D. N. Christodoulides, and M. Segev, "Topological insulator laser: Theory," *Science* eaar4003 (2018).
96. P. St-Jean, V. Goblot, E. Galopin, A. Lemaître, T. Ozawa, L. L. Gratiet, I. Sagnes, J. Bloch, and A. Amo, "Lasing in topological edge states of a one-dimensional lattice," *Nat. Photonics* **11**, 651 (2017).
97. H. Zhao, P. Miao, M. H. Teimourpour, S. Malzard, R. El-Ganainy, H. Schomerus, and L. Feng, "Topological hybrid silicon microlasers," *Nat. Commun.* **9**, 981 (2018).
98. S. Wittek, G. Harari, M. A. Bandres, H. Hodaei, M. Parto, P. Aleahmad, M. C. Rechtsman, Y. D. Chong, D. N. Christodoulides, M. Khajavikhan, and M. Segev, "Towards the Experimental Realization of the Topological Insulator Laser," in *Conference on Lasers and Electro-Optics (2017), Paper FTh1D.3* (Optical Society of America, 2017), p. FTh1D.3.
99. B. Bahari, A. Ndao, F. Vallini, A. E. Amili, Y. Fainman, and B. Kanté, "Nonreciprocal lasing in topological cavities of arbitrary geometries," *Science* eaao4551 (2017).
100. M. S. Rudner and L. S. Levitov, "Topological Transition in a Non-Hermitian Quantum Walk," *Phys. Rev. Lett.* **102**, 065703 (2009).
101. J. M. Zeuner, M. C. Rechtsman, Y. Plotnik, Y. Lumer, S. Nolte, M. S. Rudner, M. Segev, and A. Szameit, "Observation of a Topological Transition in the Bulk of a Non-Hermitian System," *Phys. Rev. Lett.* **115**, 040402 (2015).

102. S. Weimann, M. Kremer, Y. Plotnik, Y. Lumer, S. Nolte, K. G. Makris, M. Segev, M. C. Rechtsman, and A. Szameit, "Topologically protected bound states in photonic parity-time-symmetric crystals," *Nat. Mater.* **16**, 433–438 (2017).
103. *Semiconductor Lasers* / Govind P. Agrawal / Springer (n.d.).
104. J. C. Garrison and E. M. Wright, "Complex geometrical phases for dissipative systems," *Phys. Lett. A* **128**, 177–181 (1988).
105. S.-D. Liang and G.-Y. Huang, "Topological invariance and global Berry phase in non-Hermitian systems," *Phys. Rev. A* **87**, 012118 (2013).
106. J. Zak, "Berry's phase for energy bands in solids," *Phys. Rev. Lett.* **62**, 2747–2750 (1989).
107. J. P. Hohimer and G. A. Vawter, "Unidirectional semiconductor ring lasers with racetrack cavities," *Appl. Phys. Lett.* **63**, 2457–2459 (1993).
108. J.-F. Sadoc and R. Mosseri, "Geometrical Frustration by Jean-François Sadoc," [/core/books/geometrical-frustration/9CFBF6ECABC759B83B32B37289E0F53E](#).
109. L. Pauling, "The Structure and Entropy of Ice and of Other Crystals with Some Randomness of Atomic Arrangement," *J. Am. Chem. Soc.* **57**, 2680–2684 (1935).
110. A. P. Ramirez, A. Hayashi, R. J. Cava, R. Siddharthan, and B. S. Shastry, "Zero-point entropy in 'spin ice,'" *Nature* **399**, 333–335 (1999).
111. M. J. Harris, S. T. Bramwell, D. F. McMorrow, T. Zeiske, and K. W. Godfrey, "Geometrical Frustration in the Ferromagnetic Pyrochlore $\text{Ho}_2\text{Ti}_2\text{O}_7$," *Phys. Rev. Lett.* **79**, 2554–2557 (1997).
112. C. Wu, "Orbital Ordering and Frustration of p-Band Mott Insulators," *Phys. Rev. Lett.* **100**, 200406 (2008).

113. D. C. Wright and N. D. Mermin, "Crystalline liquids: the blue phases," *Rev. Mod. Phys.* **61**, 385–432 (1989).
114. L. Balents, "Spin liquids in frustrated magnets," *Nature* **464**, 199–208 (2010).
115. G. D. las Cuevas and T. S. Cubitt, "Simple universal models capture all classical spin physics," *Science* **351**, 1180–1183 (2016).
116. S. Kirkpatrick, C. D. Gelatt, and M. P. Vecchi, "Optimization by Simulated Annealing," *Science* **220**, 671–680 (1983).
117. I. Bloch, J. Dalibard, and S. Nascimbène, "Quantum simulations with ultracold quantum gases," *Nat. Phys.* **8**, 267–276 (2012).
118. J. Struck, C. Ölschläger, R. L. Targat, P. Soltan-Panahi, A. Eckardt, M. Lewenstein, P. Windpassinger, and K. Sengstock, "Quantum Simulation of Frustrated Classical Magnetism in Triangular Optical Lattices," *Science* **333**, 996–999 (2011).
119. S. Trotzky, P. Cheinet, S. Fölling, M. Feld, U. Schnorrberger, A. M. Rey, A. Polkovnikov, E. A. Demler, M. D. Lukin, and I. Bloch, "Time-Resolved Observation and Control of Superexchange Interactions with Ultracold Atoms in Optical Lattices," *Science* **319**, 295–299 (2008).
120. J. Struck, M. Weinberg, C. Ölschläger, P. Windpassinger, J. Simonet, K. Sengstock, R. Höppner, P. Hauke, A. Eckardt, M. Lewenstein, and L. Mathey, "Engineering Ising-XY spin-models in a triangular lattice using tunable artificial gauge fields," *Nat. Phys.* **9**, 738–743 (2013).

121. A. Marandi, Z. Wang, K. Takata, R. L. Byer, and Y. Yamamoto, "Network of time-multiplexed optical parametric oscillators as a coherent Ising machine," *Nat. Photonics* **8**, 937–942 (2014).
122. P. L. McMahon, A. Marandi, Y. Haribara, R. Hamerly, C. Langrock, S. Tamate, T. Inagaki, H. Takesue, S. Utsunomiya, K. Aihara, R. L. Byer, M. M. Fejer, H. Mabuchi, and Y. Yamamoto, "A fully-programmable 100-spin coherent Ising machine with all-to-all connections," *Science* aah5178 (2016).
123. Y. Takeda, S. Tamate, Y. Yamamoto, H. Takesue, T. Inagaki, and S. Utsunomiya, "Boltzmann sampling for an XY model using a non-degenerate optical parametric oscillator network," *Quantum Sci. Technol.* **3**, 014004 (2018).
124. N. G. Berloff, M. Silva, K. Kalinin, A. Askitopoulos, J. D. Töpfer, P. Cilibrizzi, W. Langbein, and P. G. Lagoudakis, "Realizing the classical XY Hamiltonian in polariton simulators," *Nat. Mater.* **16**, 1120–1126 (2017).
125. P. G. Lagoudakis and N. G. Berloff, "A polariton graph simulator," *New J. Phys.* **19**, 125008 (2017).
126. M. Nixon, E. Ronen, A. A. Friesem, and N. Davidson, "Observing Geometric Frustration with Thousands of Coupled Lasers," *Phys. Rev. Lett.* **110**, 184102 (2013).
127. V. Pal, C. Tradonsky, R. Chriki, A. A. Friesem, and N. Davidson, "Observing Dissipative Topological Defects with Coupled Lasers," *Phys. Rev. Lett.* **119**, 013902 (2017).
128. S. H. Strogatz, "Exploring complex networks," *Nature* **410**, 268–276 (2001).
129. J. T. Ariaratnam and S. H. Strogatz, "Phase Diagram for the Winfree Model of Coupled Nonlinear Oscillators," *Phys. Rev. Lett.* **86**, 4278–4281 (2001).

130. M. C. Soriano, J. García-Ojalvo, C. R. Mirasso, and I. Fischer, "Complex photonics: Dynamics and applications of delay-coupled semiconductor lasers," *Rev. Mod. Phys.* **85**, 421–470 (2013).
131. J. M. Hickmann, E. J. S. Fonseca, W. C. Soares, and S. Chávez-Cerda, "Unveiling a Truncated Optical Lattice Associated with a Triangular Aperture Using Light's Orbital Angular Momentum," *Phys. Rev. Lett.* **105**, 053904 (2010).
132. T. Inagaki, K. Inaba, R. Hamerly, K. Inoue, Y. Yamamoto, and H. Takesue, "Large-scale Ising spin network based on degenerate optical parametric oscillators," *Nat. Photonics* **10**, 415–419 (2016).